Adjoint Data Assimilation Methods for Cardiac Mechanics

Gabriel Balaban

5th January 2017

Thesis submitted for the degree of Philosophiæ Doctor

Acknowledgements

This thesis is the result of a little more than three years of work at Simula Research Laboratory. It could not have been done without the efforts of my main supervisor Dr. Marie E. Rognes, who was very supportive of me and my work, especially when things were tough. Dr. Rognes' questioning and attention to detail greatly increased the rigorousness of my work, for which I am most grateful.

Many thanks as well to my co-supervisor Dr. Joakim Sundnes who was always willing to share his knowledge of computational mechanics with me. On many occasions he pointed me towards previous studies which ended up saving weeks of work. I would also like to thank Dr. Samuel Wall, who guided much of my work and whose enthusiasm was a constant source of inspiration for me. Partway through the thesis I began a collaboration with my fellow PhD student Henrik Finsberg. I truly enjoyed working together with him, and learned a lot from our discussions. Many thanks Henrik for the good team work. I think we achieved a lot more together than we could have separately.

Computational cardiac modelling can be very theoretically demanding, with many hours devoted to mathematical formula and software implementations. Medical knowledge however, is what makes the models relevant to society. I am very grateful to have been able to spend part of my working week at Oslo University Hospital where I received a lot of advice from medical doctors. Many thanks especially to Stian Ross, Dr. Einar Hopp, Lars Dejgaard, Dr. Ida Leren, Dr. Espen Remme, and Dr. Eirik Nestaas for the enlightening discussions and Piritta Nyberg for keeping me well supplied with fruit. I am also very grateful to Professor Eigil Samset for his personal assistance with regards to speckle tracking echocardiography.

In addition to the stimulating setting at the hospital I have also enjoyed a very good working environment at Simula. Many thanks to my office mates Øyvind Evju, Dr. August Johansson, Benjamin Kehlet, and Aslak Bergersen. Research is a lot more enjoyable in good company. Special thanks to Simon Funke for sharing many tips and tricks regarding his software dolfin-adjoint, and for working through many technical issues with me. Thanks as well to Sareh Behdadfar for early discussions which developed into parts of the third article of this thesis. I am indebted as well to Eleonora Piersanti for proof-reading the thesis introduction.

In February 2016 I had the pleasure of visiting Dr. Steven Niederer at King's College London. I would like to thank him for hosting me and introducing me to electrophysiology modelling.

Last but not least, I would like to thank my family in Oslo, Lena Gross and Lyra Balaban, for their love, support and patience, without which this thesis would not have been possible.

Contents

1 Introduction **1**

1.1 Heart Pumping Mechanics 3

1.2 Computational Mechanics 6

1.3 Data Assimilation 13

1.4 Summary of Papers 16

1.5 Perspectives and Future Work 18

2 Paper I: Adjoint Multi-Start Based Estimation of Cardiac Hyperelastic Material Parameters using Shear Data **25**

2.1 Introduction 27

2.2 Mathematical models and methods 29

2.3 Numerical Results 39

2.4 Discussion 48

2.5 Conclusions 52

3 Paper II: High Resolution Data Assimilation of Cardiac Mechanics **57**

3.1 Introduction 59

3.2 Materials and Methods 61

3.3 Numerical Results 74

3.4 Discussion 82

3.5 Conclusion and Future Outlook 85

4 Paper III: Data Assimilation of Cardiac Elastic Heterogeneity in an Infarcted Human **93**
4.1 Introduction 95
4.2 Methods and Materials 96
4.3 Results 105
4.4 Discussion 115
4.5 Conclusion 119

List of Papers

Paper I
Adjoint multi-start-based estimation of cardiac hyperelastic material parameters using shear data
Gabriel Balaban, Martin S. Alnæs, Joakim Sundnes, and Marie E. Rognes
Biomechanics and Modelling in Mechanobiology; 2016: p 1-13.

Paper II
High resolution data assimilation of cardiac mechanics
Gabriel Balaban, Henrik Finsberg, Hans Henrik Odland, Marie E. Rognes, Stian Ross, Joakim Sundnes, Samuel Wall
In review for publication

Paper III
Data assimilation of cardiac elastic heterogeneity in an infarcted human
Gabriel Balaban, Henrik Finsberg, Einar Hopp, Joakim Sundnes, Samuel Wall, Marie E. Rognes
To be submitted

1 Introduction

The history of cardiac research dates back to ancient times and is at least as old as Emperor Huang Ti's 'Canon of Internal Medicine', said to have been written in 2600 BCE. In more recent times, the development of mathematical models in biology and electronic computers has led to the field of computational cardiac modelling. This field is an exciting mix of biology, computer science, engineering, mathematics and medicine, which aims to reproduce the complex processes of the heart inside a computer model. This approach is complementary to traditional experimentation on physical cardiac tissue and clinical trials, and allows for simulated experiments to be performed that would be unethical or prohibitively expensive in real life. Additionally, computer models allow for information from a variety of sources to be combined with basic physical principles. This leads to potentially new insights from existing data, which increases the efficiency of cardiac research, and allows for the possibility of in-silico diagnosis and therapy planning tools.

In recent years there has been great interest in the creation of personalised cardiac models, reflecting the state of a specific patient's heart. Such models have powerful prognostic potential, allowing for therapies to be tried out on the virtual heart non-invasively, at low cost, and with no risk to the patient. For such a powerful model to be realized, it is of paramount importance that the model captures the key features of the patient's condition. This is typically accomplished by adjusting the parameters of the model in order to match the model's outputs to clinical measurements of the patient, a process which is often referred to as data assimilation.

A simple approach to data assimilation is to define a functional which quantifies the mismatch between model outputs and clinical measurements. Minimization of this functional accomplishes the data assimilation and leads to a set of parameters that best matches the patient's condition. Information regarding the gradient of the mismatch functional with regards to model parameters can be potentially very useful. The negative gradient points in the direction of greatest decrease of the functional, and this can be used to guide an optimization and thereby greatly improve its efficiency.

In cardiac mechanics, model equations typically take the form of variational principles based on continuum approximations of matter. Such equations often cannot be solved by closed form mathematical expressions, and instead require

numerical methods and software implementation. Similarly to the model equations, evaluation of mismatch functional gradients also requires software. Recently a new software tool for the automatic derivation of adjoint equations has been developed [10]. Via the adjoint-gradient formula, this tool also automates calculation of functional gradients, which can be obtained efficiently with a cost nearly independent of the number of model parameters i.e. gradient size. This opens up new possibilities for creating personalized mechanics models with high spatial resolution of model parameters. The development of such personalized models has been a major driver for this thesis, which has the following goals:

- Create adjoint-gradient based methods for the personalization of passive tissue properties and muscle contraction in a computational model of ventricular mechanics.
- Develop an algorithm that compute a personalized load-free reference geometry of a patient's ventricles and simultaneously estimates passive tissue properties.
- Exploit the computational efficiency of the adjoint-gradient formula in order to incorporate mechanical heterogeneities into personalized models of ventricular mechanics under pathological circumstances.

The rest of this thesis introduction is organized as follows. We explain basic cardiac anatomy and pumping function in Section 1.1, and then move on to mathematical modeling in Section 1.2 where we introduce the important concepts of strain, stress and hyperelasticity. The section ends with a brief overview of the Holzapfel-Ogden mechanics model, which is used extensively in this thesis. In Section 1.3 we present the basic concepts behind variational data assimilation, and give a brief overview of the literature on data assimilation in cardiac mechanics. We summarize the three articles of this thesis in Section 1.4 and provide conclusions and an outlook for the future in Section 1.5.

1.1 Heart Pumping Mechanics

The heart is a muscular pump that is responsible for the flow of blood throughout the body, and is essential to keeping the body alive. During a day of an average

person's life, it beats around 100,000 times and pumps about 7,200 liters of blood [13]. The structure of this remarkable organ is presented in Figure 1.1. Oxygen-poor blood from the body flows into the right side of the heart, and is pumped through the pulmonary artery to the lungs, where it picks up oxygen. It then enters the left side of the heart and is pumped through the aorta back into the rest of the body. The outer surface of the heart, which is in contact with the body, is called the epicardium. The inner surface, which is in contact with blood, is called the endocardium.

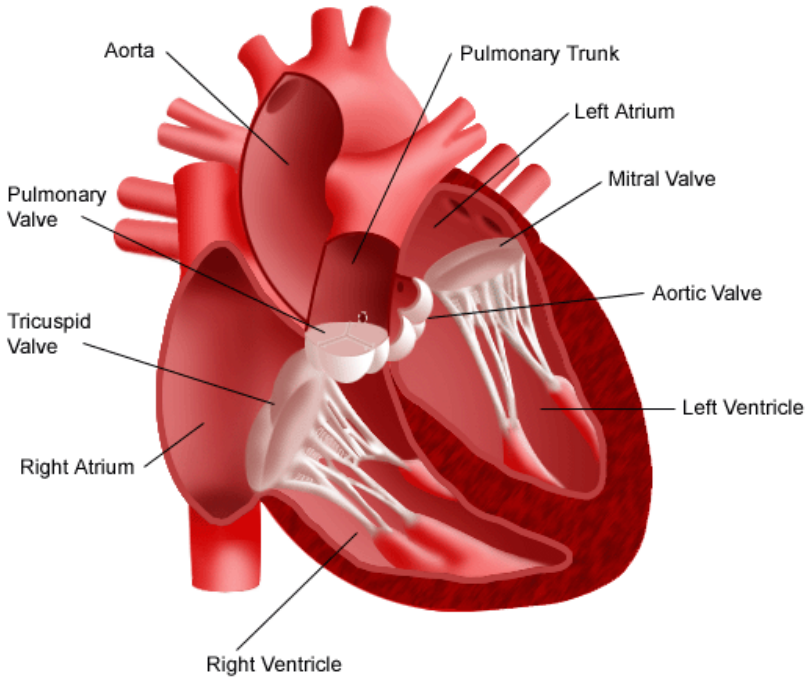

Figure 1.1: Anatomical view of the human heart showing the principle chambers and valves. Source: *http://www.hopkinsmedicine.org*.

Four chambers of the heart are used to pump blood. The bottom chambers are the ventricles. Each ventricle has two sets of valves, one for blood flowing in and one for blood flowing out. By restricting the direction of flow, the valves are essential to maintaining the correct pressure in the ventricles. Pressure must be high when pumping out and low when filling. The left ventricle is the largest

of the two ventricles, and has thicker walls required for the heavy job of pushing blood through the systemic circulation system. Being easier to image and of vital importance, the left ventricle is the focus of many computational modelling studies.

The top two chambers of the heart are the atria, which function as primer pumps. They inject extra blood into the ventricles and thereby increase ventricular function. Under normal circumstances, when the atria squeeze they fill the ventricles in two ways. Firstly atrial squeezing causes a pressure gradient across the mitral and tricuspid values, thereby causing flow of blood. Secondly the walls of the atria shorten and pull up on the valves mentioned above. This elongates the ventricles and increases their volume.

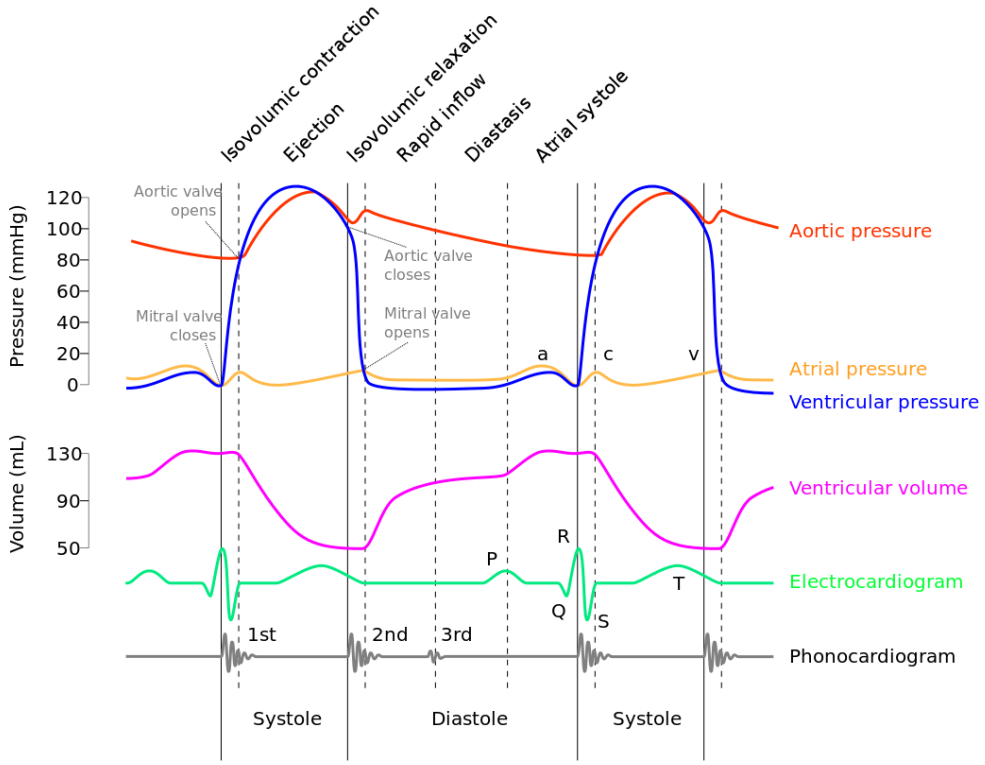

Figure 1.2: Classical Wiggers diagram showing mechanical and electrical events that occur in a typical heartbeat in the left side of a healthy human heart. Source: *Wikimedia Commons: Wiggers Diagram.svg*

The classical Wiggers diagram, Figure 1.2, shows the sequence of phases and corresponding pressure-volume relations of a single beat in the left side of the heart. All of the phases can be roughly divided into two events, systole and diastole. In systole the ventricle contracts, and in diastole it expands.

In the first phase, isovolumic contraction, the muscles of the left ventricle begin to contract with both valves closed. This causes the ventricular pressure to rapidly increase until it exceeds the aortic pressure. The reversal of the pressure gradient opens the aortic valve and the ejection phase begins. In this phase the ventricular volume decreases as blood is forced into the aorta. Consequently the pressure in the ventricle drops until it is lower than that of the aorta. The inertia of flowing blood briefly holds the aortic valve open and then the valve closes, beginning the isovolumic relaxation phase. In this phase the muscles in the ventricle release their tension, causing the blood pressure to drop further. Once the ventricular pressure drops below that of the atrium the mitral valve opens and the ventricle rapidly beings to fill with blood. This increases the ventricular volume during the rapid inflow phase. During the next phase, diastasis, the heart is at rest. Depending upon the heart-rate, this phase can be long or short, with faster heart-rates leading to a shorter diastasis phase. Finally, in the atrial systole phase, the ventricles are further filled by the contracting atria. This causes a rise in both ventricular pressure and volume.

The mechanics of the heart are coordinated by the heart's electrical activity. This activity is classically measured by the electrocardiogram, shown in green in the Wiggers diagram. The bottom curve, the phonocardiogram, shows the timing of sounds related to the opening and closing of valves.

1.2 Computational Mechanics

Mathematical models of the mechanics of cardiac tissue are often formulated within the general framework of continuum mechanics. In this framework the effects of detailed physical structures such as atoms, molecules and biological cells, are considered in an average sense. Matter is represented as existing in a homogenized continuum. This simplification allows for the computer simulation of tissues and organs, without having to deal with the details of smaller scale structures.

Fundamental to continuum mechanics is the Lagrangian description of motion. In this description we consider a body Ω which deforms over time to take the time-dependent shape $\omega(t)$. Each material point is tracked in the Lagrangian description, so that for every $\mathbf{X} \in \Omega$ we can find a corresponding $\mathbf{x}(t) \in \omega(t)$ which tracks the movement of $\mathbf{X}$ throughout the deformation. Out of computational convenience, we most often consider the displacement map

$$\mathbf{u}(t) = \mathbf{x}(t) - \mathbf{X}. \tag{1.1}$$

1.2.1 Strain

Differences in the motion of matter lead to strain. Intuitively, strains are changes in the relative motion of particles throughout a deformation. Just like displacements, strains need to be measured with respect to a reference. Many measurements for strain exist. A simple one dimensional measure is the engineering strain

$$\epsilon = \frac{l - L}{L}, \tag{1.2}$$

which is simply defined as the difference between deformed length l and reference length L divided by reference length. This measure of strain is popular in the field of speckle-tracking echocardiography, and provides a simple and effective way of describing length changes in the tissue of the heart.

For the purposes of mathematical modelling, more complicated measures of strain are used. The basis for all such measures is the displacement gradient, which is a rank 2 tensor whose components are defined as

$$\mathrm{Grad}\mathbf{u}_{ij} = \frac{\partial \mathbf{u}_i}{\partial \mathbf{X}_j}. \tag{1.3}$$

Diagonal components of this tensor measure changes in length and are called normal strains. Off diagonal components measure changes in angle, and are referred to as shear strains.

The engineering strain linearly approximates a normal component of the displacement gradient. To see this consider a 1-D line of length L deformed by the linear map $\mathbf{u}(\mathbf{X}) = \frac{l-L}{L}\mathbf{X}$. The length of such a line after deformation will be

$\mathbf{u}(\mathbf{X}_L) + L = l$, where $\mathbf{X}_L$ is the end-point of the line. By Equation 1.2 the engineering strain for this deformation will be $\frac{l-L}{L}$, which is exactly the derivative of $\mathbf{u}$. Using this approximation property it is possible to relate engineering strains from speckle tracking echocardiography to strains from continuum mechanics models given by the displacement gradient.

In addition to the strain measures mentioned above, relative deformation can also be measured by the so called deformation gradient

$$\mathbf{F} = \mathbf{u} + \mathbf{I}. \tag{1.4}$$

This measure has a multiplicative decomposition property for deformations through an intermediate configuration. Assume there is a point in the reference configuration $\mathbf{X}$, with corresponding point in the intermediate configuration $\mathbf{x}_1$ and corresponding point in the final configuration $\mathbf{x}_2$. Furthermore define the total displacement $\mathbf{u}(\mathbf{X}) = \mathbf{u}_2 \circ \mathbf{u}_1$, where $\mathbf{u}_2(\mathbf{x}_1) = \mathbf{x}_2 - \mathbf{x}_1$ and $\mathbf{u}_1(\mathbf{X}) = \mathbf{x}_1 - \mathbf{X}$. By definition

$$\mathbf{u}(\mathbf{X}) = \mathbf{u}_2(\mathbf{u}_1(\mathbf{X}) + \mathbf{X}) + \mathbf{u}_1(\mathbf{X}) + \mathbf{X}, \tag{1.5}$$

and by taking derivatives with respect to $\mathbf{X}$ and applying the chain rule one arrives at

$$\mathbf{F} = \mathbf{F}_2\mathbf{F}_1, \tag{1.6}$$

where $\mathbf{F}_2 = \mathrm{Grad}\mathbf{u}_2 + \mathbf{I}$, $\mathbf{F}_1 = \mathrm{Grad}\mathbf{u}_1 + \mathbf{I}$, and $\mathbf{F} = \mathrm{Grad}\mathbf{u} + \mathbf{I}$.

The multiplicative decomposition property of $\mathbf{F}$ is useful for comparing strains measured in-vivo to those of a continuum mechanics model. The reference configuration required for the Lagrangian description of motion is assumed to be load-free in hyperelastic theory. This is an assumption which cannot be made for an image based cardiac geometry, as there is always some blood pressure inside the heart. By considering the image based geometry to be an intermediate configuration, deformations measured in-vivo can be related to those given by Lagrangian mechanics. Furthermore, the multiplicative decomposition property is also used in the so-called active strain framework. This framework combines active muscle shortening with elastic deformation, and can account for whole-cycle motion of the heart. In active strain, shortening of muscles results in an intermediate configuration with deformation gradient $\mathbf{F}_a$ from which elastic forces are calculated. This results in an elastic deformation with deformation gradient $\mathbf{F}_e$. The total

deformation is then simply

$$\mathbf{F} = \mathbf{F}_e \mathbf{F}_a. \tag{1.7}$$

1.2.2 Stress

Strains in materials typically lead to states of stress. Stresses are defined as internal forces which act to maintain a material's deformed shape, and are defined as force per unit area. More specifically, if we consider a plane inside a deformed body, than the force exerted by the material on the plane can be represented by a vector quantity $\mathbf{t}$ in the deformed configuration and $\mathbf{T}$ in the reference configuration. By Cauchy's stress theorem [page 111 of [15]] there exist unique tensor fields $\boldsymbol{\sigma}$ and $\mathbf{P}$ such that

$$\begin{aligned} \mathbf{t}(\mathbf{x}, t, \mathbf{n}) &= \boldsymbol{\sigma}(\mathbf{x}, t)\mathbf{n} \\ \mathbf{T}(\mathbf{X}, t, \mathbf{N}) &= \mathbf{P}(\mathbf{X}, t)\mathbf{N}, \end{aligned} \tag{1.8}$$

where $\mathbf{n}$ and $\mathbf{N}$ are outward normals of the plane in deformed and reference configuration respectively. The tensors $\boldsymbol{\sigma}$ and $\mathbf{P}$ are the Cauchy and 1st Piola Kirchhoff stress tensors. By employing Nanson's formula it is possible to relate $\boldsymbol{\sigma}$ and $\mathbf{P}$, and thereby stresses in the deformed and reference configurations

$$\mathbf{P} = J\boldsymbol{\sigma}\mathbf{F}^{-T}, \tag{1.9}$$

where we have introduced the volume ratio $J = \det\mathbf{F}$. The mapping of stresses allows us the convenience of performing computer simulations in a reference configuration, which can be represented by an unchanging geometry throughout the entire simulation.

1.2.3 Hyperelasticity

Mathematical models of elasticity represents idealized materials which always return to their original shape when all external loads are removed. For situations in which deformations are large, such as in the heart, finite elasticity theory and hyperelastic models are required. Energy which is used to deform a hyperelastic model is stored in the material. This stored energy is typically given by a strain energy density function ψ, whose derivative with respect to the deformation gradient

gives the first Piola-Kirchhoff stress $\mathbf{P}$

$$\mathbf{P} = \frac{\partial \psi}{\partial \mathbf{F}}. \tag{1.10}$$

As cardiac tissue contains a large amount of water, incompressible variational principles are often employed for the calculation of model deformations. One such variational principle is the principle of stationary potential energy [Chapter 8.3 of [15]] which states that the total potential energy of a mechanical system is stationary when the system is at an equilibrium. Mathematically, internal and external energies, Π_{int} and Π_{ext}, are combined into a total energy functional Π, depending upon the deformation $\mathbf{u}$, and in the fully incompressible case an additional hydrostatic pressure field p

$$\Pi(\mathbf{u}, p) = \Pi_{\text{int}}(\mathbf{u}, p) + \Pi_{\text{ext}}(\mathbf{u}). \tag{1.11}$$

For an incompressible hyperelastic material the internal energy can be written as

$$\Pi_{\text{int}}(\mathbf{u}, p) = \int_{\Omega} p\,(J-1) + \psi(\mathbf{u})\; dV. \tag{1.12}$$

In this functional p acts as a Lagrange multiplier enforcing the incompressibility constraint $J - 1 = 0$. If the potential energy is differentiable, stationarity is equivalent to the first variation of the functional being equal to 0. We now define the Gateaux differential

$$D_{\mathbf{x}} f(\mathbf{x})[\delta \mathbf{x}] \equiv \frac{\partial}{\partial \epsilon} f(\mathbf{x} + \epsilon\, \delta \mathbf{x})\Big|_{\epsilon=0}, \tag{1.13}$$

which is presented for an abstract functional f in the direction $\mathbf{x}$. The energy (1.11) is then stationary if

$$0 = D_{\delta \mathbf{u}, \delta p} \Pi_{\text{int}}[\delta \mathbf{u}, \delta p] + D_{\delta \mathbf{u}, \delta p} \Pi_{\text{ext}}[\delta \mathbf{u}, \delta p], \tag{1.14}$$

where we have slightly expanded the notation (1.13) to indicate simultaneous variation of two variables. The equation (1.14) is also known as the principle of virtual

work, for which the internal work, δW_{int}, can be written as

$$\begin{aligned}\delta W_{\text{int}}(\mathbf{u}, p, \delta\mathbf{u}, \delta p) &= D_{\delta\mathbf{u},\delta p}\Pi_{\text{int}}[\delta\mathbf{u}, \delta p] \\ &= \int_\Omega \left(\mathbf{P} + pJ\mathbf{F}^{-T}\right) : \text{Grad}\delta\mathbf{u} + (J-1)\delta p \; dV.\end{aligned} \tag{1.15}$$

We have so far not specified any external energies or work terms. These terms depend upon the specific mechanical situation being modelled. For the case of left ventricular mechanics pressure loading of blood on the endocardium often plays an important role. If we denote the blood pressure by p_{blood}, the deformed endocardial surface by $\partial\omega_{\text{endo}}$, and the reference endocardial surface by $\partial\Omega_{\text{endo}}$, then the virtual work of the pressure load, δW_{press}, can be written as

$$\delta W_{\text{press}} = -p_{\text{blood}} \int_{\partial\omega_{\text{endo}}} \mathbf{n}\cdot\, \delta\mathbf{u} \; ds = -p_{\text{blood}} \int_{\partial\Omega_{\text{endo}}} J\mathbf{F}^{-T}\mathbf{N}\cdot\, \delta\mathbf{u} \; dS, \tag{1.16}$$

where the second equality follows from Nanson's formula.

1.2.4 The Holzapfel-Ogden Model

In the previous section a general framework for modelling incompressible hyperelastic materials was presented. In order to specify the framework to a specific material, such as cardiac tissue, a constitutive equation must be employed. In the case of hyperelasticity, such equations take the form of strain energy density functions. Furthermore, hyperelastic theory requires that such functions be invariant under rotation of the object that is being modelled. This motivates the formulation of the Right Cauchy-Green tensor

$$\mathbf{C} = \mathbf{F}^T\mathbf{F}. \tag{1.17}$$

By the polar decomposition theorem $\mathbf{F}$ can be decomposed into a rotation $\mathbf{R}$ and stretch $\mathbf{U}$ so that

$$\mathbf{C} = \mathbf{F}^T\mathbf{F} = \mathbf{U}^T\mathbf{R}^T\mathbf{R}\mathbf{U} = \mathbf{U}^T\mathbf{R}^{-1}\mathbf{R}\mathbf{U} = \mathbf{U}^T\mathbf{U}, \tag{1.18}$$

and we can see that $\mathbf{C}$ measures only the stretching component of $\mathbf{F}$. Rotation invariance of a strain energy function can be achieved by limiting the function arguments to a scalar set of invariants [page 215 of [15]].

In 2009 a model for the mechanical properties of cardiac tissue was proposed [14], which was based upon invariants. This model, often referred to as the Holzapfel-Ogden law, is orthotropic, with the myocardial micro-structure of fibers and sheets providing local axes of anisotropy. The two anisotropic axes are often referred to as the fiber, $\mathbf{e}_f$, and sheet, $\mathbf{e}_s$ axes. The invariants upon which the Holzapfel-Ogden law is based upon are

$$\begin{aligned} I_1 &= \text{tr}\,(\mathbf{C}), \\ I_{4f} &= \mathbf{e}_f \cdot \mathbf{C}\mathbf{e}_f, \\ I_{4s} &= \mathbf{e}_s \cdot \mathbf{C}\mathbf{e}_s, \\ I_{8fs} &= \mathbf{e}_f \cdot \mathbf{C}\mathbf{e}_s, \end{aligned} \tag{1.19}$$

with the first invariant capturing the isotropic response of the material and the last three the anisotropic response of the material. The Holzapfel-Ogden law depends upon a set of 8 material parameters, of which 4 are linear and 4 are exponential. The strain energy of this model is

$$\begin{aligned} \psi(\mathbf{C}, a, b, a_f, b_f, a_s, b_s, a_{fs}, b_{fs}) = \frac{a}{2b}\left(e^{b(I_1(\mathbf{C})-3)} - 1\right) + \sum_{i=f,s} \frac{a_i}{2b_i}\left(e^{b_i(I_{4i}(\mathbf{C})-1)_+^2} - 1\right) \\ + \frac{a_{fs}}{2b_{fs}}\left(e^{b_{fs}I_{8fs}^2(\mathbf{C})} - 1\right). \end{aligned} \tag{1.20}$$

Here the symbol $_+$ is the positive restriction $(\cdot)_+ = \max(\cdot, 0)$, which models the heart muscle fibers as resisting extension but not compression. For studies involving clinical data, a reduced transversely isotropic form of (1.20) is often employed

$$\psi(\mathbf{C}, a, b, a_f, b_f) = \frac{a}{2b}\left(e^{b(I_1(\mathbf{C})-3)} - 1\right) + \frac{a_f}{2b_f}\left(e^{b_f(I_{4f}(\mathbf{C})-1)_+^2} - 1\right). \tag{1.21}$$

This model has 4 fewer parameters than the orthotropic Holzapfel-Ogden law, making it easier to identify the parameters from potentially sparse and or noisy clinical data.

1.3 Data Assimilation

In this section we discuss data assimilation, that is the process of adjusting a computational model's parameters in order to match the model output to physical measurements. Applied to cardiac mechanics, a successful data assimilation results in a personalized model which reflects the state of a patient's heart.

1.3.1 The Least Squares Variational Approach

The least squares variational approach is a simple way to formulate a data assimilation problem. In this approach we have a set of observations of a system i.e. data points $\mathbf{o}_{\text{data}}$. We also have a mathematical model from which we can derive model based observations $\mathbf{o}_{\text{mod}}$. These model based observations can be tuned by a set of parameters $\mathbf{m}$ so that $\mathbf{o}_{\text{mod}}$ depends upon $\mathbf{m}$. In order to quantify the quality of a fit of model and data we introduce the classical least squares functional

$$I(\mathbf{m}) = \left|\mathbf{o}_{mod}(\mathbf{m}) - \mathbf{o}_{data}\right|^2. \tag{1.22}$$

The data assimilation problem consists of finding the set of optimal parameters $\mathbf{m}^*$ which minimize $I(\mathbf{m})$.

In the case of cardiac mechanics, our mathematical models consist of variational equations implemented as finite element software, which can take anywhere from minutes to days in order to run. For models with longer run-times, it is advantageous to use gradient-based optimization methods in order to minimize (1.22), as such algorithms tend to use fewer evaluations of the model than gradient-free methods. However, if the number of components of $\mathbf{m}$ is large, than calculating the gradient of (1.22) can be challenging. A classical finite difference approach involves evaluating the model with as many perturbations as there are parameters in order to approximate the gradient. This can greatly increase the number of model evaluations needed for an optimization. The adjoint gradient formula on the other hand can calculate the gradient of (1.22) with a computational cost nearly independent of the size of $\mathbf{m}$. For an introduction to the adjoint gradient formula we refer the reader to Section 2.4 of the first article in this thesis, and also to [10], which describes the principles behind the automatic adjoint derivation software dolfin-adjoint.

1.3.2 Review of data assimilation in cardiac mechanics

The design and use of mathematical models of cardiac mechanics has been an ongoing process over the last 4 decades. In the 1980's biaxial loading tests were performed on samples of ex-vivo canine myocardial tissue [7, 28]. The results of these experiments were used to fit coefficients of exponential stress-strain relations. Further tissue testing was performed in 2002, this time with porcine myocardium and simple shear deformations [8]. These experiments showed that the mechanical response of myocardium can be orthotropic, with the local myocardial fiber and sheet orientations providing orthogonal axes of anisotropy. Based on this data the Holzapfel-Ogden strain energy law was developed [14]. More recently, the porcine shear experiments [8] have been repeated with 24 specimens of human ventricular myocardium obtained very shortly after death [23]. An orthotropic response similar to the porcine experiments [8] was obtained.

A comparison of passive myocardial mechanics models was performed by assuming homogeneous shear angles [20, 22] and also with finite element methods which allowed for more flexible deformations [19, 21]. In these comparisons models were fitted to porcine shear data [8], and showed that the Costa Law [5] was best suited to forward simulation and inverse parameter estimation.

For clinical use determining material properties by tissue testing is unfeasible due to the destructive nature of the tests. Therefore there has been a lot of interest in using observations of whole organ behaviour for inverse material parameter determination. In 2005 such an organ scale parameter estimation was performed on ex-vivo dog hearts which were passively inflated [2]. The method proposed in this paper was based on tagged MRI images, and was validated with a gel phantom. Following this study the determination of material properties from in-vivo data was only a step away. In 2009 Wang et al. [25] used in-vivo MRI data of a dog heart, together with pressure data from a catheter, to identify parameters of the transversely isotropic Guccione Law [11].

More recently, analysis of MRI images has enabled the study of material properties of infarcted tissue in sheep hearts [16, 18]. These studies introduced the genetic algorithm optimization technique to cardiac mechanics. This technique is a global optimization method that uses successive generations of material parameters in order to search the parameter space and find the best minimum. For low-dimensional parameter sets it is a computationally expensive but effective

method that avoids getting trapped in suboptimal minima.

Over the past couple of years there has been a push to translate computational modelling techniques of cardiac mechanics to everyday clinical practice. Such translational research has given rise to several studies in which data assimilation is carried out for clinical data from human patients. In 2015 contractility parameters were estimated for 17 AHA zones using a derivative free subplex algorithm for 3 patients and 3 healthy volunteers [26]. A synthetic data test confirmed the accuracy of the technique. Such global optimizations with high dimensional parameter spaces are computationally very expensive, and for clinical applications computational times need to be kept at a minimum. Two recent studies [1, 12] have attempted to address this need by considering simplified models with few parameters which are personalized by a parameter sweep technique. Furthermore it was shown in [12] that the a-type linear parameters of the Holzapfel-Ogden law are structurally identifiable. This means that it is possible to uniquely determine the parameters, given sufficient information about deformation states of the heart which can be reproduced by the mathematical model. This result is an important first step towards a mathematical understanding of the conditions necessary for a unique parameter estimate obtainable from clinical data. Another simplified model, whose properties were personalized to echocardiography data, was proposed in [9]. A single parameter of this model was adjusted to fit measured LV volumes and the adjusted parameter was shown to be significantly different for healthy and infarcted hearts.

A popular approach to parameter estimation that has arisen in recent years is reduced order Unscented Kalman Filtering (rUKF). This approach estimates parameters sequentially, that is by considering one state of deformation at a time, and updates the parameters after each deformation state is assimilated. This is in contrast to variational approaches, such as the one described in Section 1.3.1, which assimilate all the data at once. For lower dimensional parameter sets the Kalman Filtering approach is computationally efficient and generates an estimate of the covariance matrix of the parameters that were estimated. This matrix provides useful information about the uncertainty of the parameter estimates, and also about possible linear coupling amongst parameters. The rUKF technique was introduced in the seminal paper [17], and tested on an example of data assimilation in cardiac biomechanics. Follow up studies showed its efficiency in a synthetic

data test with regional AHA stiffness parameters [27], and in the estimation of regional contractility in a model of a pig heart with a myocardial infarction [3].

Variational approaches to data assimilation using adjoint-gradients are an attractive way to handle models with high dimensional parameters, as the evaluation of the adjoint-gradient only requires a single forward and a single backward solve of the model, regardless of the number of parameters that need to be optimized. Pioneering work on applying this approach to cardiac mechanics was carried out in 2009 with a simple linear viscoelastic model used to reconstruct motion from cine-MRI images [24]. Further work was carried out in 2011 on the estimation of contractility in scarred and healthy regions using electrophysiology and cine-MRI data of three patients [6]. The models used in the two studies above were linear. This linearity greatly simplifies the implementation of an adjoint solver, which can be obtained by matrix-transposition of the original forward system. For more realistic nonlinear models of cardiac mechanics the implementation of an adjoint solver is more complex, requiring the solution of a separate linearized adjoint system. The derivation and software implementation of this adjoint system has been automated in the software dolfin-adjoint [10], which facilitates the use of adjoint models of nonlinear mechanics in this thesis.

In this review only a small part of the field of data assimilation in cardiac mechanics is covered. For a more comprehensive review the reader is referred to the excellent summary provided in [4].

1.4 Summary of Papers

The work of this thesis is divided into three papers, each of which is described in this section. In the first paper an adjoint-gradient technique is developed for the estimation of model parameters in cardiac mechanics. In the next two papers the adjoint-gradient methods are applied to the problems of estimating heterogeneities in passive and active properties of in-vivo myocardial tissue.

1.4.1 Paper I: Adjoint Multi-Start Based Estimation of Cardiacy Hyperelastic Material Parameters using Shear Data

A method for estimating material parameters of cardiac hyperelastic models is proposed. The method combines efficient adjoint gradient calculations as part of a local search using a sequential quadratic programming algorithm. This local search is embedded in a multi-start procedure; that is local optimizations are started from many initial points in the parameter space in order to explore a variety of minima. The new method is tested by estimating the parameters of the Holzapfel-Ogden law [14] by fitting a finite element model to shear data collected from porcine tissue samples [8]. This extends the previous work of Schmidt et al. [19, 21] to the Holzapfel-Ogden law. The results of the study show good model-data fits using our method, and that our adjoint-gradient implementation reaches theoretically optimal efficiency for larger system sizes. Finally, we demonstrate that the multi-start procedure is able to generate globally optimal minima in the absence of a good initial guess for the local search.

1.4.2 Paper II: High Resolution Data Assimilation of Cardiac Mechanics

In this work the adjoint-gradient methods developed in the previous paper are used to capture spatial variations in contraction in a patient-specific model of a dyssynchronous left ventricle. Regional strain measurements from 3-D echocardiography as well as pressure data from a catheter make up the clinical data of the study. These data show great regional variation in the timing and magnitude of wall motion, as can be expected in a dyssynchronous heart.

Adjoint-gradient based data assimilation is employed to estimate a piecewise linear contraction field whose spatial resolution is the same as the computational mesh representing the patient's ventricular geometry. In total 2661 control variables are optimized. This provides the highest level of detail to date in a personalized model of ventricular contraction. The simulated strains from the personalized model match very closely to the measured strains observed in-vivo. The accuracy and efficiency of our method opens up new possibilities for extending the capabilities of medical imaging, for example by providing a simulated patient-specific

stress field, and or a local contractility estimate.

1.4.3 Paper III: Data Assimilation of Cardiac Elastic Heterogeneity in an Infarcted Human

Following a myocardial infarction, patients who survive the acute effects are still at risk of experiencing adverse ventricular remodelling and eventual heart failure. The material properties of the patient's ventricular tissue play a role in determining the outcome. Overly stiff tissues resist stretching in diastole, which can impair filling function. Conversely, overly compliant but non-contracting tissue can be stretched in systole, thereby wasting energy which could otherwise have been used to pump blood.

In this article we further extend our adjoint-gradient based data assimilation to cover spatial variations in passive material properties, with the goal of creating high resolution models of infarcted hearts. Furthermore, a novel combined pressure-free geometry and material parameter estimation algorithm is developed in order to ensure that model strains and pressures are consistent with those observed in-vivo. Our methods are applied to the case of a patient with a severe myocardial infarction. Good matches to measured regional strain data are obtained in the personalized model.

1.5 Perspectives and Future Work

The two pathologies considered in this thesis, dyssynchrony and myocardial infarction, can lead to large heterogeneities in ventricular tissue properties which are highly specific to a patient. Personalized models of cardiac mechanics should incorporate these heterogeneities in order to make model-based predictions as relevant as possible. In this thesis my coauthors and I have shown that adjoint-gradient based data assimilation methods are able to efficiently and accurately incorporate tissue heterogeneities into personalized ventricular mechanics models. These methods were tested on clinical data from two patients, each of which is representative of one of the two pathologies mentioned above.

Furthermore we have developed an algorithm for computing a personalized reference geometry that matches an intermediate configuration to one observed

in-vivo. This leads to a personalization of passive tissue properties which gives left ventricular cavity pressures and wall strains that are consistent with their corresponding in-vivo measurements.

Further work is required to establish the utility of the adjoint-gradient based methods for clinical purposes. Firstly, more clinical cases need to be considered in order to establish a method that is widely applicable. Secondly, the information provided by the personalized models needs to be tested to see if it can improve the diagnosis and or treatment of cardiac diseases. Finally, the resolution of the heterogeneous parameter fields should be optimized. Higher resolutions can potentially capture more of the details of a patient's specific mechanical situation. Lower resolutions on the other hand can potentially result in simpler optimization problems with less iterations needed to find a minimum, and fewer minima that need to be explored.

Bibliography

[1] Liya Asner, Myrianthi Hadjicharalambous, Radomir Chabiniok, Devis Peresutti, Eva Sammut, James Wong, Gerald Carr-White, Philip Chowienczyk, Jack Lee, Andrew King, et al. Estimation of passive and active properties in the human heart using 3D tagged MRI. *Biomechanics and modeling in mechanobiology*, pages 1–19, 2015.

[2] Kevin F Augenstein, Brett R Cowan, Ian J LeGrice, Poul MF Nielsen, and Alistair A Young. Method and apparatus for soft tissue material parameter estimation using tissue tagged magnetic resonance imaging. *Journal of biomechanical engineering*, 127(1):148–157, 2005.

[3] Radomir Chabiniok, Philippe Moireau, P-F Lesault, Alain Rahmouni, J-F Deux, and Dominique Chapelle. Estimation of tissue contractility from cardiac cine-MRI using a biomechanical heart model. *Biomechanics and modeling in mechanobiology*, 11(5):609–630, 2012.

[4] Radomir Chabiniok, Vicky Y Wang, Myrianthi Hadjicharalambous, Liya Asner, Jack Lee, Maxime Sermesant, Ellen Kuhl, Alistair A Young, Philippe Moireau, Martyn P Nash, et al. Multiphysics and multiscale modelling, data–model fusion and integration of organ physiology in the clinic: ventricular cardiac mechanics. *Interface focus*, 6(2):20150083, 2016.

[5] Kevin D Costa, Jeffrey W Holmes, and Andrew D McCulloch. Modelling cardiac mechanical properties in three dimensions. *Philosophical Transactions of the Royal Society of London A: Mathematical, Physical and Engineering Sciences*, 359(1783):1233–1250, 2001.

[6] Herve Delingette, Florence Billet, Ken CL Wong, Maxime Sermesant, Kawal Rhode, Matthew Ginks, C Aldo Rinaldi, Reza Razavi, and Nicholas Ayache. Personalization of cardiac motion and contractility from images using variational data assimilation. *IEEE transactions on biomedical engineering*, 59(1):20–24, 2012.

[7] Linda L Demer and FC Yin. Passive biaxial mechanical properties of isolated canine myocardium. *The Journal of physiology*, 339:615, 1983.

[8] Socrates Dokos, Bruce H Smaill, Alistair A Young, and Ian J LeGrice. Shear properties of passive ventricular myocardium. *American Journal of Physiology-Heart and Circulatory Physiology*, 283(6):H2650–H2659, 2002.

[9] Longling Fan, Jing Yao, Chun Yang, Zheyang Wu, Di Xu, and Dalin Tang. Material stiffness parameters as potential predictors of presence of left ventricle myocardial infarction: 3D echo-based computational modeling study. *Biomedical engineering online*, 15(1):1, 2016.

[10] Patrick E Farrell, David A Ham, Simon W Funke, and Marie E Rognes. Automated derivation of the adjoint of high-level transient finite element programs. *SIAM Journal on Scientific Computing*, 35(4):C369–C393, 2013.

[11] Julius M Guccione, Andrew D McCulloch, and LK Waldman. Passive material properties of intact ventricular myocardium determined from a cylindrical model. *Journal of biomechanical engineering*, 113(1):42–55, 1991.

[12] Myrianthi Hadjicharalambous, Radomir Chabiniok, Liya Asner, Eva Sammut, James Wong, Gerald Carr-White, Jack Lee, Reza Razavi, Nicolas Smith, and David Nordsletten. Analysis of passive cardiac constitutive laws for parameter estimation using 3D tagged MRI. *Biomechanics and modeling in mechanobiology*, 14(4):807–828, 2015.

[13] Heart and Stroke Foundation. Heart and stroke foundation. `http://www.heartandstroke.com/`, February 2013.

[14] Gerhard Holzapfel and Ray W Ogden. Constitutive modelling of passive myocardium: a structurally based framework for material characterization.

Philosophical transactions. Series A, Mathematical, physical, and engineering sciences, 367(1902):3445–75, sep 2009.

[15] Gerhard A Holzapfel. *Nonlinear solid mechanics:A Continuum Approach for Engineering*. Wiley Chichester, 2000.

[16] Jeremy R McGarvey, Dimitri Mojsejenko, Shauna M Dorsey, Amir Nikou, Jason A Burdick, Joseph H Gorman, Benjamin M Jackson, James J Pilla, Robert C Gorman, and Jonathan F Wenk. Temporal changes in infarct material properties: an in vivo assessment using magnetic resonance imaging and finite element simulations. *The Annals of thoracic surgery*, 100(2):582–589, 2015.

[17] Philippe Moireau and Dominique Chapelle. Reduced-order unscented Kalman filtering with application to parameter identification in large-dimensional systems. *ESAIM: Control, Optimisation and Calculus of Variations*, 17(2):380–405, 2011.

[18] Dimitri Mojsejenko, Jeremy R McGarvey, Shauna M Dorsey, Joseph H Gorman III, Jason A Burdick, James J Pilla, Robert C Gorman, and Jonathan F Wenk. Estimating passive mechanical properties in a myocardial infarction using MRI and finite element simulations. *Biomechanics and modeling in mechanobiology*, 14(3):633–647, 2015.

[19] H Schmid, MP Nash, AA Young, and PJ Hunter. Myocardial material parameter estimation—a comparative study for simple shear. *Journal of biomechanical engineering*, 128(5):742–750, 2006.

[20] H Schmid, P O'Callaghan, MP Nash, W Lin, IJ LeGrice, BH Smaill, AA Young, and PJ Hunter. Myocardial material parameter estimation-a non–homogeneous finite element study from simple shear tests. *Biomechanics and modeling in mechanobiology*, 7(3):161–173, 2008.

[21] H Schmid, W Wang, PJ Hunter, and MP Nash. A finite element study of invariant-based orthotropic constitutive equations in the context of myocardial material parameter estimation. *Computer methods in biomechanics and biomedical engineering*, 12(6):691–699, 2009.

[22] H Schmid, YK Wang, J Ashton, AE Ehret, SBS Krittian, MP Nash, and PJ Hunter. Myocardial material parameter estimation-a comparison of invariant based orthotropic constitutive equations. *Computer methods in biomechanics and biomedical engineering*, 12(3):283–295, 2009.

[23] Gerhard Sommer, Andreas J Schriefl, Michaela Andrä, Michael Sacherer, Christian Viertler, Heimo Wolinski, and Gerhard A Holzapfel. Biomechanical properties and microstructure of human ventricular myocardium. *Acta biomaterialia*, 24:172–192, 2015.

[24] Hari Sundar, Christos Davatzikos, and George Biros. Biomechanically-constrained 4D estimation of myocardial motion. In *Medical Image Computing and Computer-Assisted Intervention–MICCAI 2009*, pages 257–265. Springer, 2009.

[25] Vicky Y Wang, H I Lam, Daniel B Ennis, Brett R Cowan, Alistair a Young, and Martyn P Nash. Modelling passive diastolic mechanics with quantitative MRI of cardiac structure and function. *Medical image analysis*, 13(5):773–84, October 2009.

[26] Ken CL Wong, Maxime Sermesant, Kawal Rhode, Matthew Ginks, C Aldo Rinaldi, Reza Razavi, Hervé Delingette, and Nicholas Ayache. Velocity-based cardiac contractility personalization from images using derivative-free optimization. *Journal of the mechanical behavior of biomedical materials*, 43:35–52, 2015.

[27] Jiahe Xi, Pablo Lamata, Jack Lee, Philippe Moireau, Dominique Chapelle, and Nic Smith. Myocardial transversely isotropic material parameter estimation from in-silico measurements based on a reduced-order unscented Kalman filter. *Journal of the mechanical behavior of biomedical materials*, 4(7):1090–1102, 2011.

[28] Frank CP Yin, Robert K Strumpf, Paul H Chew, and Scott L Zeger. Quantification of the mechanical properties of noncontracting canine myocardium under simultaneous biaxial loading. *Journal of biomechanics*, 20(6):577–589, 1987.

2 Paper I: Adjoint Multi-Start Based Estimation of Cardiac Hyperelastic Material Parameters using Shear Data

Adjoint Multi-Start Based Estimation of Cardiac Hyperelastic Material Parameters using Shear Data

Gabriel Balaban[1,2], Martin S. Alnæs[1], Joakim Sundnes[1,2], Marie E. Rognes[1,3]

1. Simula Research Laboratory, P.O. Box 134 1325 Lysaker, Norway
2. Department of Informatics, University of Oslo, P.O. Box 1080 Blindern 0316 Oslo, Norway
3. Department of Mathematics, University of Oslo, P.O. Box 1053 Blindern 0316 Oslo, Norway

Abstract: Cardiac muscle tissue during relaxation is commonly modelled as a hyperelastic material with strongly nonlinear and anisotropic stress response. Adapting the behavior of such a model to experimental or patient data gives rise to a parameter estimation problem which involves a significant number of parameters. Gradient-based optimization algorithms provide a way to solve such nonlinear parameter estimation problems with relatively few iterations, but require the gradient of the objective functional with respect to the model parameters. This gradient has traditionally been obtained using finite differences, the calculation of which scales linearly with the number of model parameters, and introduces a differencing error. By using an automatically derived adjoint equation, we are able to calculate this gradient more efficiently, and with minimal implementation effort. We test this adjoint framework on a least squares fitting problem involving data from simple shear tests on cardiac tissue samples. A second challenge which arises in gradient-based optimization is the dependency of the algorithm on a suitable initial guess. We show how a multi-start procedure can alleviate this dependency. Finally, we provide estimates for the material parameters of the Holzapfel and Ogden strain energy law using finite element models together with experimental shear data.

2.1 Introduction

The personalization of computational models in cardiology is a key step towards making models useful in clinical practice and cardiac surgery. A computational model, once properly calibrated, has the potential to forecast cardiac function and disease, and can aid in planning treatments and therapies. To describe the mechanical function of the heart, the passive elasticity of the muscle tissue needs to be represented. Personalizing the effects of this elasticity in a computational model is typically accomplished by tuning a set of material parameters so that the output of the model fits observed data. Gradient-based optimization algorithms have successfully been used in the past to automatically perform the parameter tuning at an organ scale [2, 28]. In these studies, the gradient of the objective functional is approximated using one-sided finite differences.

Compared to using a global optimization method, local gradient-based methods have the advantage of using relatively few optimization iterations. This is an important consideration when optimizing organ scale finite element models, for which running a single forward model can take hours or days. On the other hand, a disadvantage of using local optimization methods is the fact that they can converge to local, globally suboptimal, minima. One way to combine the speed of a local optimization with the robustness of a global optimization is to use the multi-start method. In this method, many local optimizations are run starting from various points in parameter space and the best fitting solution of the group is taken to be the global optimum.

Another popular approach to parameter fitting is the reduced order unscented Kalman filter. This approach was successfully used to fit a transversely isotropic passive mechanics model to synthetic data [30], to partially calibrate a multi-physics model [20], and to estimate regional contractility parameters [5]. Note however that the use of both unscented Kalman filtering and finite differences carries a computational cost that increases with the number of model parameters.

Assuming there are k parameters to be estimated, an unscented Kalman filter with a minimal sigma-point configuration requires $k + 1$ model evaluations at a single time level for each assimilated data point. An evaluation of a finite difference derivative on the other hand requires $k + 1$ runs of the model throughout the full span of model configurations considered.

In contrast to these two techniques, the adjoint approach computes the objective functional gradient via the solution to an adjoint equation, which involves only a single solve of a linearized system for any number of model parameters. Thus, for models involving many parameters, either due to model complexity or spatiotemporal parameter variation, the adjoint approach offers a computationally attractive approach for parameter estimation.

There are some previous results involving adjoint equations and cardiac elasticity. Sundar et al. (2009) developed a framework for the estimation of wall motion based on cine-MRI images and adjoint inversion [25], and Delingette et al. (2012) used an adjoint equation to estimate contractility para meters [7]. However, both of these studies involve linear and isotropic elasticity models, which represent a significant simplification of the orthotropic and highly nonlinear behavior reported in the contemporary cardiac mechanics literature [6, 8, 15].

One reason why it is difficult to use an adjoint equation with modern nonlinear anisotropic models is the complexity required in deriving and implementing code for the solution of the adjoint problem. In order to resolve this issue, we make use of an automatic framework for generating adjoint code [9]. Here, we use this adjoint framework to estimate the material parameters of an invariant-based orthotropic myocardial strain energy law (the Holzapfel-Ogden model) [15]. This law is embedded here in an incompressible finite element framework, and we use the raw data from a simple shearing experiment [8] as a target for optimization. These data have previously been used to estimate material parameters for a variety of other strain energy functions using a finite element framework, but with a gradient obtained using finite differences [23, 24]. The material parameters of the particular strain energy density that we are using have also been previously estimated using digitized data based on Figure 6 of [8], and a homogeneous deformation model [12, 15, 27]. Our study is however the first to use the adjoint approach for the estimation of cardiac hyperelasticity parameters and the first to provide optimized material parameters for the incompressible Holzapfel-Ogden model for non-homogeneous deformations.

The rest of this paper is organized as follows. In Section 2.2 we describe the variational formulation of the elasticity model, the optimization problem for identifying the material parameters, and how the adjoint gradient formula can be used to calculate a functional gradient. In Section 2.3 we describe the verification

of the forward and inverse solvers, present timings to show the efficiency of the adjoint method, and show the results of parameter estimations. Finally, we test a multi-start optimization method in order to reduce the dependence of the gradient-based algorithm on the choice of initial parameter set. We conclude by discussing our findings in Section 2.4, and drawing some conclusions in Section 2.5.

2.2 Mathematical models and methods

We shall use the notion of the directional derivative frequently throughout. For a functional $f : Y \to \mathbb{R}$ for some vector space Y, we define the directional derivative of f with respect to the argument named $\mathbf{y}$ in the direction $\delta\mathbf{y}$

$$D_{\mathbf{y}} f(\mathbf{y})[\delta\mathbf{y}] \equiv \frac{\partial}{\partial \epsilon} f(\mathbf{y} + \epsilon\, \delta\mathbf{y})\Big|_{\epsilon=0}.$$

Furthermore we denote the total derivative by the usual notation $\frac{Df}{Dy}$ to mean the derivative of f with respect to all arguments depending on y.

2.2.1 Hyperelasticity model

Let $\Omega \subset \mathbb{R}^3$ be an open and bounded domain with coordinates $\mathbf{X}$ and boundary $\partial\Omega$, occupied by an incompressible hyperelastic body. We consider the quasi-static regime of a body undergoing a large deformation $\mathbf{x} = \mathbf{x}(\mathbf{X})$ and are interested in finding the displacement $\mathbf{u} = \mathbf{u}(\mathbf{X}) = \mathbf{x} - \mathbf{X}$ and the hydrostatic pressure $p = p(\mathbf{X})$ that minimize the incompressible strain energy $\Pi = \Pi(\mathbf{u}, p, \mathbf{m})$:

$$\Pi(\mathbf{u}, p, \mathbf{m}) = \int_\Omega \psi(\overline{\mathbf{C}}, \mathbf{m}) + p(J-1)\,\mathrm{dx} \tag{2.1}$$

over the space of admissible displacements and pressures satisfying any given Dirichlet boundary conditions. In (2.1), $\mathbf{m}$ is a set of material parameters, $J = \det \mathbf{F}$, where $\mathbf{F} = \mathrm{Grad}\mathbf{x} = \mathrm{Grad}\mathbf{u} + \mathbf{I}$ denotes the deformation gradient, $\mathbf{I}$ is the identity tensor in $\mathbb{R}^3$, $\overline{\mathbf{C}} = J^{-\frac{2}{3}}\mathbf{F}^T\mathbf{F}$ denotes a volume-preserving right Cauchy-Green tensor, and ψ denotes an isochoric strain energy density.

The incompressible Holzapfel and Ogden hyperelasticity model [15] describes large deformations and stresses in cardiac tissue via the following energy density

ψ:

$$\begin{aligned}\psi(\overline{\mathbf{C}},\mathbf{m}) = &\frac{a}{2b}\left(\exp\left[b(I_1(\overline{\mathbf{C}})-3)\right]-1\right)\\ &+\sum_{i=f,s}\frac{h(I_{4i}(\overline{\mathbf{C}}))a_i}{2b_i}\left(\exp\left[b_i(I_{4i}(\overline{\mathbf{C}})-1)^2\right]-1\right)\\ &+\frac{a_{fs}}{2b_{fs}}\left(\exp\left[b_{fs}I_{8fs}^2(\overline{\mathbf{C}})\right]-1\right).\end{aligned} \tag{2.2}$$

Here f, s denote fiber and sheet directions, respectively; $h(x)$ is a Heaviside function with a jump at $x = 1$, and the material parameters are

$$\mathbf{m} = (a, b, a_f, b_f, a_s, b_s, a_{fs}, b_{fs}). \tag{2.3}$$

Moreover, $I_1, I_{4s}, I_{4f}, I_{8fs}^2$ are rotation invariant functions given by

$$\begin{aligned} I_1(\overline{\mathbf{C}}) &= tr\overline{\mathbf{C}}\\ I_{4i}(\overline{\mathbf{C}}) &= \mathbf{e}_i\cdot\overline{\mathbf{C}}\mathbf{e}_i \quad i=f,s\\ I_{8fs}(\overline{\mathbf{C}}) &= \mathbf{e}_s\cdot\overline{\mathbf{C}}\mathbf{e}_f\end{aligned} \tag{2.4}$$

where tr denotes the tensor trace and $\mathbf{e}_f, \mathbf{e}_s$ denote unit vectors pointing in the local myocardial fiber and sheet directions [15]. The strain energy density ψ is rotation-invariant, and polyconvex if $\mathbf{m} > \mathbf{0}$ [15].

The Euler-Lagrange equations for the minimizing displacement $\mathbf{u}$ and pressure p of (2.1) read: for given $\mathbf{m}$, find $\mathbf{w} = (\mathbf{u}, p)$ such that

$$R(\mathbf{w}, \mathbf{m}; \delta\mathbf{w}) \equiv D_{\mathbf{u},p}\Pi(\mathbf{u}, p, \mathbf{m})[\delta\mathbf{u}, \delta p] = 0, \tag{2.5}$$

for all admissible virtual variations $\delta\mathbf{w} = (\delta\mathbf{u}, \delta p)$. Inserting the total potential energy from (2.1) and taking the directional derivatives, we obtain

$$D_{\mathbf{u},p}\Pi(\mathbf{u}, p, \mathbf{m})[\delta\mathbf{u}, \delta p] = \int_\Omega \left(\left(\frac{\partial\psi(\overline{\mathbf{C}},\mathbf{m})}{\partial\mathbf{F}} + pJ\mathbf{F}^{-T}\right) : \mathrm{Grad}\delta\mathbf{u} + (J-1)\delta p\right)\,\mathrm{dx}. \tag{2.6}$$

2.2.2 Parameter estimation as a PDE-constrained optimization problem

In the general case, the passive material parameters $\mathbf{m}$ entering the constitutive relationship (2.2) are not known. In order to estimate these parameters from data, we propose to use a numerical approximation in combination with a gradient-based optimization algorithm in which the gradients are computed via an adjoint model. The optimization algorithm seeks to minimize the misfit between model output and observations. Denoting the misfit functional by $I = I(\mathbf{w}(\mathbf{m}), \mathbf{m})$, the optimization problem reads:

$$\min_{\mathbf{m}} I(\mathbf{w}(\mathbf{m}), \mathbf{m}) \qquad \text{subject to} \qquad R(\mathbf{w}, \mathbf{m}; \delta\mathbf{w}) = 0 \quad \forall \delta\mathbf{w} \in W, \tag{2.7}$$

together with suitable Dirichlet boundary conditions on $\mathbf{w}$. We also require that $\mathbf{m} > 0$ to ensure the functional (2.1) is polyconvex [15]. For notational convenience we will sometimes use the reduced formulation of the misfit functional and its gradient with respect to the material parameters $\mathbf{m}$. In particular, we introduce the reduced functional $\hat{I}$

$$\hat{I}(\mathbf{m}) \equiv I(\mathbf{w}(\mathbf{m}), \mathbf{m}). \tag{2.8}$$

In our numerical experiments we use Sequential Least Squares Programming (SLSQP) as implemented in [**?**] and wrapped in the package SciPy [17] in order to solve (2.7).

2.2.3 Multi-start Optimization

A common challenge with gradient-based algorithms is that the solution obtained depends on the choice of initialization point for the algorithm. Moreover, the optimized solution may be a local minimum only and not necessarily a global minimum. One way to attack these issues is to run many optimizations from randomly chosen initial parameter points, and to chose the resulting optimized material parameter set that gives the best fit. This method is often referred to as multi-start optimization [4] and is an example of combining global and local optimization.

Due to the presence of exponential functions in the strain energy (2.2), it is

possible for calculated stresses to become very large, which may result in convergence issues for the numerical solution of the Euler-Lagrange equation (2.5). This can easily occur if several material parameters have large values. In order to minimize this problem we have designed a procedure to generate random initial guesses which limits the number of large material parameter values while still allowing for a large range of initial possible values for each parameter. The procedure works as follows: first set a maximum parameter value P_{max}. Then choose N (with $N = 8$ in our case) points $p_i,\ i \in \{1, 2, 3...n\}$, from a uniform distribution defined over the interval $[0, P_{max}]$ and let $p_0 = 0$. The parameter values m_i are then set to be the distances between successive randomly drawn points, that is $m_i = p_i - p_{i-1}$.

2.2.4 Computing the functional gradient via the adjoint solution

Gradient-based optimization algorithms in general, and the SLSQP algorithm in particular, rely on the total derivative of the objective functional (2.8). By introducing an *adjoint* state variable, this derivative may be computed efficiently. We summarize this result below. Our presentation is based on [14], and is adapted here to the solid mechanics setting.

We define three abstract spaces W, M, and Φ, where W is the space of all possible solutions to the variational equation (2.5) which also satisfy any given Dirichlet boundary conditions, M is the material parameter vector space, and Φ is the space of virtual variations. The Lagrangian $L : W \times M \times \Phi \to \mathbb{R}$ is defined as:

$$L(\mathbf{w}, \mathbf{m}, \phi) = I(\mathbf{w}, \mathbf{m}) - R(\mathbf{w}, \mathbf{m}; \phi). \tag{2.9}$$

For all $\mathbf{m} \in M$, $\mathbf{w} \in W$ solving the state equation (2.5), we have

$$\frac{D}{D\mathbf{m}} R(\mathbf{w}(\mathbf{m}), \mathbf{m}; \phi) = 0,$$

such that the total derivatives of I and L coincide,

$$\frac{D}{D\mathbf{m}} I(\mathbf{w}(\mathbf{m}), \mathbf{m}) = \frac{D}{D\mathbf{m}} L(\mathbf{w}(\mathbf{m}), \mathbf{m}, \phi). \tag{2.10}$$

If we choose $\phi \in \Phi$ such that

$$D_{\mathbf{w}} L(\mathbf{w}, \mathbf{m}, \phi)[\delta \mathbf{w}] = 0 \tag{2.11}$$

for all $\delta \mathbf{w} \in W$, which in particular includes $\delta \mathbf{w} = D_{\mathbf{m}} \mathbf{w}(\mathbf{m})[\delta \mathbf{m}]$, the total derivative of L with respect to $\mathbf{m}$ in the direction $\delta \mathbf{m}$ simplifies as follows using the chain rule:

$$\begin{aligned} \frac{D}{D\mathbf{m}} L(\mathbf{w}(\mathbf{m}), \mathbf{m}, \phi) &= D_{\mathbf{w}} L(\mathbf{w}, \mathbf{m}, \phi)[D_{\mathbf{m}} \mathbf{w}(\mathbf{m})[\delta \mathbf{m}]] + D_{\mathbf{m}} L(\mathbf{w}, \mathbf{m}, \phi)[\delta \mathbf{m}] \\ &= D_{\mathbf{m}} L(\mathbf{w}, \mathbf{m}, \phi)[\delta \mathbf{m}] \end{aligned} \tag{2.12}$$

Then, for any infinitesimal variation in the material parameters $\delta \mathbf{m}$, combining (2.10), (2.12), and (2.9) yields an efficient evaluation formula, not requiring derivatives of the state variable $\mathbf{w}$ with respect to the material parameters $\mathbf{m}$, for the total derivative of I:

$$\frac{D}{D\mathbf{m}} I(\mathbf{w}(\mathbf{m}), \mathbf{m}) = D_{\mathbf{m}} I(\mathbf{w}, \mathbf{m})[\delta \mathbf{m}] - D_{\mathbf{m}} R(\mathbf{w}, \mathbf{m}, \phi)[\delta \mathbf{m}]. \tag{2.13}$$

We still need to compute ϕ. By defining the form $R_{\mathbf{w}}$ and its adjoint $R^*_{\mathbf{w}}$,

$$\begin{aligned} R_{\mathbf{w}}(\mathbf{w}, \mathbf{m}; \delta \mathbf{w}, \phi) &\equiv D_{\mathbf{w}} R(\mathbf{w}, \mathbf{m}; \phi)[\delta \mathbf{w}], \\ R^*_{\mathbf{w}}(\mathbf{w}, \mathbf{m}; \phi, \delta \mathbf{w}) &\equiv R_{\mathbf{w}}(\mathbf{w}, \mathbf{m}; \delta \mathbf{w})[\phi], \end{aligned}$$

we can rewrite (2.11) as

$$D_{\mathbf{w}} L(\mathbf{w}, \mathbf{m}, \phi)[\delta \mathbf{w}] = D_{\mathbf{w}} I(\mathbf{w}, \mathbf{m})[\delta \mathbf{w}] - R^*_{\mathbf{w}}(\mathbf{w}, \mathbf{m}; \phi, \delta \mathbf{w}) = 0,$$

and thus recognize the adjoint equation: given $\mathbf{m}$, $\mathbf{w}$, find $\phi \in \Phi$ such that

$$R^*_{\mathbf{w}}(\mathbf{w}, \mathbf{m}; \phi, \delta \mathbf{w}) = D_{\mathbf{w}} I(\mathbf{w}, \mathbf{m})[\delta \mathbf{w}] \tag{2.14}$$

for all $\delta \mathbf{w} \in W$.

In summary, the adjoint-based gradient evaluation formula is: given $\mathbf{m}$, first compute $\mathbf{w}$ by solving the state equation (2.5), next compute ϕ by solving (2.14),

and finally evaluate (2.13).

2.2.5 Description of shearing experiments

We aim to optimize the material parameters of the Holzapfel-Ogden model (2.2) with respect to target experimental data, in particular data resulting from an earlier set of simple shearing experiments [8]. In these experiments, 6 pig hearts were extracted. From each heart, three adjacent $3\text{mm} \times 3\text{mm} \times 3\text{mm}$ cubic blocks were cut in such a way that the sides of the cubes were aligned with the local myocardial fiber and sheet directions. A device held two opposing faces of each cube between two plates using an adhesive. The top plate was displaced in order to put each specimen in simple shear. For each specimen 6 different modes of shear were tested. These modes are described using the F, S, N coordinate system, which refer to the myocardial fiber, sheet and sheet normal directions, respectively. Each mode is denoted by two letters, where the first defines the normal of the face of the cube that is being displaced, and the second refers to the direction of displacement. These 6 modes are FS, FN, SF, SN, NF, NS.

In order to remove the effects of strain softening, preliminary displacements were applied to the tissue samples until no further softening was observed. After that, displacements were once again applied, and the forces in the shear direction were measured on the top plate. These measurements were taken for circa $200 - 250$ various states of shear per mode.

In Figure 2.1 we display the stress-strain relations for positive displacements that were obtained from the shearing experiments [8]. As can be seen in Figures 4 and 6 of [8] the experimentally obtained curves contain a high degree of symmetry through the line $y = -x$. We can expect the same symmetry in the stresses computed by finite element models which use the strain energy (2.2) since changing the sign of the displacement map will change the sign of the resulting stresses but preserve their magnitude. In the previous studies [15], [12], and [27], only the data for positive shear displacements were used. For the sake of comparability, we restrict our data in the same way.

In our numerical experiments we use two data sets with reference to the numbering of [8]. The first is Data Set 6, and the second data is Data Set 2 with the SF and SN curves swapped. This swap and the choice of data sets are discussed

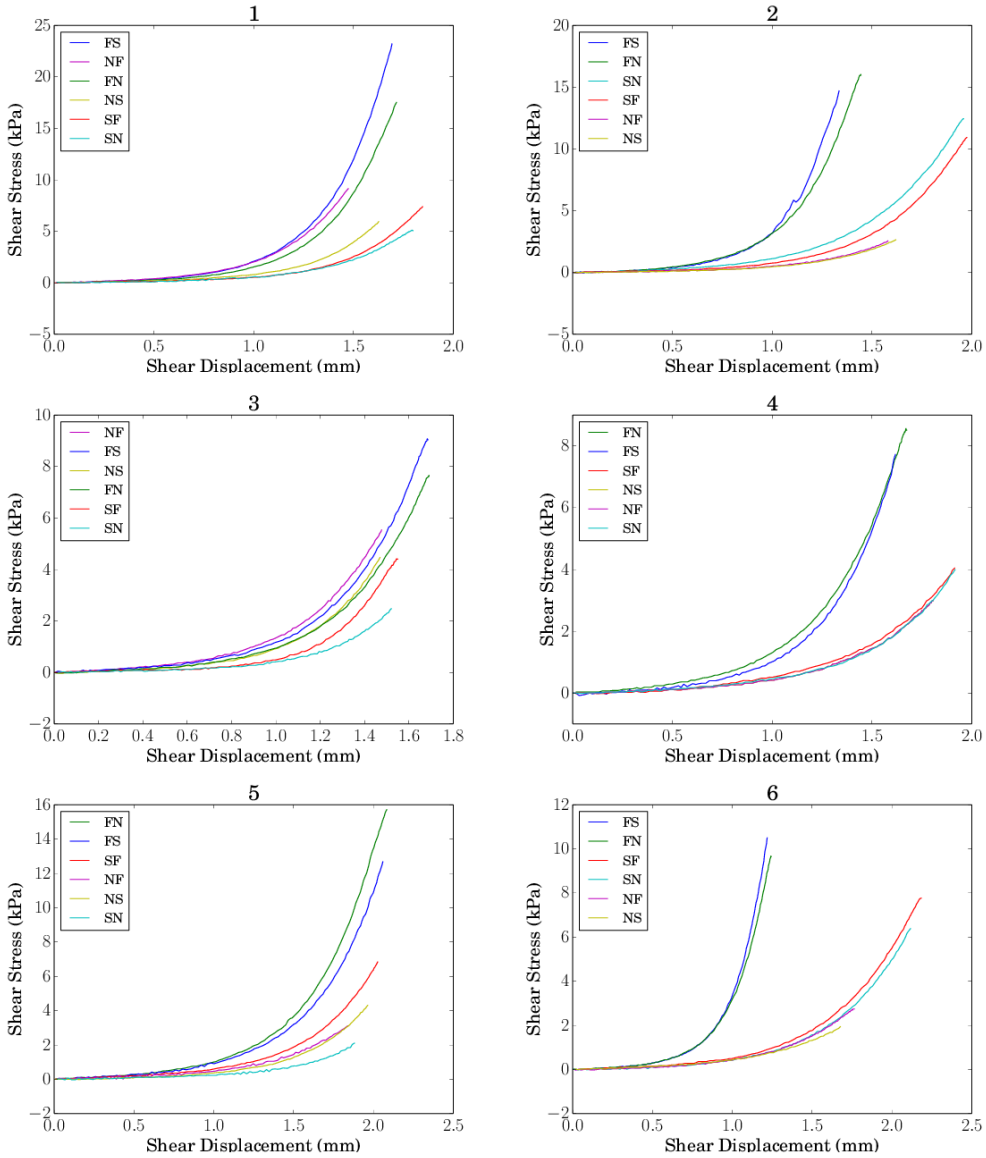

Figure 2.1: Stress-strain relations, numbered 1 through 6, obtained from simple shearing experiments performed on 3mm $\times$ 3mm $\times$ 3mm cubes of myocardium extracted from 6 porcine hearts. The modes are ordered from highest to lowest stiffness in each experiment. The data originates from the study [8], but were not published in the subsequent article. In Experiment 4 the data for one of the NS-NF curves was copied into the other before we received it, so the two curves lie here on top of one another.

further in Section 2.4. For clarity, we shall refer to Data Set 6 as "transversely isotropic" and Data Set 2 with the swap as "orthotropic", as the respective stress-strain curves are typical of materials of these types. For each mode, the prescribed shear displacement is modelled as a Dirichlet boundary condition for the displacement on the respective top and bottom faces in the respective direction.

2.2.6 Choice of objective functional

In order to estimate the passive material parameters of the Holzapfel-Ogden model, we make use of a least squares objective functional. This functional defines a distance from the model output to the data points of the shearing experiment, and we seek the material parameter set $\mathbf{m}$ that minimizes this. Before introducing our objective functional, we define the set of directions $\mathcal{D} = \{F, S, N\}$, referring to fiber, sheet and sheet normal directions. We also use the notation (i, j) to refer to a mode, with the index i referring to the normal of the face that is shifted, and j to the direction in which the shift occurs.

Our fit function is similar to that used in [22], and is given by

$$\hat{I}(\mathbf{m})^2 = \sum_{i\in\mathcal{D}} \sum_{j\in\mathcal{D}} \sum_{k=1}^{G} \omega_k \left(t^{i,j}_{\text{model}}(c_k, \mathbf{m}) - t^{i,j}_{\text{exper}}(c_k) \right)^2 \tag{2.15}$$

In (2.15), $t^{i,j}_{\text{exper}}$ is the force measured during the experiment, and $t^{i,j}_{\text{model}}$ is the force generated by the finite element model at each prescribed shear displacement $c_k \in [0, C^{i,j}]$, where $C^{i,j}$ is the maximal prescribed displacement of the mode (i, j) in the experiment. Each c_k is chosen to be a Gauss point of a G-point Gauss integration rule defined over $[0, C^{i,j}]$, and ω_k is the value of the Gauss weight related to c_k. Explicitly, for mode (i, j) with top face $\partial\Omega_i$, $t^{i,j}_{\text{model}}$ is given by

$$t^{i,j}_{\text{model}}(c_k, \mathbf{m}) = \int_{\partial\Omega_i} \frac{\partial\psi(\mathbf{u}(c_k), \mathbf{m})}{\partial \mathbf{F}_{i,j}} \, \text{dS}, \tag{2.16}$$

where $\mathbf{F}_{i,j} = \mathbf{e}_i \cdot \mathbf{F}\mathbf{e}_j$ is a shear component of the deformation gradient.

Evaluating the inner loop of $\hat{I}$ requires solving (2.5) once for each given shear displacement c_k. The motion given by the calculated displacements is then a quasi-static approximation of the motion undergone by the corresponding tissue

in the shearing experiment.

Following [22], we evaluate the least squares fit (2.15) at G Gauss integration points, rather than for all 250 recorded points for each shear mode, in order to greatly reduce the computational expense of evaluating $\hat{I}$. At each Gauss point we obtain the corresponding shear stress by linearly interpolating between the two neighbouring stresses which were recorded in the experiments of Dokos et al. [8].

The use of Gauss integration is based on the observation that $\hat{I}(\mathbf{m})$ is an approximation to the following expression

$$\left(\sum_{j \in \mathcal{D}} \sum_{i \in \mathcal{D}} \int_0^{C^{i,j}} \left(t^{i,j}_{\text{model}}(c, \mathbf{m}) - t^{i,j}_{\text{exper}}(c) \right)^2 \, dc \right)^{\frac{1}{2}}. \tag{2.17}$$

By setting $t^{i,j}_{\text{model}} = 0$ and approximating the integral by the midpoint rule applied to the full dataset we can determine the quality of the Gauss approximation. In order to do this we define the relative error

$$\epsilon_{rel} = \left| \frac{\hat{I} - \hat{I}_{mid}}{\hat{I}_{mid}} \right|, \tag{2.18}$$

where I_{mid} is the midpoint rule approximation of (2.17) evaluated over the full data, and I, given by (2.15), is evaluated at a reduced set of Gauss points. We noticed that 9 Gauss points are sufficient to reduce ϵ_{rel} to less than 0.01. However, in our numerical experiments we use $G = 40$ Gauss points as this guaranteed small enough changes in the solution of the Euler-Lagrange equation (2.5) from one Gauss point to the next, so that our Newton's method solution of (2.5) always converged.

2.2.7 Finite element discretization of the hyperelasticity equations

We represent each tissue sample of the shearing experiments by a three-dimensional cube $\Omega = [0, 3]^3$ (mm^3). An $N \times N \times N$ mesh of this cube was constructed by uniformly dividing the mesh into $N \times N \times N$ boxes and then subdividing the boxes

into tetrahedra. The local myocardial fiber and sheet orientations were represented as spatially constant vectors aligned with the coordinate axes.

On these geometries, we solve (2.5) and its adjoint, using a Galerkin finite element method with the Taylor-Hood finite element pair [16]; e.g. a continuous piecewise quadratic vector field for the displacement and a continuous piecewise linear scalar field for the pressure. For the solution of the nonlinear system of equations, we use a Newton trust region method. The absolute tolerance of the nonlinear solver was set to 10^{-10} in the numerical experiments below. Linear systems are solved by LU factorization.

Additionally, we model the case of a homogeneous deformation which corresponds to a linear displacement with a constant shear angle throughout the domain. Such a model can be represented by discretizing the cubes with a single layer of linear finite elements: the resulting displacement is completely determined by the prescribed boundary conditions. Figure 2.2 illustrates the two kinds of deformations on cube meshes.

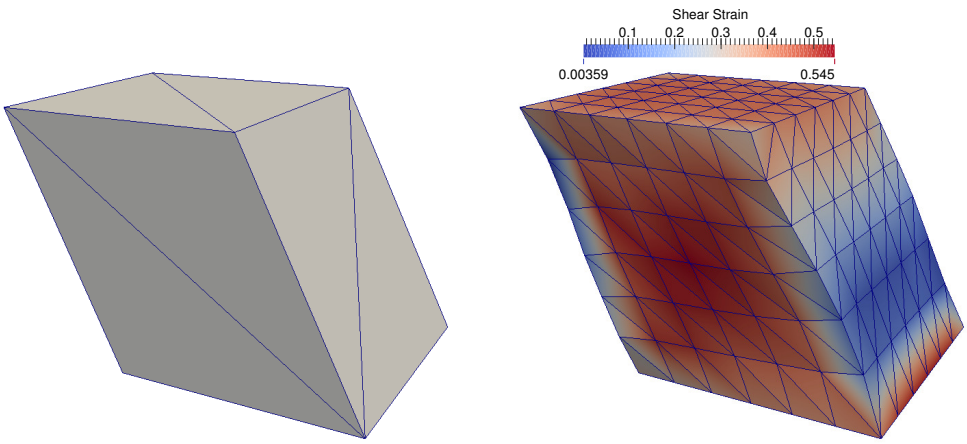

Figure 2.2: Finite element representation of cubes of cardiac tissue undergoing simple shear in the NS mode. The bottom of the cube is fixed and the top displacement is given. Left: homogeneous deformation with a constant shear angle. Right: finite element solution on a $6 \times 6 \times 6$ mesh. The plot shows the value of the NS-component of the right Cauchy Green tensor $\mathbf{C}$.

The discrete variational formulation of the Euler-Lagrange equations is implemented using the FEniCS Project software [1, 19] and dolfin-adjoint [9]. From a FEniCS forward model, dolfin-adjoint automatically generates the symbolic adjoint system of equations and computes the functional gradient (2.13) using the adjoint solution. The FEniCS framework automatically generates and compiles efficient C++ code for the assembly of the relevant linear systems from the symbolic representations of both forward and adjoint equations, and solves the nonlinear and linear systems using e.g. PETSc [3]. With this setup, we observed that a typical solution of the Euler-Lagrange equation (2.5) takes 6 Newton iterations.

2.3 Numerical Results

2.3.1 Verification

Each of the finite element, adjoint, and optimization solvers have been carefully verified, separately and combined, as follows:

(i) The finite element solver was verified by the method of manufactured solutions [21]. Following this method we chose an analytic expression for the displacement and pressure fields

$$\begin{aligned} \mathbf{u} &= \left(tx^3,\ y\left(\tfrac{1}{3tx^2+1} - 1\right), 0\right) \\ p &= 0. \end{aligned} \tag{2.19}$$

Here x, y refer to Cartesian coordinates and t is a scaling parameter which we set to $t = 0.2$. Using this analytic expression we derived Dirichlet boundary conditions over a unit cube, and a loading term f which satisfied a pointwise form of equation (2.6)

$$\frac{\partial \psi(\overline{\mathbf{C}}, \mathbf{m})}{\partial \mathbf{F}} + pJ\mathbf{F}^{-T} = f \quad \text{in } \Omega. \tag{2.20}$$

Note that the chosen displacement field satisfies the incompressibility constraint $J - 1 = 0$. We then computed finite element approximations to (2.19) and observed the expected second-order convergence of the displacement gradient to the analytical displacement gradient [16].

(ii) We verified the computation of stresses in the finite element model by prescribing a homogeneous deformation and comparing the resulting numerically

integrated top face shear stress values to analytically computed values. The analytic values were based on the calculations found in [15, Section 5a] and the numerical values were observed to match closely.

(iii) We confirmed the correctness of the adjoint gradients by considering the linearization of the functional $\hat{I}(\mathbf{m})$ around $\mathbf{m}$ with perturbation $\Delta\mathbf{m}$ and using Taylor's theorem: the expression

$$\hat{I}(\mathbf{m}) - \hat{I}(\mathbf{m} + \Delta\mathbf{m}) + \frac{D\hat{I}(\mathbf{m})}{D\mathbf{m}}(\Delta\mathbf{m}) = O(\Delta\mathbf{m}^2) \tag{2.21}$$

converged to 0 at a rate of 2 as $\Delta\mathbf{m} \longrightarrow 0$, which can only be expected if $\frac{D\hat{I}(\mathbf{m})}{D\mathbf{m}}$ is computed accurately.

2.3.2 Parameter estimation with synthetic data

Additionally, we verified the optimization solver by performing a synthetic data test. In this test we chose a target set of material parameters, Table 2.1, 2nd line, and used them to compute synthetic integrated stress values for all 6 shear modes of the tissue experiment [8]. These synthetic stresses were then matched by an optimization starting from material parameter values 25% higher than the target.

We performed this test using our two models for deformation. The first model assumed a homogeneous shear angle through the material and the second model was a finite element model with a $1 \times 1 \times 1$ mesh. Since the displacement field of the finite element model was element-wise quadratic, it allowed for more flexibility in the deformation field. The results of this synthetic data test are presented in Table 2.1 and show that the optimization algorithm was able to closely match the target material parameters.

2.3.3 Parameter estimation with experimental stress data

In the following, we present the results of fitting the Holzapfel-Ogden strain energy law (2.2) using the objective function (2.15) and a SLSQP optimizer with bound constraints. The SLSQP algorithm makes use of the gradient of the objective functional which we obtain using the adjoint gradient formula (2.13).

Table 2.1: Synthetic data test results. The first row (Initial) contains the material parameter values used to initialize the algorithm, while the second row (Target) contains the parameters that were used to generate the synthetic stresses. The rows marked 'Homogeneous' and 'Finite Element' contain optimized parameter values coming from homogeneous deformation and finite element models. These optimized values are matched perfectly by the optimized homogeneous model and very closely by the finite element model.

	a (kPa)	b	a_f (kPa)	b_f	a_s (kPa)	b_s	a_{fs} (kPa)	b_{fs}	I (mN)
Initial	0.059	8.023	18.472	16.026	2.481	11.120	0.216	11.436	
Target (80%)	0.047	6.418	14.778	12.821	1.985	8.896	0.173	9.149	
Homogeneous	0.047	6.418	14.778	12.821	1.985	8.896	0.173	9.149	4.611×10^{-8}
Finite Element	0.047	6.406	14.778	12.821	1.983	8.938	0.173	9.155	0.00082

As the numerical solution of the nonlinear Euler-Lagrange equation (2.5) easily fails to converge when a material parameter becomes too small, we set a lower bound of 1.0×10^{-2} on the components of $\mathbf{m}$ while optimizing finite element models. This bound was not necessary for the homogeneous deformation models as no Euler-Lagrange equation is solved. All optimizations were carried out until the optimizer was unable to further reduce the objective functional or an absolute tolerance of 1.0×10^{-6} in the 2-norm of the functional gradient was reached.

Material parameter estimation using *a priori* knowledge

The material parameters of the Holzapfel-Ogden model have previously been estimated using a homogeneous deformation model (Table 1, 2nd row in [15]). We first used these values as the initial values for optimization of our homogeneous model targeting the transversely isotropic and orthotropic data sets. The optimized results are listed in Table 2.2 with the label Homogeneous.

We next consider finite element models that allow for heterogeneous shear displacements. Beginning with a $1 \times 1 \times 1$ cube and the optimal material parameters from the homogeneous model as initial values, we computed optimal values for the $1 \times 1 \times 1$ case. This procedure was repeated for $N \times N \times N$ cubes with $N = 2, 4, 6, 8$, using the results of the previous optimization as the initial condi-

tion for the next case. The resulting parameter values are presented in Table 2.2, and the corresponding optimal stress-strain curves are shown in Figure 2.3.

We note that going from $N = 8$ to $N = 10$ using both the transversely isotropic and the orthotropic data does not change the material parameters rounded to two 2 significant digits, and therefore consider our finite element models to be sufficiently refined at this resolution. We also note that the fit values, I, decreased with mesh refinement up to about 2 digits accuracy. We expect this decrease since increased mesh refinement gives more flexibility in the deformation field of the finite element model.

Material parameter estimation using multi-start optimization

In this section, we present the results of using the multi-start method to estimate the optimal material parameters, rather than relying on a good initial guess. For the calculation of random initial guesses we set $P_{max} = 40$, cf. Section 2.2.3. This value is close to the largest material parameter found in Table 2.2. Note that this choice gives a conservative set of initial parameters for the optimization algorithm (low initial values) which in turn enhances the robustness of the procedure. We also set 60 as an upper bound for each material parameter value during the optimization. Without this upper bound we observed that many optimizations crashed or converged to suboptimal local minima.

In each multi-start experiment, 30 random starting points were used. The mesh fineness was set to the level of $N = 8$, which was sufficient to give converged material parameter sets when using a priori knowledge in Section 2.3.3. In Table 2.3 we present the best fitting results of the multi-start experiments and note that they are very close to those obtained with a priori knowledge in Table 2.2.

Objective functional values for alternative material parameters

Several other studies [12, 15, 27] have used of the Dokos et al. 2002 shear data [8] to calibrate the Holzapfel and Ogden strain energy (2.2). These studies used homogenized deformation models for the optimization. In Table 2.4 we list the computed objective functional value of parameter sets originating from previous

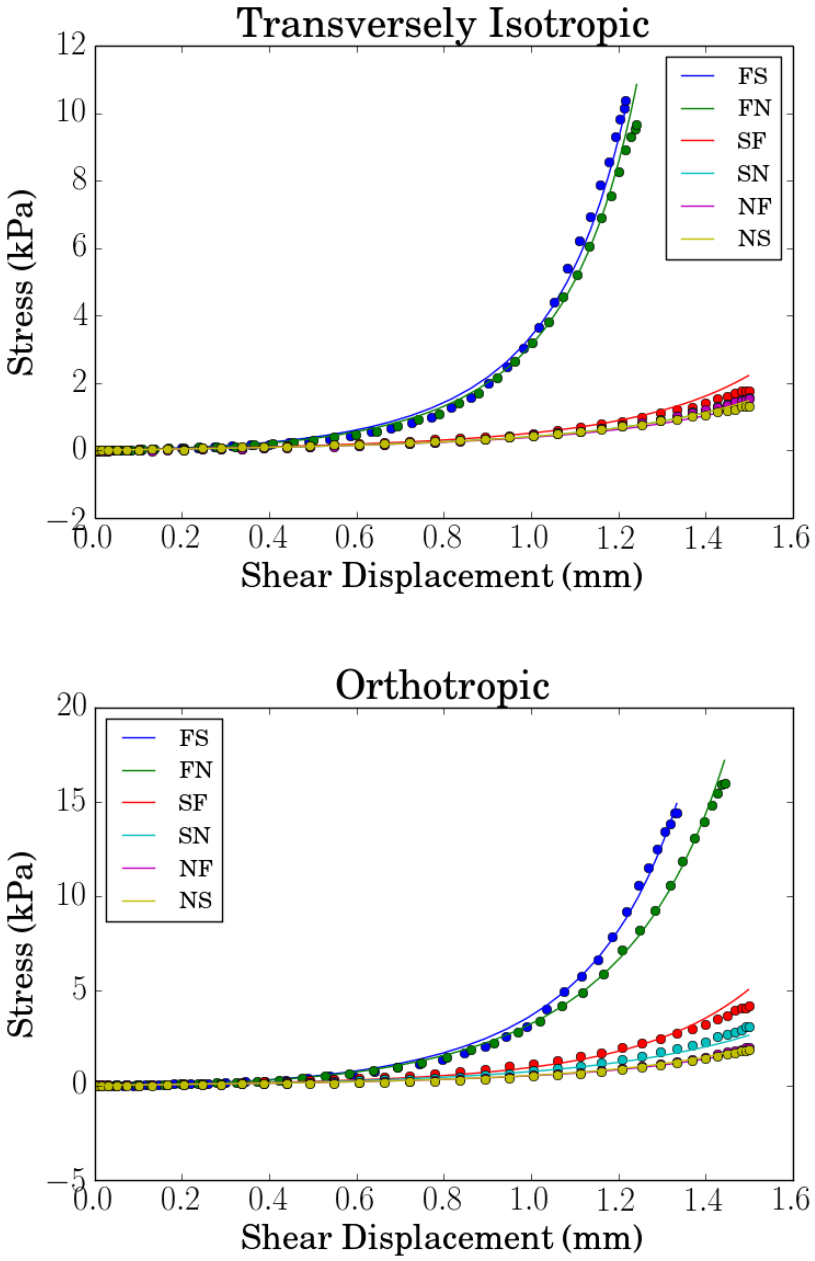

Figure 2.3: Comparison of optimized model stress-strain curves with experimental data. The dots are interpolated experimental data at Gauss points, the solid lines show the output of the finite element models with $N = 8$ elements per edge of the cube.

	a (kPa)	b	a_f (kPa)	b_f	a_s (kPa)	b_s	a_{fs} (kPa)	b_{fs}	I (mN)	Ev.	Grad Ev.
Transversely Isotropic											
Homogeneous	0.544	6.869	23.220	39.029	0.0001	0.172	0.248	5.310	3.291	41	21
N = 1	0.593	6.841	23.209	38.826	0.010	0.010	0.243	9.531	3.173	44	37
N = 2	0.732	6.818	22.110	39.946	0.010	0.010	0.183	13.614	3.010	24	18
N = 4	0.807	6.737	21.349	40.468	0.010	0.010	0.122	17.936	2.819	25	18
N = 6	0.794	6.859	21.212	40.537	0.010	0.010	0.129	17.462	2.802	22	15
N = 8	0.784	6.973	21.149	40.584	0.010	0.010	0.145	16.401	2.815	21	14
N = 10	0.778	7.048	21.112	40.585	0.010	0.010	0.150	16.036	2.819	24	17
Orthotropic											
Homogeneous	0.556	7.940	33.366	14.224	2.804	0.0001	0.588	8.216	6.804	31	20
N = 1	0.766	6.857	31.640	15.210	2.069	0.010	0.352	15.243	5.880	29	19
N = 2	1.040	6.557	29.375	15.979	1.742	0.010	0.118	23.296	4.565	39	24
N = 4	0.979	7.364	28.882	15.813	2.058	0.010	0.107	24.039	3.952	28	16
N = 6	0.961	7.495	28.762	15.783	2.088	0.010	0.114	23.549	3.899	21	13
N = 8	0.962	7.510	28.649	15.806	2.044	0.010	0.122	23.027	3.899	20	11
N = 10	0.959	7.542	28.565	15.813	2.017	0.010	0.123	22.750	3.981	25	12

Table 2.2: Material parameters fitted to the orthotropic and transversely isotropic datasets for the Homogeneous and $N \times N \times N$ finite element models. I refers to the value of the objective functional. The number of functional evaluations (Ev.) and functional gradient evaluations (Grad Ev.) are given in the two rightmost columns.

Table 2.3: Results of fitting material parameters to the transversely isotropic and orthotropic data sets using the multi-start method. The rows labeled 'Best Multistart' correspond to the optimizations with the lowest misfit value I. The rows labeled '$N = 8$' are copied from Table 2.2 for reference.

	a (kPa)	b	a_f (kPa)	b_f	a_s (kPa)	b_s	a_{fs} (kPa)	b_{fs}	I (mN)
Transversely Isotropic									
N = 8	*0.784*	*6.973*	*21.149*	*40.584*	*0.010*	*0.010*	*0.145*	*16.401*	*2.815*
Best Multistart	0.795	6.855	21.207	40.545	0.010	0.010	0.130	17.446	2.802
Orthotropic									
N = 8	*0.962*	*7.510*	*28.649*	*15.806*	*2.044*	*0.010*	*0.122*	*23.027*	*3.899*
Best Multistart	0.964	7.510	28.654	15.791	2.051	0.010	0.118	23.230	3.959

studies using the orthotropic dataset and finite element model ($N = 8$). The results indicate that our parameter set fits these data better than the previously computed ones.

We also note that our finite element parameter set with finite element model has a better fit value than the homogeneous parameter set with the homogeneous model. Indeed we expect the finite element fit to be at least as good as the homogeneous fit, as the finite element model allows for greater flexibility in the the deformation field, above and beyond that of the homogeneous model.

2.3.4 Computational efficiency of the adjoint-based functional gradient

Adjoint solver efficiency may be measured by comparing the runtime of the adjoint and forward solves. Here, we examine the overall gradient efficiency in a similar manner. We consider the evaluation of the gradient of the objective functional (2.15), though in a reduced case with only a single shear mode included in the sum and a reduced forward solve consisting of a single nonlinear solver iteration. In this case, the forward and adjoint models each consist of a single linear solve in addition to a number of residual evaluations. For larger linear

Table 2.4: Holzapfel-Ogden law parameter estimates from this and previous studies. I_{fem} indicates the value of the fit function (2.15) with model stresses from a finite element model ($N = 8$), and I_{hom} the value of the same fit function but with model stresses computed with a homogeneous deformation model. The material parameters of the last two rows originate from homogeneous and finite element model fits respectively in Table 2.2. Note that objective functional (I-) values for parameter sets from other studies are obtained using the orthotropic data used in this study (experimental data), and not the data used in the studies the parameter sets originate from (digitized data).

Source	a (kPa)	b	a_f (kPa)	b_f	a_s (kPa)	b_s	a_{fs} (kPa)	b_{fs}	I_{hom} (mN)	I_{fem} (mN)
[1]	0.059	8.023	18.472	16.026	2.481	11.120	0.216	11.436	36.143	36.825
[2]	0.496	7.209	15.193	20.417	3.283	11.176	0.662	9.466	28.583	29.480
[3]	0.2362	0.810	20.037	14.154	3.7245	5.1645	0.4108	11.300	33.271	34.195
[4]	0.556	7.940	33.366	14.224	2.804	0.0001	0.587	8.216	**6.804**	9.653
[5]	0.962	7.510	28.649	15.806	2.044	0.010	0.122	23.027	41.622	**3.899**

[1] Holzapfel and Ogden 2009 [2] Goektepe et al 2011 [3] Wang et al 2013 [4] current (hom) [5] current (fem).

system sizes, the runtime of a linear solve is expected to dominate the runtime of assembly, and thus these forward and adjoint models are of roughly the same computational expense.

For this reduced case, we evaluated the adjoint-based gradient for a range of linear system sizes. For each system size, we calculated the gradient runtime ratio; that is, the runtime used by the evaluation of the gradient divided by the runtime of the forward solve. The resulting ratios are plotted in Figure 2.4. The curve indicates that the gradient run-time ratio gets close to the theoretically optimal value of 1 as we increase the system size.

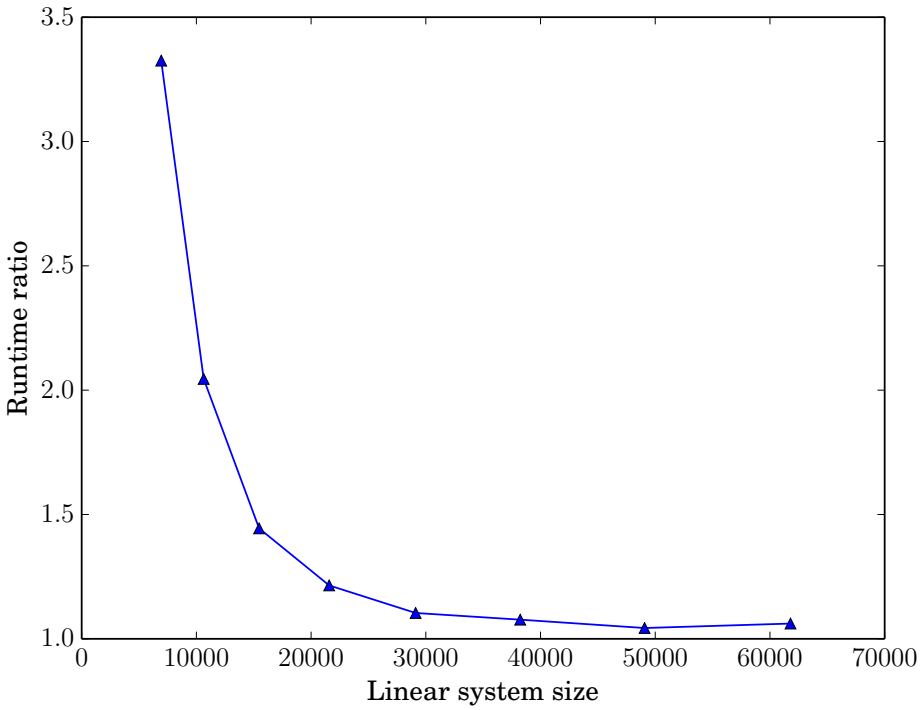

Figure 2.4: Gradient efficiency: ratio of gradient evaluation runtime over single Newton iteration runtime for increasing linear system sizes.

2.4 Discussion

2.4.1 Choice of shearing experiment datasets

Of the six shearing experiment datasets, cf. Figure 2.1, we have used two for parameter estimation. One of the reasons for this choice is an incompatibility of most of the datasets with assumptions made in the design of the strain energy functional (2.2). In particular, the strain energy (2.2) dictates an ordering of the shear mode stiffnesses in the case of a homogeneous shear displacement. We can see this by adapting the analysis that leads to equations (5.23) – (5.28) of [15]. In this analysis a parameter γ is introduced to represent the amount of simple shear displacement present in a homogeneous deformation. For example for the FS mode

$$\mathbf{F} = \begin{bmatrix} 1 & \gamma & 0 \\ 0 & 1 & 0 \\ 0 & 0 & 1 \end{bmatrix}. \tag{2.22}$$

Using this deformation gradient, and the respective deformation gradients of the other modes, the shear component of the Cauchy stress σ in the shearing direction can be calculated for each mode. If we consider the same invariants as in (2.2), that is $I_1, I_{4f}, I_{4s}, I_{8fs}$, and use the notation $\psi_i = \frac{\partial \psi}{\partial I_i}$, we arrive at the following equations for shear stress as a function of shear displacement

$$\begin{aligned} \text{(FS):} \quad & \sigma_{FS} = 2(\psi_1 + \psi_{4f})\gamma + \psi_{8fs}, \\ \text{(FN):} \quad & \sigma_{FN} = 2(\psi_1 + \psi_{4f})\gamma, \\ \text{(SF):} \quad & \sigma_{SF} = 2(\psi_1 + \psi_{4s})\gamma + \psi_{8fs}, \\ \text{(SN):} \quad & \sigma_{SN} = 2(\psi_1 + \psi_{4s})\gamma, \\ \text{(NF):} \quad & \sigma_{NF} = 2\psi_1\gamma, \\ \text{(NS):} \quad & \sigma_{NS} = 2\psi_1\gamma. \end{aligned} \tag{2.23}$$

For further details regarding the derivation of these equations we refer the reader to [15]. The simple shear stresses (2.23) reveal two assumptions built into the

design of (2.2), namely for homogeneous simple shear deformations

$$\begin{aligned} \sigma_{FS} \geq \sigma_{FN} \geq \sigma_{NF}, \\ \sigma_{SF} \geq \sigma_{SN} \geq \sigma_{NF}. \end{aligned} \tag{2.24}$$

Out of the six datasets, only one is consistent with these orderings, namely the 6th one, which was used here under the label transversely isotropic. In this dataset the stress-strain relationship is typical of a transversely isotropic material with a stiffer fiber direction. In several other cardiac mechanics simulation studies [10, 11, 18], the Holzapfel and Ogden energy functional (2.2) has been simplified to model transversely isotropic behavior by removing the terms involving the invariants I_{4s}, I_{8fs}. For such a simplified model one could use the parameter estimates for a, b, a_f, b_f that we obtained from the Transversely Isotropic dataset.

However, the Holzapfel and Ogden model was originally proposed to model orthotropic behavior. This motivates also targeting a dataset displaying fully orthotropic properties. In particular, dataset 2 in Figure 2.1 is such and compares well with Figure 6 of [8] and Figure 2 of [15]. By switching the SF and SN curves of Dataset 2 we were able to reinterpret this data in a way that is consistent with the interpretation in [15], and the shear stiffness orderings (2.24).

2.4.2 Discussion of optimal material parameter values

We have obtained two sets of material parameters: one corresponding to an orthotropic case and one corresponding to a transversely isotropic case. We observe that for both sets of material parameters, the b_s parameter essentially vanishes. For the Transversely Isotropic case, both a_s and b_s essentially vanish, which is in excellent agreement with the transversely isotropic stress-strain pattern. Furthermore we note that the magnitude of both a_s and b_s parameters in the best fitting parameter sets presented in Table 2.3 are very small. In light of the shear stress calculations (2.23) we can see that the a_s and b_s parameters are related to the degree of extra stiffness in the sheet direction over the sheet normal direction. Indeed when we examine the shear data, Figure 2.3, we can see that the $SN - SF$ curves are only slightly stiffer than the $NF - NS$ curves, which explains why the optimal values of a_s and b_s are so small.

Comparing the orthotropic material parameter values to the previously published values in Table 2.4, we observe that the fit of our material parameters is better. This was expected since we used a finite element model which did not include a homogeneous shearing angle assumption and hence was able to more realistically model the motion of the cubes in the shearing experiment. We note that our material parameters differ from those previously published, and also that there is a significant variability in the parameter values previously reported. Some of this variability is most likely due to the differences in the selection of points during the digitization of [Figure 2 of [15]], which was done in the studies whose material parameter sets we compare in Table 2.4. By using original data from the shearing experiment, we were able to remove the uncertainty due to digitization in our parameter estimates. Finally we note that even after the SF-SN curves are swapped in Dataset 2 of Figure 2.1, there are still minor differences when compared to [Figure 7 of [15]] and [Figure 3 of [12]] and [Figure 4 of [27]]. This also explains why our parameter sets differ from those calculated in the previous studies.

2.4.3 Computing functional gradients in cardiac mechanics

Figure 2.4 demonstrates that the computational cost of the adjoint gradient computation is comparable to that of a single iteration of the nonlinear solution algorithm of (2.5) for larger system sizes. For smaller system sizes, the cost of symbolic computation and the cost of residual and Jacobian assembly contribute significantly yielding higher ratios – as expected. Wang et al.'s 2013 simulations of a human left ventricle in diastole use system sizes of approximately $100\,000$ degrees of freedom [27]. Given the trend in Figure 2.4, we can expect that the adjoint method and solver implemented in this work will continue to be efficient at this scale and beyond.

Comparatively, assuming the use of Newton's method for the solution of nonlinear systems, the evaluation of a finite difference gradient requires a linear system assembly and solve for each Newton iteration, and one nonlinear solve is required per component of the gradient. Counting the 8 parameters in the Holzapfel-Ogden model (2.2), and assuming a typical solution of the Euler-Lagrange equation (2.5) takes 6 Newton iterations, we can expect the computational cost of finite

difference gradient evaluation to be circa 48 times greater than that of the adjoint method.

In the optimization results of Table 2.2, we observed iteration counts of up to 44 for the optimization of 8 parameters using our gradient-based method. This compares favorably with the circa 7000 iterations needed to estimate 9 parameters using a global method in [Figure 5 of [29]].

2.4.4 Implications for organ-scale image-based parameter estimation with spatially resolved material parameters

Although we have tested our adjoint-based multi-start optimization method on the 2002 shear data of Dokos et al [8], we believe our methods will provide the biggest advantage in the case of optimizing cardiac model parameters in high spatial resolution at the organ scale to MRI or echocardiographic image data. In this case the high spatial resolution would allow for detailed modelling of regional differences in tissue stiffness, which is for example present in patients with post-infarct fibrosis.

In such an application a model parameter could be represented as a finite element function similarly to the displacement or hydrostatic pressure fields ($\mathbf{u}$, p). Doing this would increase the number of components of the gradient $\frac{D\hat{I}}{D\mathbf{m}}$ by the number of degrees of freedom needed to spatially represent the parameter of interest. Using a finite difference or reduced order Kalman filter approach in this case would require an additional evaluation of the Euler-Lagrange equation (2.5) for each degree of freedom introduced, whereas the adjoint gradient formula (2.13) only needs to be calculated once regardless of the number of additional degrees of freedom. In the current study the adjoint gradient is estimated to be

$$\text{(number of model parameters)} \times 6 = 48$$

times faster than finite differencing. In the case of a spatially varying model parameter the speedup is potentially a lot more significant.

When fitting material parameters to the Dokos experiment data, we were able to generate good initial guesses for the local optimization by progressively refining the mesh and using the optimal results from the previous coarser refinement level as an initial guess in the successive finer level. It would be more challenging to

apply this technique using image based ventricular geometries, due to the problem of accurately representing the geometry with few elements. As an alternative we propose the multi-start approach, which we have shown here to be accurate and viable using the Dokos experiment data.

One issue that would arise in using the multi-start approach with image based geometries would be the choice of the number of multi-start points; using less points is more computationally efficient, while using more is potentially more robust. Possible solutions are the use of optimal stopping criteria [4] or more sophisticated local-global searches [13, 26].

2.5 Conclusions

In this work, we have presented a new application of efficient gradient-based optimization methods in the context of estimating cardiac hyperelastic material parameters from experimental data. In particular, we have demonstrated how an adjoint solution can greatly speed up the evaluation of functional gradients. These methods have produced two new sets of material parameter values that yield simulated stress-strain curves that fit closely to orthotropic and transversely isotropic shear data. For future parameter estimation studies using image based geometries and a local search algorithm, multi-start or a similar method should be used in order to avoid suboptimal minima.

Acknowledgements

The authors would like to thank Socrates Dokos, Holger Schmid and Ian LeGrice, for making the experimental data available. Our work is supported by The Research Council of Norway through a Centres of Excellence grant to the Center for Biomedical Computing at Simula Research Laboratory, project number 179578, and also through the Center for Cardiological Innovation at Oslo University Hospital project number 203489. Alnæs has been supported by the Research Council of Norway through grant number 209951. Computations were performed on the Abel supercomputing cluster at the University of Oslo via NOTUR project NN9316k.

Bibliography

[1] Martin S Alnæs, Anders Logg, Kristian B Ølgaard, Marie E Rognes, and Garth N Wells. Unified form language: A domain-specific language for weak formulations of partial differential equations. *ACM Transactions on Mathematical Software (TOMS)*, 40(2):9, 2014.

[2] Kevin F Augenstein, Brett R Cowan, Ian J LeGrice, Poul MF Nielsen, and Alistair A Young. Method and apparatus for soft tissue material parameter estimation using tissue tagged magnetic resonance imaging. *Journal of biomechanical engineering*, 127(1):148–157, 2005.

[3] S Balay, J Brown, K Buschelman, WD Gropp, D Kaushik, MG Knepley, L Curfman McInnes, BF Smith, and H Zhang. Petscc web page, 2015.

[4] Cornelis Gustaaf Eduard Boender and AHG Rinnooy Kan. Bayesian stopping rules for multistart global optimization methods. *Mathematical Programming*, 37(1):59–80, 1987.

[5] Radomir Chabiniok, Philippe Moireau, P-F Lesault, Alain Rahmouni, J-F Deux, and Dominique Chapelle. Estimation of tissue contractility from cardiac cine-MRI using a biomechanical heart model. *Biomechanics and modeling in mechanobiology*, 11(5):609–630, 2012.

[6] Kevin D Costa, Jeffrey W Holmes, and Andrew D McCulloch. Modelling cardiac mechanical properties in three dimensions. *Philosophical transactions of the Royal Society of London. Series A: Mathematical, physical and engineering sciences*, 359(1783):1233–1250, 2001.

[7] H Delingette, F Billet, K C L Wong, M Sermesant, K Rhode, M Ginks, C A Rinaldi, R Razavi, and N Ayache. Personalization of Cardiac Motion and Contractility From Images Using Variational Data Assimilation. *Biomedical Engineering, IEEE Transactions on*, 59(1):20–24, January 2012.

[8] Socrates Dokos, Bruce H Smaill, Alistair A Young, and Ian J LeGrice. Shear properties of passive ventricular myocardium. *American Journal of Physiology-Heart and Circulatory Physiology*, 283(6):H2650–H2659, 2002.

[9] Patrick E Farrell, David A Ham, Simon W Funke, and Marie E Rognes. Automated derivation of the adjoint of high-level transient finite element programs. *SIAM Journal on Scientific Computing*, 35(4):C369–C393, 2013.

[10] Henrik N Finsberg, Gabriel Balaban, Joakim Sundnes, Hans Henrik Odland, Marie Rognes, and Samuel T Wall. Mechanical imaging of dynamic patient stress patterns, June 2015.

[11] Sjur Gjerald, Johan Hake, Simone Pezzuto, Joakim Sundnes, and Samuel T Wall. Patient–specific parameter estimation for a transversely isotropic active strain model of left ventricular mechanics. In *Statistical Atlases and Computational Models of the Heart-Imaging and Modelling Challenges*, pages 93–104. Springer, 2015.

[12] S Göktepe, SNS Acharya, J Wong, and E Kuhl. Computational modeling of passive myocardium. *International Journal for Numerical Methods in Biomedical Engineering*, 27(1):1–12, 2011.

[13] David E Goldberg and Siegfried Voessner. Optimizing global-local search hybrids. *Urbana*, 51:61801, 1999.

[14] Max D Gunzburger. *Perspectives in flow control and optimization*, volume 5. Siam, 2003.

[15] Gerhard Holzapfel and Ray W Ogden. Constitutive modelling of passive myocardium: a structurally based framework for material characterization. *Philosophical transactions. Series A, Mathematical, physical, and engineering sciences*, 367(1902):3445–75, sep 2009.

[16] P Hood and C Taylor. Navier-stokes equations using mixed interpolation. *Finite element methods in flow problems*, pages 121–132, 1974.

[17] Eric Jones, Travis Oliphant, Pearu Peterson, et al. SciPy: Open source scientific tools for Python, 2001–. [Online; accessed 2014-12-09].

[18] Adarsh Krishnamurthy, Christopher T Villongco, Joyce Chuang, Lawrence R Frank, Vishal Nigam, Ernest Belezzuoli, Paul Stark, David E Krummen, Sanjiv Narayan, Jeffrey H Omens, et al. Patient-specific models of cardiac biomechanics. *Journal of computational physics*, 244:4–21, 2013.

[19] Anders Logg, Kent-Andre Mardal, Garth N. Wells, et al. *Automated Solution of Differential Equations By the Finite Element Method*. Springer, 2011.

[20] S Marchesseau, H Delingette, M Sermesant, M Sorine, K Rhode, S G Duckett, C a Rinaldi, R Razavi, and N Ayache. Preliminary specificity study of the Bestel-Clément-Sorine electromechanical model of the heart using parameter calibration from medical images. *Journal of the mechanical behavior of biomedical materials*, 20:259–71, May 2013.

[21] Kambiz Salari and Patrick Knupp. Code verification by the method of manufactured solutions. Technical report, Sandia National Labs., Albuquerque, NM (US); Sandia National Labs., Livermore, CA (US), 2000.

[22] H Schmid, MP Nash, AA Young, O Röhrle, and PJ Hunter. A computationally efficient optimization kernel for material parameter estimation procedures. *Journal of biomechanical engineering*, 129(2):279–283, 2007.

[23] H Schmid, P O'Callaghan, MP Nash, W Lin, IJ LeGrice, BH Smaill, AA Young, and PJ Hunter. Myocardial material parameter estimation-a non–homogeneous finite element study from simple shear tests. *Biomechanics and modeling in mechanobiology*, 7(3):161–173, 2008.

[24] H Schmid, YK Wang, J Ashton, AE Ehret, SBS Krittian, MP Nash, and PJ Hunter. Myocardial material parameter estimation-a comparison of invariant based orthotropic constitutive equations. *Computer methods in biomechanics and biomedical engineering*, 12(3):283–295, 2009.

[25] Hari Sundar, Christos Davatzikos, and George Biros. Biomechanically-constrained 4d estimation of myocardial motion. In *Medical Image Computing and Computer-Assisted Intervention–MICCAI 2009*, pages 257–265. Springer, 2009.

[26] Frank T-C Tsai, Ne-Zheng Sun, and William W-G Yeh. Global-local optimization for parameter structure identification in three-dimensional groundwater modeling. *Water resources research*, 39(2), 2003.

[27] HM Wang, H Gao, XY Luo, C Berry, BE Griffith, RW Ogden, and TJ Wang. Structure-based finite strain modelling of the human left ventricle in diastole. *International journal for numerical methods in biomedical engineering*, 29(1):83–103, 2013.

[28] Vicky Y Wang, H I Lam, Daniel B Ennis, Brett R Cowan, Alistair a Young, and Martyn P Nash. Modelling passive diastolic mechanics with quantitative MRI of cardiac structure and function. *Medical image analysis*, 13(5):773–84, October 2009.

[29] Ken CL Wong, Maxime Sermesant, Kawal Rhode, Matthew Ginks, C Aldo Rinaldi, Reza Razavi, Hervé Delingette, and Nicholas Ayache. Velocity-based cardiac contractility personalization from images using derivative-free optimization. *Journal of the mechanical behavior of biomedical materials*, 43:35–52, 2015.

[30] Jiahe Xi, Pablo Lamata, Jack Lee, Philippe Moireau, Dominique Chapelle, and Nic Smith. Myocardial transversely isotropic material parameter estimation from in-silico measurements based on a reduced-order unscented kalman filter. *Journal of the mechanical behavior of biomedical materials*, 4(7):1090–1102, 2011.

3 Paper II: High Resolution Data Assimilation of Cardiac Mechanics

High Resolution Data Assimilation of Cardiac Mechanics

Gabriel Balaban[1,2,5], Henrik Finsberg[1,2,5], Hans Henrik Odland[4,5], Marie E. Rognes[4,5], Stian Ross[4,5], Joakim Sundnes[1,2,5], Samuel Wall[1,6,5]

1. Simula Research Laboratory, P.O. Box 134 1325 Lysaker, Norway
2. Department of Informatics, University of Oslo, P.O. Box 1080 Blindern 0316 Oslo, Norway
3. Department of Mathematics, University of Oslo, P.O. Box 1053 Blindern 0316 Oslo, Norway
4. Faculty of Medicine, University of Oslo, P.O. Box 1078 Blindern, 0316 Oslo, Norway
5. Center for Cardiological Innovation, Songsvannsveien 9, 0372 Oslo, Norway
6. Department of Mathematical Science and Technology, Norwegian University of Life Sciences, Universitetstunet 3 1430 Ås, Norway

Abstract: Computational models of cardiac mechanics, personalized to a patient, offer access to mechanical information and tissue biomarkers above and beyond direct medical imaging. Additionally, such models can be used to optimize and plan therapies in-silico, thereby reducing risks and improving patient outcome. Model personalization has traditionally been achieved by data assimilation, which is the tuning or optimization of model parameters to match patient observations. Current data assimilation procedures for cardiac mechanics are limited in their ability to efficiently handle high dimensional parameters. This restricts parameter spatial resolution, and thereby the ability of a personalized model to account for heterogeneities that are often present in a diseased or injured heart. In this paper we address this limitation by proposing an adjoint-gradient based data assimilation method that can efficiently handle high-dimensional parameters. We test this procedure on a synthetic data set, and then provide a clinical example with a dyssynchronous left ventricle with highly irregular motion. Our results show that the method efficiently handles a high dimensional optimization parameter, and produces an excellent agreement for personalized models to both synthetic and clinical data.

[0]Gabriel Balaban and Henrik Finsberg contributed equally to this work.

3.1 Introduction

Computational cardiac mechanics models are potentially a powerful aid in the diagnosis and treatment of cardiac disease. By relating image based observations to fundamental physical properties, models can provide analysis and tissue biomarkers beyond what can be observed by medical imaging. Furthermore, computational models offer cost and safety advantages over in-vivo experimentation and testing, so that they can be used to plan and optimize therapies before any invasive surgeries are undertaken.

A key step in making such a clinically useful cardiac mechanics model is proper data assimilation from patient observations into a fit model. This involves the optimization, or tuning, of individual model parameters in order to make the model match the observations of the patient's heart. A successful data assimilation calibrates the model so that it can be used to make predictions relevant to the patient's condition.

Over the last decade several data assimilation methods have been proposed for the creation of patient-specific cardiac mechanics models from clinical data. The earliest studies employed gradient based optimization in order to minimize the discrepancy between model-derived data and clinical observations. The gradients necessary for these optimizations were calculated using direct differentiation [36] or finite differencing [2, 15, 39]. More recent efforts include the use of global optimization methods: in particular genetic algorithms [31, 37], a Monte Carlo method [33], subplex algorithm [40], and parameter sweeps [1, 19]. Finally, reduced order unscented Kalman filtering has also been successfully applied as a data assimilation tool for patient-specific model creation [10, 30, 41].

However, the computational expense of the techniques mentioned above scale badly with the number of model parameters. In the case of the Kalman filtering strategies, at least one extra evaluation of the model is required per additional model parameter to be optimized. The calculation of model-data mismatch gradients by finite differencing or direct differentiation suffers from the same limitation. Global methods on the other hand are affected by the curse of dimensionality; that is, a rapid expansion of the space of parameters that must be searched as the number of dimensions increases. For high dimensional problems the run-time needed to carry out a global search can be computationally prohibitive.

In contrast to the previously mentioned techniques the calculation of a functional gradient by the adjoint formula is nearly independant of the number of optimization parameters. The requirements of this formula are a forward and backward adjoint solve of the mathematical model. The forward solve is typically needed to evaluate the functional, so that the evaluation of the gradient at the same point requires only an additional backward solve of the adjoint system. This backward solve is linear, and therefore slightly cheaper than the forward solve. Adjoint-based data assimilation techniques have previously been employed for cardiac mechanics using linear elastic models and clinical data [11, 38], and also a nonlinear model with experimental data [4].

Our example of improved data assimilation is demonstrated by optimizing a mechanical contraction parameter in high spatial resolution to patient data. This leads to a high dimensional optimization problem that can be efficiently solved using an adjoint gradient based technique, which was described in detail in our previous work [4]. We demonstrate our method on the pathological case of a dyssynchronous left ventricle, which has a complex and irregular motion, as well as on a synthetic case consisting of data generated by our mechanical model.

This study is to the best of our knowledge the first to use adjoint-based data assimilation for nonlinear cardiac mechanics with clinical data, and the first to consider the resolution of a parameter at the same scale as the discretization of the cardiac geometry.

The rest of this paper is organized as follows: In Section 3.2 we present a mathematical model that accounts for the three main drivers of ventricular mechanics; blood pressure, tissue elasticity and muscle contraction. Furthermore, we describe two datasets: one clinical case exhibiting dyssynchrony, and one synthetic. We also describe our data assimilation procedure for fitting the model. The numerical results are presented in Section 3.3, and discussed in Section 3.4. Finally, we provide some concluding remarks in Section 3.5.

3.2 Materials and Methods

3.2.1 Wall motion modelling

In order to estimate the position of the myocardial walls through the cardiac cycle we adopt a continuum mechanics description of cardiac wall motion. In this description we consider a fixed left ventricular reference geometry Ω, with endocardial boundary $\partial\Omega_{\text{endo}}$, and basal boundary $\partial\Omega_{\text{base}}$.

Our fundamental quantity of interest is the vector valued displacement map $\mathbf{u}(\mathbf{X})$, where $\mathbf{X} \in \Omega$. At any given point in time in the cardiac cycle, $\mathbf{u}(\mathbf{X})$ relates the current geometry ω to the reference geometry by

$$\mathbf{X} + \mathbf{u}(\mathbf{X}) = \mathbf{x}, \quad \mathbf{x} \in \omega, \quad \mathbf{X} \in \Omega. \tag{3.1}$$

Assuming that the cardiac walls are in equilibrium, it is possible to determine the value of $\mathbf{u}$ from the principle of virtual work

$$\delta W(\mathbf{u}) = 0, \tag{3.2}$$

which states that the virtual work, $\delta W(\mathbf{u})$, of all forces applied to a mechanical system vanishes in equilibrium. For our ventricular wall motion model, the virtual work $\delta W(\mathbf{u})$, is given by

$$\begin{aligned}\delta W(\mathbf{u}) = &\int_\Omega \mathbf{P} : \operatorname{Grad} \delta\mathbf{u}\, dV + \int_\Omega (J-1)\delta p + pJ\mathbf{F}^{-T} : \operatorname{Grad} \delta\mathbf{u}\, dV \\ &+ p_{\text{blood}} \int_{\partial\Omega_{\text{endo}}} J\mathbf{F}^{-T}\mathbf{N}\cdot \delta\mathbf{u}\, dS + \int_{\partial\Omega_{\text{base}}} k\mathbf{u}\cdot \delta\mathbf{u}\, dS.\end{aligned} \tag{3.3}$$

Here we have introduced the hydrostatic pressure p in order to enforce the incompressibility constraint $J = 1$, with $J = \det \mathbf{F} = \det(\operatorname{Grad} \mathbf{u} + \mathbf{I})$, and $\mathbf{I}$ being the second order identity tensor. Furthermore, $\mathbf{N}$ denotes the unit outward normal vector, k the constant of a spring that we introduce at the basal boundary, and p_{blood} the intra-ventricular blood pressure. The virtual variables $\delta\mathbf{u}$ and δp are test functions whose values in Equation (3.2) are arbitrary in the case of a mechanical equilibrium.

In order to anchor the computational geometry, we fix $\mathbf{u}$ in the longitudinal

direction at the base by using a Dirichlet boundary condition. At the epicardial boundary normal forces are set to 0, and so there is no term for this boundary in (3.3).

The internal stresses of our model are given by $\mathbf{P}$, the first Piola-Kirchhoff tensor, which can be calculated as a derivative of a strain energy functional in the case of a hyperelastic material. In our model we employ a reduced version [1, 18, 19, 26] of the Holzapfel-Ogden strain energy law [21],

$$\psi(\mathbf{C}) = \frac{a}{2b}\left(e^{b(I_1(\mathbf{C})-3)} - 1\right) + \frac{a_f}{2b_f}\left(e^{b_f(I_{4f}(\mathbf{C})-1)_+^2} - 1\right), \tag{3.4}$$

which gives the amount of strain energy, ψ, stored per unit volume myocardium undergoing the strain $\mathbf{C} = \mathbf{F}^T\mathbf{F}$. The notation $(\cdot)_+$ refers here to $\max\{\cdot, 0\}$. Furthermore the mechanical invariants I_1 and I_{4f} are defined as

$$I_1(\mathbf{C}) = \text{tr } \mathbf{C}, \qquad I_{4f} = \mathbf{e_f} \cdot \mathbf{C}\mathbf{e_f}, \tag{3.5}$$

with $\mathbf{e_f}$ indicating the local myocardial fiber direction. The material parameters a, a_f, b, b_f are scalar quantities which influence the shape of the stress-strain relationship, and can be adapted to personalize the elastic properties of a myocardial tissue model to a specific patient.

The Lagrange multiplier formulation of incompressibility that we employ enforces its constraint only weakly. This can cause convergence issues in the numerical solution of the work balance equation (3.2). We therefore eliminate volumetric strains from the energy function (3.4) by a simple modification

$$\tilde{\psi}(\mathbf{C}) = \psi(J^{-\frac{2}{3}}\mathbf{C}), \tag{3.6}$$

which has been shown to improve the robustness of Newton-Raphson methods applied to incompressible hyperelastic problems [Figure 3C of [27]].

In order to account for muscle contraction we apply the active strain framework [32]. In this framework the amount of muscle fiber shortening is specified by a field γ via a split of the deformation gradient

$$\mathbf{F} = \mathbf{F}_e\mathbf{F}_a(\gamma), \tag{3.7}$$

where $\mathbf{F}_e$ is the elastic part and $\mathbf{F}_a(\gamma)$ the active part of the deformation gradient. For the value of $\mathbf{F}_a(\gamma)$ we adopt a simple relation [12, 18] which satisfies the incompressibility constraint by design and directly relates the amount of active fiber shortening to the value of γ

$$\mathbf{F}_a = (1-\gamma)\mathbf{e}_f \otimes \mathbf{e}_f + \frac{1}{\sqrt{1-\gamma}}(\mathbf{I} - \mathbf{e}_f \otimes \mathbf{e}_f). \tag{3.8}$$

In the case $\gamma = 0$ there is no active shortening at all, and the amount of shortening increases with increased γ up to the theoretical limit of $\gamma = 1$.

The active contraction is accounted for in terms of virtual work by modifying the first Piola-Kirchhoff stress tensor, so that the strain energy only depends on the elastic part of the deformation

$$\mathbf{P} = \frac{\partial \tilde{\psi}}{\partial \mathbf{F}} = \frac{\partial \tilde{\psi}(\mathbf{C}_e)}{\partial \mathbf{F}} \tag{3.9}$$

with $\mathbf{C}_e = \mathbf{F}_e^T \mathbf{F}_e$.

Given an amount of fiber shortening γ, the value of the elastic parameters a, b, a_f, b_f, the intraventricular blood pressure p_{blood} and the spring constant k, the myocardial wall displacement $\mathbf{u}$ and hydrostatic pressure p can be obtained by solving the principle of virtual work (3.2).

3.2.2 Clinical measurements

Clinical data were obtained with the permission of staff of Oslo University Hospital in the context of the Impact study [23]. Specifically, we consider the case of an 82 year old man in NYHA functional class III systolic heart failure with coronary artery disease, and left bundle branch block. A left bundle branch block normally causes both electrical and mechanical dyssynchrony. This case had a QRS width of 140 ms and an ejection fraction of 30 %.

Prior to cardiac resynchronization therapy implant, the patient had echocardiographic and left ventricular (LV) pressure measurements taken, which are the basis for the clinical data used in this study. Pressure recordings were carried out using a standard over the wire technique; that is, a pressure catheter (Millar micro catheter) was placed in the LV through a multipurpose catheter via the right

femoral artery. A stable position inside the LV cavity was established by withdrawing the multipurpose catheter into the ascending aorta. Pressure data were obtained automatically within the frequency range of 0 – 1000Hz and digitized (Powerlab system, AD Instruments) before offline analyses were performed with a low pass filter of 200Hz.

Images of the patient's left ventricle (LV) were captured with 4D echocardiography using a GE Vingmed E9 machine. Speckle tracking motion analysis was carried out with GE's software package EchoPac. Data from 6 beats were combined in EchoPac in order to obtain a single sequence of images for a single heartbeat. Analysis of these images resulted in LV cavity volume measurements as well as regional strain curves defined for a 17 segment delineation of the LV according to the AHA representation [9]. The strain curves were measured in the local left ventricular longitudinal, radial and circumferential directions. Both strains and volumes were measured 34 times throughout the cardiac cycle. Using ECG data and valvular events, a representative pressure trace from the catheter was synchronized to the strain and volume data. A pressure-volume loop based on this synchronization is displayed in Figure 3.2.

Finally a linear correction of the strain curves was performed based on the drift of the curves; with the drift being the value of the strain obtained at the end of the cardiac cycle. Theoretically the drift is zero for stable conditions during which the heartbeat is cyclical, and the linear correction enforces this cyclical property.

3.2.3 Computational geometry generation

The computational mechanics framework used for our wall motion model, described in Section 3.2.1, requires a reference stress-free geometry from which to define displacements. Such a geometry typically does not exist in-vivo due to the presence of blood pressure on the endocardial walls. Algorithms exist for calculating stress free geometries given a loaded state [8, 16]. However for the sake of simplicity we derive our reference geometry from an echocardiographic image of the LV at the beginning of atrial systole, as the pressure is near minimal at this point, and the ventricular myocardium can be assumed to be relaxed.

From the image at the beginning of atrial systole, triangulated data points for left ventricular endocardial and epicardial surfaces, along with a 17 segment de-

lineation, were extracted using the EchoPac software package. The segment delineation was given on a so called strain mesh, which is a 2-D surface constructed by EchoPac and located approximately in the midwall of the LV.

We constructed a basal plane via least squares fitting, using the basal points of the strain mesh as target data. The position of the basal plane was then adjusted so that the cavity volume of the resulting mesh agreed with the measured volume to a tolerance of 1 ml. Points on the epicardial and endocardial surfaces that lay above the basal plane were removed.

We employed Gmsh [17] to create three linear tetrahedral volumetric meshes between the endocardial and epicardial surfaces, with 4407, 8401 and 16343 elements. The mesh with 16343 elements is shown in Figure 3.1b. Myocardial fiber orientations were assigned using a rule based method, with a fiber helix angle of 40 degrees on the endocardium rotated clockwise throughout the ventricular wall to 50 degrees on the epicardium [6]. A streamline representation of the local myocardial fibers is displayed in Figure 3.1c.

Finally, the AHA-segments from the strain meshes were transferred onto the volumetric meshes. This was accomplished by computing prolate spherical coordinates for the barycenter of each tetrahedron, and then assigning an AHA-zone to the tetrahedron based on the corresponding prolate spherical coordinate in the strain mesh. The volumetric mesh with 16343 elements complete with AHA-segments is shown in Figure 3.1d.

3.2.4 Synthetic test case

A synthetic dataset was constructed by solving the virtual work equation (3.2) for a given set of elastic parameters (a, a_f, b, b_f), contraction γ, cavity pressures p_{blood} and spring constant k. The elastic parameters were chosen from a fit of the reduced Holzapfel-Ogden law (3.4) to a set of patient-specific diastolic displacements [Table 5 of [1]].

The contraction γ was chosen to be a wave traveling from apex to base with a Gaussian shape along the basal-apical axis. A set of eight synthetic measurements were generated. The pressure values of the first three measurements are the pressure increases in the atrial systolic points of the patient pressure-volume loop, Figure 3.2, and the rest are a linear extrapolation to 0 kPa. The exact pressures

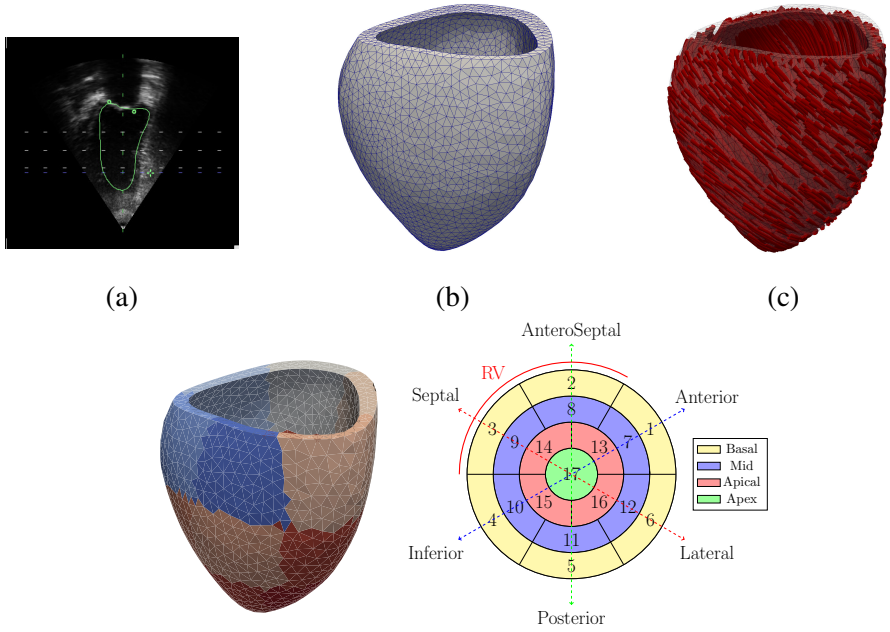

Figure 3.1: Computational geometry generation. Endo and epi-cardial surfaces are marked on 3-D ultrasound images, 3.1a shows the endocardial marking for a 2-D slice of one such image. Next a computational geometry is generated from epi and endo-cardial surfaces 3.1b, and rule based fibers are assigned 3.1c. Finally AHA segments are assigned to the geometry 3.1d, according to the standardized scheme 3.1e.

Table 3.1: Mean and standard deviation of a Gaussian noise summand estimated from patient drift values in circumferential (C), radial (R) and longitudinal (L) directions.

Mean	Covariance $\times 10^{-4}$			
	C	R	L	
0.006	1.43	0.73	0.66	C
-0.013	-	6.8	6.31	R
0.01	-	-	7.26	L

values in kPa are $\{0.93, 2.0, 4.8, 4.8, 3.6, 2.4, 1.2, 0.0\}$.

The strains and volumes generated by the wall motion model from the specified Gaussian contraction wave, together with the pressures, form a set of synthetic measurements that can be used to test our data assimilation procedure. These synthetic measurements contain fewer points than the clinical measurements, thereby allowing for faster computations.

In order to increase the relevance of the synthetic dataset we added noise to the computed synthetic strains and volumes. The strain noise was modelled as an additive Gaussian process in order to imitate the accumulation of tracking errors in EchoPac's image based strain calculations. The mean and variance of a summand in the Gaussian process were estimated by dividing the sample means and variances of the strain drift values by the number of measurement points. The resulting mean and covariance estimates are given in Table 3.1. Theoretically, error free strain curves would have almost no drift, making the drift values a good approximation of the tracking error. Similarly to our patient dataset, we performed a linear correction of our synthetic strain curves based on the synthetic drift values.

Finally our synthetic volume measurements are corrupted by Gaussian noise with mean 0 and a standard deviation of 4.3 mL. This standard deviation value was experimentally obtained in [3, Figure 3B]].

3.2.5 Parameter Estimation

Now that we have a mathematical description of cardiac motion, along with a personalized computational geometry and target data, we next turn to the problem of personalizing the motion model via the estimation of the elastic parameters a, a_f, b, b_f and fiber contraction γ.

We consider a, a_f, b, b_f to be constant in time, as these parameters characterize the myocardial stress-strain relationship, which we do not expect to change in the span of a heartbeat. On the other hand, we expect the fiber contraction to vary significantly during a heartbeat, and therefore estimate γ separately for each set of pressure, strain, and volume measurements in the cardiac cycle. Furthermore, as the contraction of the left ventricle may occur dyssynchronously, we allow for γ to vary in space as well as in time.

Active muscle shortening is typically present in the ventricles throughout systole and in early diastole until the muscles fully release their contraction. During the phase of atrial systole we do not expect muscle contraction in the ventricle, and so we set $\gamma = 0$ for this phase. This allows us to estimate a, b, a_f, b_f independently of γ during atrial systole, and then estimate γ at each point in the rest of the cardiac cycle with the material parameters fixed. In Figure 3.2 we show the pressure-volume loop of the patient under consideration, and highlight the phases where we estimate the contraction and elastic parameters.

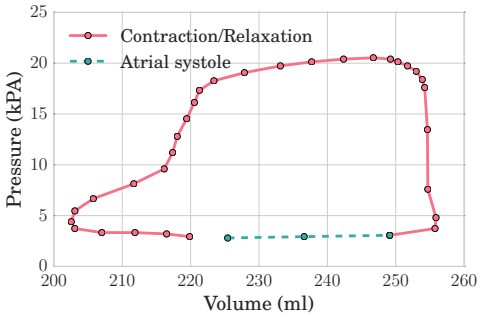

Figure 3.2: Patient pressure-volume relationship for the left ventricle. Measurements in the red solid line are used to estimate contraction, whereas measurements in the green dashed line are used to estimate elasticity.

3.2.6 Definition of data matching functionals

As described in Section 3.2.2, the data available for our personalization of the wall motion model are pressure, volume and strain measurements throughout the cardiac cycle. The pressure measurements are included in the model as a boundary condition via the virtual work (3.2), and thus our data assimilation only needs to fit the model to the volume and strain measurements. In order to do this we define a suitable set of functionals that quantify the model-data mismatch. The personalization of the wall motion model can then be achieved by optimizing the contraction and elastic parameters in order to minimize the model-data mismatch.

Let i denote the index of an observed cavity volume V^i, or strain ε^i, in the cardiac cycle. Furthermore let $j \in \{1, .., 17\}$ be the index of an AHA segment Ω_j, and $k \in \{c, r, l\}$ indicate a direction: circumferential, radial or longitudinal, respectively. Given a measurement point i, we define the model-strain mismatch

$$I^i_{\text{strain}} = \sum_{j=1}^{17} \sum_{k\in\{c,r,l\}} \left(\varepsilon^i_{k,j} - \tilde{\varepsilon}^i_{k,j}\right)^2, \tag{3.10}$$

for model strain $\tilde{\varepsilon}^i_{k,j}$ and measured strain $\varepsilon^i_{k,j}$.

The speckle tracking software we used provided regionally averaged Lagrangian strain measurements $\varepsilon^i_{k,j}$. In order to mimic these measurements in our model we define the model strain as

$$\varepsilon_{k,j} = G_j(\mathbf{e}_k^T \nabla \mathbf{u}\, \mathbf{e}_k), \tag{3.11}$$

where $\mathbf{e}_k$ denotes a unit direction field and G_j is the averaging operator

$$G_j(f) = \frac{1}{|\Omega_j|} \int_{\Omega_j} f dx, \tag{3.12}$$

with $|\Omega_j|$ indicating the volume of segment j. Furthermore we also define the model-volume mismatch

$$I^i_{\text{vol}} = \left(\frac{V^i - \tilde{V}^i}{V^i}\right)^2, \quad \tilde{V}^i = -\frac{1}{3}\int_{\partial\Omega_{\text{endo}}} (\mathbf{X} + \mathbf{u}) \cdot J\mathbf{F}^{-T}\mathbf{N}\, dS, \tag{3.13}$$

and note that the method of calculating the simulated volume $\tilde{V}^i$ depends upon $(\mathbf{X}+\mathbf{u})\cdot\mathbf{N}=0$ at the basal plane. These conditions hold in our model as the basal plane is defined with 0 longitudinal coordinate and longitudinal displacements are also set to 0 at this plane.

Finally, in order to have a single optimization target we combine the strain (3.10) and volume (3.13) mismatches into one single functional with parameter α,

$$I^i_\alpha = \alpha I^i_{\text{vol}} + (1-\alpha) I^i_{\text{strain}}, \tag{3.14}$$

where α controls the relative emphasis of the parameter estimation on volume or strain matching.

3.2.7 Parameter estimation as an optimization problem

The four elastic parameters a, b, a_f, b_f of the reduced Holzapfel-Ogden law (3.4) represent the passive elastic properties of the myocardium. Of the four parameters we leave the exponential b type parameters fixed and estimate the linear a type parameters by solving the following optimization problem

$$\begin{aligned} &\underset{a,a_f}{\text{minimize}} \quad \sum_{i=1}^{N_{\text{AS}}} I^i_{\text{vol}} \\ &\text{subject to} \quad \delta W = 0 \quad \forall\, i, \end{aligned} \tag{3.15}$$

where δW is given by (3.3), and $N_{\text{AS}}=3$ indicates the total number of measurements available in atrial systole.

In order to avoid the issue of an under-constrained optimization problem for the active contraction, we employ first order Tikhonov regularization to favor smoother contractions. Mathematically, the contraction parameter problem is then formulated as follows:

$$\begin{aligned} &\underset{\gamma}{\text{minimize}}\ I^i_\alpha + \|\text{Grad}\gamma\| \\ &\text{subject to } \delta W = 0 \quad \forall\, i, \\ &\qquad\qquad \gamma^i(\mathbf{X}) \in [0,1),\ \mathbf{X}\in\Omega, \end{aligned} \tag{3.16}$$

with regularization parameter λ. Here $\|\cdot\|$ refers to the standard L^2 norm. This

problem is solved for every measurement point i not in atrial systole.

The optimization problems (3.15) and (3.16) have two free parameters whose values must be chosen, namely the strain-volume weighing α and the regularization λ. The optimal choice of these parameters can be determined experimentally based on the L-criterion [20].

In general, the L-criterion applies to a situation in which a parameter controls the trade-off between two target values for minimization and where minimizing one target comes at the cost of potentially increasing the other. In such a situation the value of the two targets can be visualized as a curve parameterized by the control. This curve may have an L-shape, such that a good compromise between the two targets can be found in the corner.

Here, we consider λ in (3.16), whose value can be expected to influence the trade-off between the optimized values of the data functional I_α^i and the regularization functional $\|\nabla\gamma^i\|^2_{L^2(\Omega)}$. Similarly α can be expected to influence the trade-off between the optimized strain mismatch and volume mismatch in (3.15) and (3.16).

3.2.8 Implementation of mechanics and optimization solvers

For the numerical solution of the work balance equation (3.2) we employ a Galerkin finite element method with Taylor-Hood tetrahedral elements [22]; that is, a continuous piecewise quadratic representation of the displacement field and a continuous piecewise linear representation of the pressure field. The contraction parameter γ is represented discretely as continuous piecewise linear.

The software implementation of our finite element method is based on the package FEniCS [29], which automatically generates matrix and vector assembly code from a symbolic representation of the work balance equation (3.2). The resulting nonlinear systems were solved using the PETSc implementation of a Newton trust region algorithm [5], while the inner linear solves were handled by a distributed memory parallel LU solver [28].

To solve the optimization problems (3.15) and (3.16), we apply a sequential quadratic programming algorithm (SQP) [25]. This algorithm requires the derivatives of the function to be optimized, which in our case are the gradients of the mismatch functionals in problems (3.15) and (3.16) with respect to a, a_f and γ

respectively. These gradients are automatically computed by solving a machine derived adjoint equation via the software framework dolfin-adjoint [13].

In addition to gradients, the SQP algorithm requires evaluations of the mismatch functionals for given values of the control variables, which again relies on the solution of the work balance equation (3.2). In the case of problem (3.16), the control variable is γ, which has a very large influence on the solution of (3.2). Numerical solution of (3.2) by Newton's method depends upon having a good initial guess, which in our case are the values of the mechanical state variables, $\mathbf{u}, p$, resulting from the previous solve of (3.2). If the value of γ differs too greatly from one solve to the next the Newton algorithm might fail due to the root of the system being too far away from the initial guess. To avoid this problem we make use of a homotopy procedure that moves from one value of γ to the next in small increments, and solves (3.2) each time the value of γ is changed. This procedure is presented as Algorithm 1 and is similar to the one found in [34].

All algorithms, solvers and relevant data are publicly available online [14].

Algorithm 1 Max Increment Homotopy Newton Solver

Initial Variables

$\mathbf{u}_{prev}$	Previous displacement field
p_{prev}	Previous tissue hydrostatic pressure field
γ_{next}	Desired tissue contraction field
$\delta\gamma_{max}$	Maximum change in a component per Newton solve

Set

$M = \left\lceil \frac{\|\gamma_{next} - \gamma_{prev}\|_\infty}{\delta\gamma_{max}} \right\rceil$
$\gamma_0 = \gamma_{prev}$
$\mathbf{u}_0 = \mathbf{u}_{prev}$
$p_0 = p_{prev}$
$\delta\gamma = \frac{1}{M}(\gamma_{next} - \gamma_{prev})$

Use Newton's method M times with fixed increment $\delta\gamma$
for $i \in \{1...M\}$ **do**
  $\gamma_i = \gamma_{i-1} + \delta\gamma$
  Initialize Newton solver with $\mathbf{u}_{i-1}, p_{i-1}$
  Solve $\delta W(\mathbf{u}_i, p_i, \gamma_i) = 0$ for $\mathbf{u}_i, p_i$
Output $\mathbf{u}_i, p_i$

3.2.9 Error estimation

In order to evaluate the goodness of fit of the reproduction to synthetic data, we introduce two spatial error measures. The first is the maximum of the relative difference between the reproduced contraction parameter γ_{repr} and ground truth γ_{ground} averaged over AHA segments

$$\|\gamma\|_{\text{err}} = \max_i \frac{1}{17} \sum_{j=1}^{17} \frac{|G_j(\gamma^i_{\text{repr}}) - G_j(\gamma^i_{\text{ground}})|}{\max_k |G_j(\gamma^i_{\text{ground}})|}. \tag{3.17}$$

Note that this error measure makes use of the averaging operator G_j defined in (3.12). The second spatial error measure is based on the difference between the reproduced displacement field $\mathbf{u}_{\text{repr}}$ and the ground truth $\mathbf{u}_{\text{ground}}$

$$\|\mathbf{u}\|_{\text{err}} = \max_{\mathbf{X} \in \text{degrees of freedom of } \mathbf{u}} |\mathbf{u}_{\text{repr}}(\mathbf{X}) - \mathbf{u}_{\text{ground}}(\mathbf{X})|. \tag{3.18}$$

Finally in order to ease the interpretation of the strain and volume matches, we also consider averaged values of the optimization functionals

$$\overline{I}_{\text{strain}} = \frac{1}{51N} \sum_{i=1}^{N} I^i_{\text{strain}}, \tag{3.19}$$

$$\overline{I}_{\text{vol}} = \frac{1}{N} \sum_{i=1}^{N} \sqrt{I^i_{\text{vol}}} = \frac{1}{N} \sum_{i=1}^{N} \left| \frac{V^i - \tilde{V}^i}{V^i} \right|, \tag{3.20}$$

$$\overline{\|\nabla\gamma\|^2} = \frac{1}{N} \sum_{i=1}^{N} \|\nabla\gamma^i\|^2. \tag{3.21}$$

$$\tag{3.22}$$

Here N specifies the number of measurement points used in the optimization, and the factor 51 in the definition of $\overline{I}_{\text{strain}}$ originates from the number of AHA segments, 17, times the number of strain measurements per segment, 3.

3.3 Numerical Results

In this section we present the results of our numerical experiments. We first conduct parameter estimation using synthetic data generated by the wall motion model; this gives an idea of how well the algorithm can perform under noisy but otherwise ideal circumstances. Next, we carry out parameter estimation using the clinical data. Finally, we compare our spatially resolved contraction parameter results to those generated using a global contraction field.

In all of the experiments below, optimizations were terminated if the difference between the value of the mismatch in the current and previous iteration was less than 10^{-9} for the passive material parameter optimization and 10^{-6} for the active contraction parameter optimization, or if the SQP algorithm was not able to further reduce the mismatch value. For the identification of the elastic parameters, the SQP algorithm was initialized with the elastic material parameters given in Section 3.2.4. For the identification of the contraction field γ, the SQP algorithm was initialized with the value of γ from the previous measurement point in the cardiac cycle.

In order to obtain convergence of Newton's method for the solution of the virtual work equation (3.2), we set $\delta\gamma_{max} = 0.02$ in the homotopy Newton solver, (Algorithm 1) and limit γ to the interval $[0, 0.9]$. In the cases that Newton's method did not converge, $\delta\gamma_{max}$ was further reduced several times. If the reductions in $\delta\gamma_{max}$ did still not obtain Newton solver convergence, then a large value of the mismatch functional was returned so that the optimization algorithm would move to another part of the parameter space. A similar approach was applied when changing the endocardial pressure from one measurement point to the next. If the number of steps needed to reach the next endocardial pressure exceeded 100 steps, then the algorithm was stopped and was considered to have failed.

Strains were calculated with respect to the measurement point defined as start of atrial systole, as the reference geometry taken from the image corresponding to this point was assumed to be stress and strain free. Similarly, pressures for the clinical data were adjusted downward by the pressure measured at the start of atrial systole, 2.8 kPa, so that the adjusted start of atrial systole pressure was 0, and therefore compatible with the stress free assumption.

Using the patient data, we tested the three different mesh resolutions, low,

medium and high with 4407, 8401 and 16343 elements respectively. In all three cases we observed a good fit of the simulated to the clinical data, and have chosen to perform all of our computations on the medium resolution mesh.

The medium resolution mesh contained 2661 vertices, and as a consequence the contraction optimization problem 3.16 had just as many control variables. The value of the basal spring-constant was set to $k = 1.0$, as we noticed that this value gave reasonable motion at the base of the computational models.

3.3.1 Synthetic data

Using the synthetic data described in Section 3.2.4 as a target, we personalized the wall motion model using a series of strain-volume weighing (α) and regularization (λ) values. We first set $\lambda = 0$ and tested α from 0 to 1.0 in increments of 0.1. In the noisy case this yielded the trade-off curve Figure 3.3a, from which we selected $\alpha = 0.8$ based on the L-criterion described in Section 3.2.7. Next we set $\alpha = 0.8$ and tested λ from 0.0001 to 10.0 in increasing powers of 10, and selected the point 0.01 also based on the L-criterion. The trade-off curve for λ can be seen in Figure 3.3b.

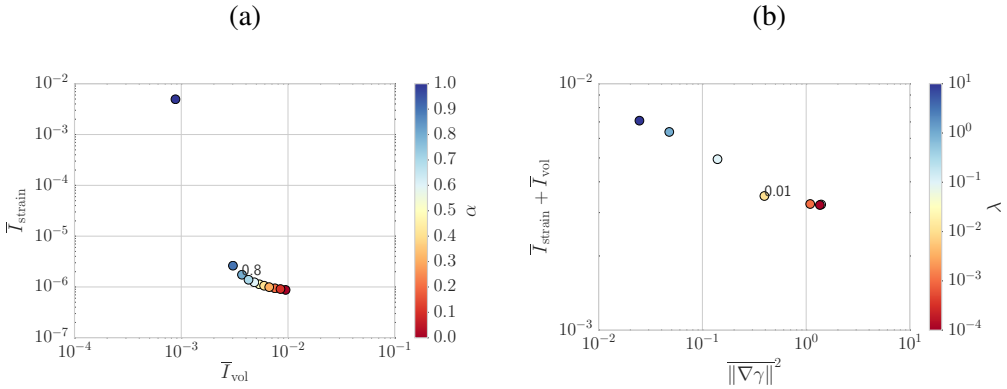

Figure 3.3: Trade-off curves for various α and λ values used in model personalization with noisy synthetic data as a target. Left: optimal average strain versus average volume misfits as defined in Equation (3.22) for a variety of choices of α and $\lambda = 0.0$. Right: Total average data functional versus contraction gradient size for a variety of λ values and $\alpha = 0.8$.

Table 3.2: Accuracy of reproduced synthetic data as compared to ground truth. The error measures are defined in Section 3.2.9. The value of the strain volume trade-off and regularization parameters are $\alpha = 0.8, \lambda = 0.01$.

	$\|\mathbf{u}\|_{\text{err}}$	$\|\gamma\|_{\text{err}}$
Clean	1.18 mm	0.0212
Noisy	1.39 mm	0.0434

With the α and λ values chosen, we quantified the error in reproduction of γ and the error in the displacement map for both the noisy and clean cases. These are displayed in Table 3.2. In both the noisy and clean cases the displacement map is reproduced with a maximum error less then 1.4 mm, and the reproduced contraction parameter has a relative regional error below 4.34%. As one would expect, the errors in the noisy case are higher than in the clean case.

The reconstructed displacement fields in the noisy case are shown alongside the ground truth in Figure 3.4. We note that the ground truth and reproduction look very similar.

3.3.2 Clinical data

Based on the clinical data described in Section 3.2.2 we calculated optimized elastic parameter and contraction values. The elastic parameters a, a_f, b, b_f were optimized solely using the volume mismatch I_{vol}. In Table 3.3 we show the results of the elastic parameter fitting. We note that the initial volume mismatch was already very small, and that the optimization algorithm managed to reduce this by circa 25%. The strain mismatch, though not explicitly optimized, was also slightly improved.

After completing the elastic parameter estimation we next turned to optimizing the contraction parameter γ. In order to identify good functional weighing values, α and λ, we followed a variation of the procedure used in the synthetic data case. We first ran optimizations with $\lambda = 0$ and α ranging from 0 to 1.0 in increments of 0.1. All of these optimizations failed due to Newton solver non-convergence. Next we tested $\lambda = 1.0$ and α in the same increments. These optimizations succeeded, but the resulting strain-volume trade-off curve did not contain any obvious corner values that would allow us to pick an α by the L-criterion. By visually inspecting

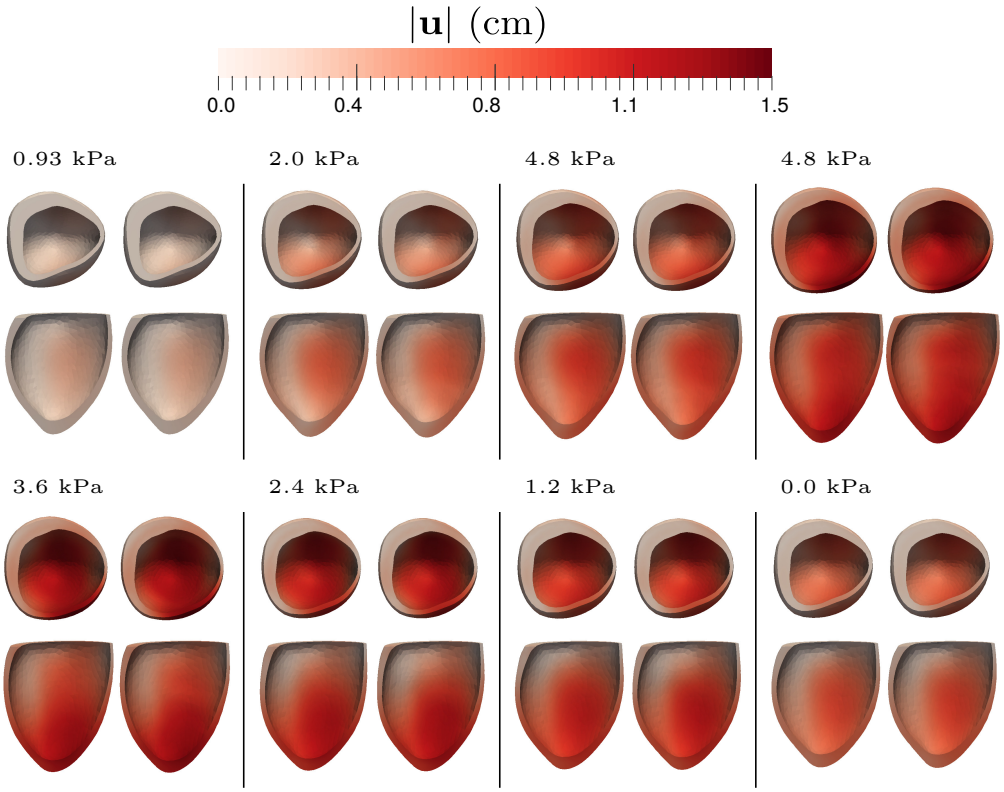

Figure 3.4: Reconstruction of displacement based on noisy synthetic data for 8 measurement points using $\alpha, \lambda = 0.8, 0.01$. For each point the ground truth is displayed on the left and the reconstruction on the right.

Table 3.3: Optimized and initial patient-specific elastic parameter values and objective functionals. Note that only the volume and not the strain functional was used in the optimization.

	a (kPa)	b	a_f (kPa)	b_f	$\overline{I}_{\text{vol}}$	$\overline{I}_{\text{strain}}$
Initial	0.291	5.0	2.582	5.0	0.0098	0.0024
Optimized	0.335	5.0	2.586	5.0	0.0073	0.0023

the simulated vs. measured volume and strain curves we identified $\alpha = 0.9$ as giving good strain and volume matching. We next tested $\alpha = 0.9$ and $\lambda = 0.0001$ to 1.0 in increasing powers of 10. From these trials only $\lambda = 0.01$ and above were convergent, with $\lambda = 0.01$ giving the best strain and volume functional values. We therefore chose $\alpha, \lambda = 0.9, 0.01$ as the values of the functional weights.

With these α and λ values we were able to obtain an excellent agreement of the model to the measured regional strain values and pressure-volume loop. Simulated versus measured plots of these data are given in Figure 3.5 for strain and Figure 3.6 for the pressure-volume loop. In Figure 3.7 we plot the initial and optimized mismatch values for the measurement points for which γ was active. We note that the strain mismatch is reduced by at least two orders of magnitude at each measurement point, and that the volume is in most cases significantly reduced as well, except at around a single point near 50% of the cardiac cycle where the volume fit was slightly worsened.

Visualizations of the optimized displacement field are given in Figure 3.8. These displacements are very heterogeneous, as expected for a dyssynchronous ventricle.

3.3.3 Clinical data with a synchronous contraction

In this section we repeat the estimation of γ from the clinical data, but instead of representing γ as a piecewise linear function we represent it with a single global value, which gives a synchronous contraction. This reduces the number of controls in the optimization problem (3.16) to 1, and makes the λ parameter unnecessary, as $\|\nabla\gamma\|^2_{L^2(\Omega)} = 0$ for a spatially constant γ. Due to solver stability issues we were not able to use the same strain - volume weighing, $\alpha = 0.9$ as in the piecewise linear case. A slight increase of this parameter to $\alpha = 0.95$ yielded convergent optimization results which we present here.

In Figure 3.9 we plot the optimal strain and volume fit functionals using both a piecewise linear and a global γ. The plot shows that the piecewise representation of γ gave in most points at least an order of magnitude improvement in the mismatch values over the global representation of γ.

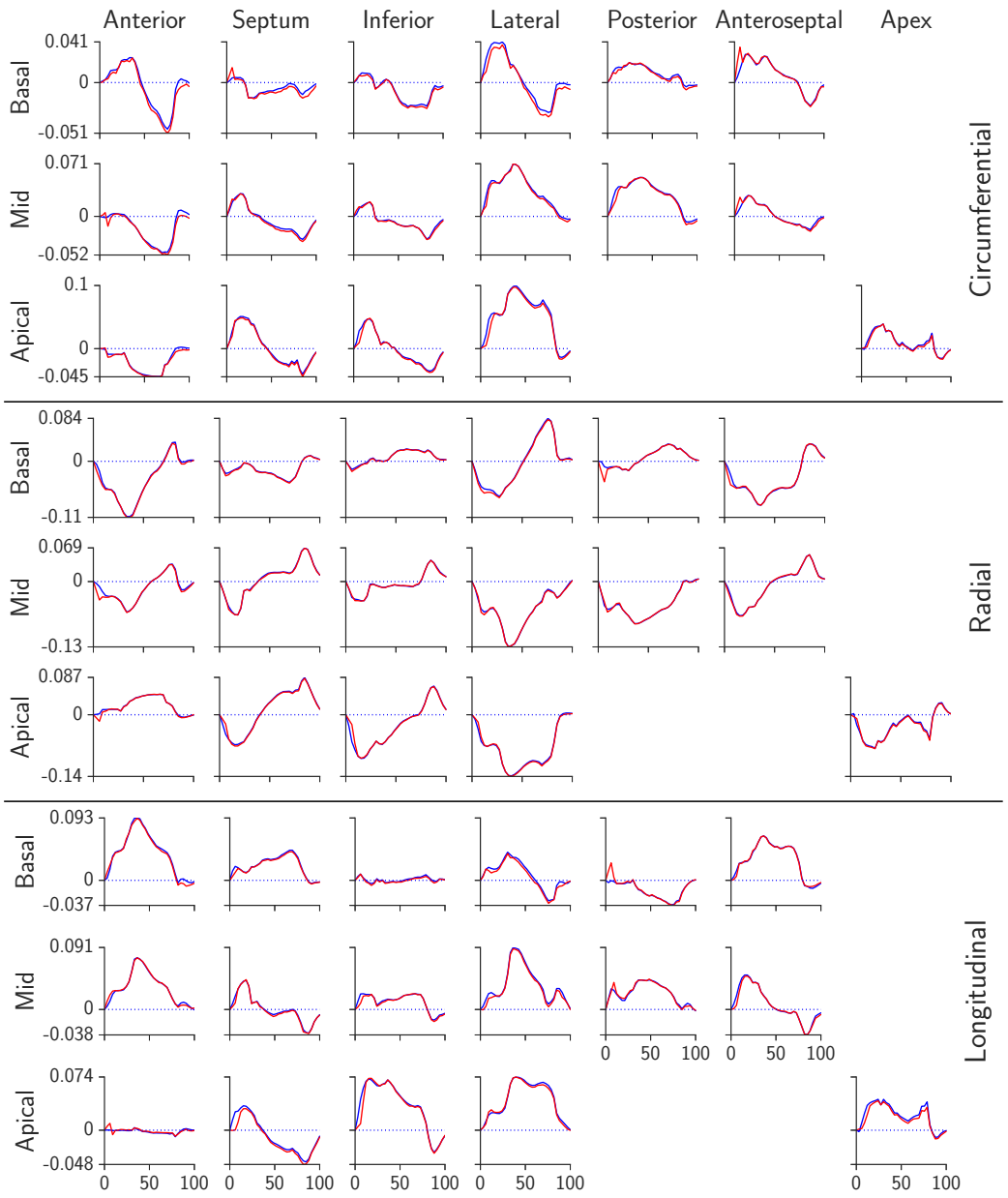

Figure 3.5: Comparison of regional strain curves starting in end diastole. In red: optimized wall motion model data. In blue: clinical data from speckle tracking echocardiography. In each plot the y-axis represents strain while the x-axis shows the progression in time of the cardiac cycle as a percentage.

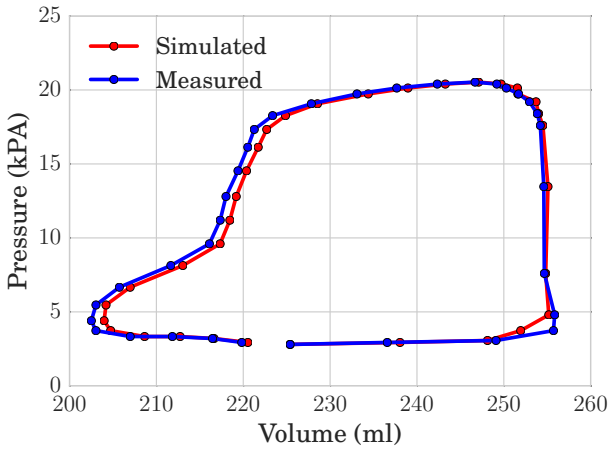

Figure 3.6: Clinically measured (blue) versus optimized wall motion model (red) left ventricular cavity volumes.

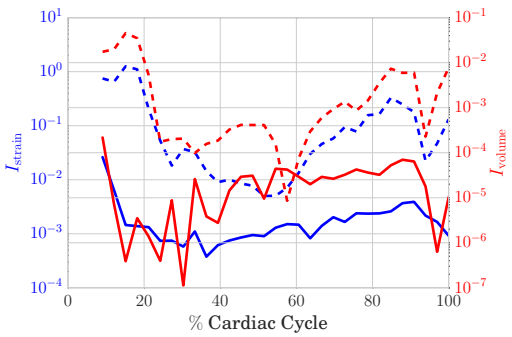

Figure 3.7: Initial and optimized values of the strain (blue) and volume (red) mismatch functionals for measurement points used to estimate the contraction γ. Dotted lines represent the initial value of the functional evaluated at the previous γ value, while the solid line shows the optimized value.

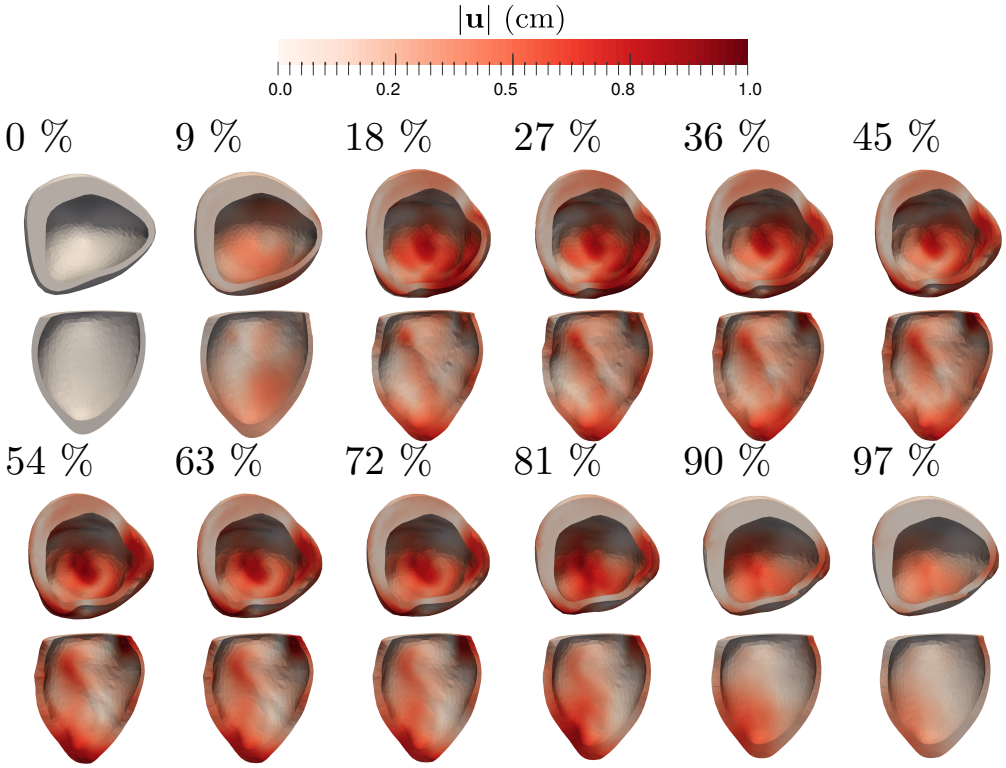

Figure 3.8: Two views of displacement magnitudes calculated by the wall motion model optimized to clinical data for different points in the cardiac cycle.

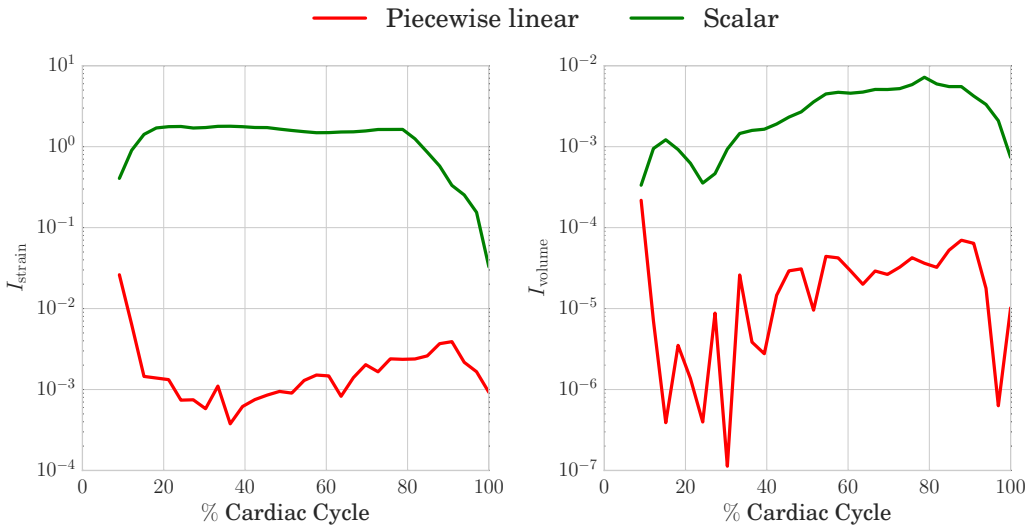

Figure 3.9: Comparison of optimized mismatch functional values obtained from a global and piecewise linear representation of γ. The volume functional is plotted on the left and the strain functional on the right.

3.4 Discussion

3.4.1 Mathematical model and fit to data

We conducted parameter estimations with synthetic data in order to test our data assimilation procedure under idealized circumstances. These tests employed a contraction pattern and pressure curve that were not physiologically motivated, but rather were designed to simply capture the essential mechanical effects of the cardiac cycle; that is, regionally varying muscle shortening and elastic distention due to pressure. These tests also incorporated noise in strain and volume which were derived directly from clinical measurements. The results of the synthetic data estimations gave an accurate reproduction of the original data. Displacements were matched to within 1.18 mm in the clean case and to 1.39 mm in the noisy case, whereas the contraction parameter was estimated regionally to within 2.1 % in the clean case and 4.3 % in the noisy case.

Several past studies [31, 37] have included objective functionals consisting of strain and volume components with equal weighing given to both. We have shown

that it may be possible to improve such data assimilation procedures by tuning the relative weight of strain and volume components. Specifically in our synthetic data case, Figure 3.3a, we were able to locate the point $\alpha = 0.8$ in the corner of the strain-volume trade-off curve that gave a good compromise between volume and strain matching.

The clinical measurements that we used to demonstrate our data assimilation technique had several pathological features. Firstly the data indicated a large leak of volume in the early relaxation phase, as can be seen in Figure 3.6. In a healthy heart this phase occurs iso-volumetrically. Furthermore there is a great variation in the timing and magnitude of peak strain, Figure 3.5, which indicates a dyssynchronous contraction. Our data assimilation procedure was able to reproduce these pathological features with high accuracy. The largest discrepancies between model and image based strains were in atrial systole, where no contraction was simulated. This discrepancy could possibly be reduced by allowing for more spatial resolution in the elastic parameters, in a similar way to the contraction.

By performing the contraction fitting with both a high resolution and a synchronous global parameter we were able to show the necessity of using the former in order to accurately represent the dyssynchronous contraction. Indeed, Figure 3.9 shows that the spatially resolved parameter achieved fit values that were several orders of magnitude better than with the global parameter.

In [24] it was shown by computational modelling that a synchronous left ventricular contraction leads to a homogeneous strain distribution, which was expected based on measurements of healthy left ventricles. Our results show what one would expect in the dyssynchronous case: namely that a synchronous contraction, modelled with a global parameter, does not give the expected strain distribution, as observed in our clinical measurements.

In many computational modelling studies [7, 10, 35] the force of contraction in the myocardium is modelled by an increase in fiber tension triggered by an electrical activation. In contrast to this the force of contraction is indirectly modeled by the elastic and contraction parameters in our study. Given a fixed contraction parameter γ, smaller material parameters indicate weaker contractions and vice-versa. In this way our approach relies more on accurate clinical data and less on assumptions than if the contraction had been given by a model.

3.4.2 Algorithmic considerations

The discrete implementation of the optimization problem (3.16) has as many control variables as there are vertices in the computational mesh, making the use of adjoint gradient calculations highly advantageous. During the optimization of the contraction parameter γ a typical evaluation of the work-balance equation (3.2) took 8.4 seconds running in parallel on 8 cores. The evaluation of the functional gradient took 13.5 seconds using the adjoint method, also with 8 cores. In contrast to this a one sided finite difference evaluation of the gradient, as used in [2, 39], would require 2661 work-balance equation evaluations, with an extrapolated compute time of over 6 hours.

The proper choice of regularization parameter is an issue that is common in the field of inverse problems. In our study we also included an additional strain-volume weighing parameter α that we tuned in order to obtain a good balance between strain and volume matching. In our synthetic data case, we were able to decouple the problems of identifying good α and λ values by fixing one parameter and then tuning the other based on the L-criterion. This allowed us to obtain an accurate reproduction of the underlying displacement and contraction fields. In the patient data case we were limited to the range of α and λ values for which our Homotopy-Newton solver was able to secure convergence, and by a lack of identifiable corner points in the resulting trade-off curves. Nevertheless we were able to obtain good α and λ values ad-hoc that lead to excellently matching strain curves and pressure-volume relations.

3.4.3 Limitations

The results obtained in this article were limited by issues pertaining to the choice of mathematical model, quality of clinical data, numerical stability, and the design of the data assimilation algorithm. Firstly, the boundary conditions of the ventricle wall motion model did not account for the effects of the right ventricular pressure on the septum, and the mechanical coupling to the neighbouring structures: left atrium, right ventricle and pericardium. Furthermore, the motion model neglected the effects of visco-elasticity, tissue compressibility [42], inertia, and myocardial sheet microstructure. Finally the reference geometry that we used for our calculations came from an echocardiographic image in which there was a non-zero level

of blood pressure. The blood pressures we used in our patient specific model were off by the 2.8 kPa which we subtracted in order to have 0 pressure in the reference geometry. This pressure adjustment meant that the elastic stiffness of the ventricle was underestimated by our elastic parameter estimation, as the mathematical model operated at a lower pressure than measured in the patient's heart.

The accuracy of the optimized motion model is limited by uncertainties in the clinical strain and volume measurements, which are related to echocardiographic image quality, image sample rate, and speckle tracking algorithm accuracy. The level of detail in the reproduced motion was limited by the spatial resolution of the strain data, which was only available to us as regional averages.

Finally there were several algorithmic limitations. Firstly our procedures for choosing the functional weights α and λ were not optimal. In both the synthetic and clinical data case the weight values were chosen by parameter sweeps that kept a single parameter fixed, which did not account for possibly better α, λ combinations lying outside of the areas we tested. Next the Newton-Homotopy solver was not able to solve (3.2) for all the values of γ that were suggested by the SQP algorithm. Further restrictions on the space of control variables or better nonlinear solvers are needed to improve the stability of the contraction optimization. Finally the SQP optimization algorithm that we employed was a local search only, that is only one minimum of the objective is calculated. Better parameter fits may be possible with global optimization methods that explore multiple minima.

3.5 Conclusion and Future Outlook

By employing high resolution data assimilation we were able to capture the detailed motion of a dyssynchronous left ventricle in a computational model with an excellent fit of model observations to data. This demonstrates the power of the data assimilation method, which can also be applied to other models and or model parameters.

In the future we would like to improve and further automate our high resolution data assimilation method so that it can be employed on cohorts of patients. This would allow us to search for patterns among groups of patients that could lead to further understanding of dyssynchrony.

Author Declaration

All of the clinical data for this study was collected with the approval of the Norwegian national ethics committee, REC, and in accordance to the Helsinki Declaration of 1975, as revised in 2000.

Acknowledgements

Computations were performed on the Abel supercomputing cluster at the University of Oslo via Notur projects nn9316k and nn9249k.

Bibliography

[1] Liya Asner, Myrianthi Hadjicharalambous, Radomir Chabiniok, Devis Peresutti, Eva Sammut, James Wong, Gerald Carr-White, Philip Chowienczyk, Jack Lee, Andrew King, et al. Estimation of passive and active properties in the human heart using 3D tagged MRI. *Biomechanics and modeling in mechanobiology*, pages 1–19, 2015.

[2] Kevin F Augenstein, Brett R Cowan, Ian J LeGrice, Poul MF Nielsen, and Alistair A Young. Method and apparatus for soft tissue material parameter estimation using tissue tagged magnetic resonance imaging. *Journal of biomechanical engineering*, 127(1):148–157, 2005.

[3] Matthias Aurich, Florian André, Marius Keller, Sebastian Greiner, Alexander Hess, Sebastian J Buss, Hugo A Katus, and Derliz Mereles. Assessment of left ventricular volumes with echocardiography and cardiac magnetic resonance imaging: real-life evaluation of standard versus new semiautomatic methods. *Journal of the American Society of Echocardiography*, 27(10):1017–1024, 2014.

[4] Gabriel Balaban, Martin S Alnæs, Joakim Sundnes, and Marie E Rognes. Adjoint multi-start-based estimation of cardiac hyperelastic material parameters using shear data. *Biomechanics and Modeling in Mechanobiology*, pages 1–13, 2016.

[5] S Balay, J Brown, K Buschelman, WD Gropp, D Kaushik, MG Knepley, L Curfman McInnes, BF Smith, and H Zhang. PETSc web page. `http://www.mcs.anl.gov/petsc`, 2015.

[6] JD Bayer, RC Blake, G Plank, and NA Trayanova. A novel rule-based algorithm for assigning myocardial fiber orientation to computational heart models. *Annals of biomedical engineering*, 40(10):2243–2254, 2012.

[7] Ezgi Berberoğlu, H Onur Solmaz, and Serdar Göktepe. Computational modeling of coupled cardiac electromechanics incorporating cardiac dysfunctions. *European Journal of Mechanics-A/Solids*, 48:60–73, 2014.

[8] Joris Bols, Joris Degroote, Bram Trachet, Benedict Verhegghe, Patrick Segers, and Jan Vierendeels. A computational method to assess the in vivo stresses and unloaded configuration of patient-specific blood vessels. *Journal of Computational and Applied Mathematics*, 246:10–17, 2013.

[9] Manuel D Cerqueira, Neil J Weissman, Vasken Dilsizian, Alice K Jacobs, Sanjiv Kaul, Warren K Laskey, Dudley J Pennell, John A Rumberger, Thomas Ryan, Mario S Verani, et al. Standardized myocardial segmentation and nomenclature for tomographic imaging of the heart a statement for healthcare professionals from the cardiac imaging committee of the Council on Clinical Cardiology of the American Heart Association. *Circulation*, 105(4):539–542, 2002.

[10] Radomir Chabiniok, Philippe Moireau, P-F Lesault, Alain Rahmouni, J-F Deux, and Dominique Chapelle. Estimation of tissue contractility from cardiac cine-MRI using a biomechanical heart model. *Biomechanics and modeling in mechanobiology*, 11(5):609–630, 2012.

[11] H Delingette, F Billet, K C L Wong, M Sermesant, K Rhode, M Ginks, C A Rinaldi, R Razavi, and N Ayache. Personalization of cardiac motion and contractility from images using variational data assimilation. *Biomedical Engineering, IEEE Transactions on*, 59(1):20–24, January 2012.

[12] A Evangelista, P Nardinocchi, PE Puddu, L Teresi, C Torromeo, and V Varano. Torsion of the human left ventricle: experimental analysis and computational modeling. *Progress in biophysics and molecular biology*, 107(1):112–121, 2011.

[13] Patrick E Farrell, David A Ham, Simon W Funke, and Marie E Rognes. Automated derivation of the adjoint of high-level transient finite element programs. *SIAM Journal on Scientific Computing*, 35(4):C369–C393, 2013.

[14] Henrik Finsberg and Gabriel Balaban. High resolution data assimilation of cardiac mechanics. `http://www.bitbucket.org/finsberg/cardiac_highres_dataassim`, 2016.

[15] H Gao, WG Li, L Cai, C Berry, and XY Luo. Parameter estimation in a Holzapfel–Ogden law for healthy myocardium. *Journal of engineering mathematics*, 95(1):231–248, 2015.

[16] MW Gee, Ch Förster, and WA Wall. A computational strategy for prestressing patient-specific biomechanical problems under finite deformation. *International Journal for Numerical Methods in Biomedical Engineering*, 26(1):52–72, 2010.

[17] Christophe Geuzaine and Jean-François Remacle. Gmsh: A 3-D finite element mesh generator with built-in pre-and post-processing facilities. *International Journal for Numerical Methods in Engineering*, 79(11):1309–1331, 2009.

[18] Sjur Gjerald, Johan Hake, Simone Pezzuto, Joakim Sundnes, and Samuel T Wall. Patient–specific parameter estimation for a transversely isotropic active strain model of left ventricular mechanics. In *Statistical Atlases and Computational Models of the Heart-Imaging and Modelling Challenges*, pages 93–104. Springer, 2015.

[19] Myrianthi Hadjicharalambous, Radomir Chabiniok, Liya Asner, Eva Sammut, James Wong, Gerald Carr-White, Jack Lee, Reza Razavi, Nicolas Smith, and David Nordsletten. Analysis of passive cardiac constitutive laws for parameter estimation using 3D tagged MRI. *Biomechanics and modeling in mechanobiology*, 14(4):807–828, 2015.

[20] Per Christian Hansen and Dianne Prost O'Leary. The use of the l-curve in the regularization of discrete ill-posed problems. *SIAM Journal on Scientific Computing*, 14(6):1487–1503, 1993.

[21] Gerhard a Holzapfel and Ray W Ogden. Constitutive modelling of passive myocardium: a structurally based framework for material characterization. *Philosophical transactions. Series A, Mathematical, physical, and engineering sciences*, 367(1902):3445–75, sep 2009.

[22] P Hood and C Taylor. Navier-stokes equations using mixed interpolation. *Finite element methods in flow problems*, pages 121–132, 1974.

[23] Oslo University Hospital. Acute feedback on left ventricular lead implantation location for cardiac resynchronization therapy (CCI impact). `https://clinicaltrials.gov`, 2016.

[24] RCP Kerckhoffs, PHM Bovendeerd, JCS Kotte, FW Prinzen, K Smits, and T Arts. Homogeneity of cardiac contraction despite physiological asynchrony of depolarization: a model study. *Annals of biomedical engineering*, 31(5):536–547, 2003.

[25] Dieter Kraft et al. A software package for sequential quadratic programming. Deutsche Forschungs- und Versuchsanstalt fuer Luft- und Raumfahrt e.V. (DFVLR), Germany. `http://hdl.handle.net/10068/147127`, 1988.

[26] Adarsh Krishnamurthy, Christopher T Villongco, Joyce Chuang, Lawrence R Frank, Vishal Nigam, Ernest Belezzuoli, Paul Stark, David E Krummen, Sanjiv Narayan, Jeffrey H Omens, Andrew D McCulloch, and Roy Cp Kerckhoffs. Patient-specific models of cardiac biomechanics. *Journal of computational physics*, 244:4–21, july 2013.

[27] Sander Land, Steven Niederer, Pablo Lamata, Nicolas P Smith, et al. Improving the stability of cardiac mechanical simulations. *Biomedical Engineering, IEEE Transactions on*, 62(3):939–947, 2015.

[28] Xiaoye S. Li and James W. Demmel. SuperLUDIST: A scalable distributed-memory sparse direct solver for unsymmetric linear systems. *ACM Trans. Mathematical Software*, 29(2):110–140, June 2003.

[29] Anders Logg, Kent-Andre Mardal, Garth N. Wells, et al. *Automated Solution of Differential Equations By the Finite Element Method*. Springer, 2011.

[30] S Marchesseau, H Delingette, M Sermesant, M Sorine, K Rhode, S G Duckett, C a Rinaldi, R Razavi, and N Ayache. Preliminary specificity study of the Bestel-Clément-Sorine electromechanical model of the heart using parameter calibration from medical images. *Journal of the mechanical behavior of biomedical materials*, 20:259–71, May 2013.

[31] Dimitri Mojsejenko, Jeremy R McGarvey, Shauna M Dorsey, Joseph H Gorman III, Jason A Burdick, James J Pilla, Robert C Gorman, and Jonathan F Wenk. Estimating passive mechanical properties in a myocardial infarction using MRI and finite element simulations. *Biomechanics and modeling in mechanobiology*, 14(3):633–647, 2014.

[32] Paola Nardinocchi and Luciano Teresi. On the active response of soft living tissues. *Journal of Elasticity*, 88(1):27–39, 2007.

[33] Dominik Neumann, Tommaso Mansi, Bogdan Georgescu, Ali Kamen, Elham Kayvanpour, Ali Amr, Farbod Sedaghat-Hamedani, Jan Haas, Hugo Katus, Benjamin Meder, et al. Robust image-based estimation of cardiac tissue parameters and their uncertainty from noisy data. In *Medical Image Computing and Computer-Assisted Intervention–MICCAI 2014*, pages 9–16. Springer, 2014.

[34] S Pezzuto, D Ambrosi, and A Quarteroni. An orthotropic active–strain model for the myocardium mechanics and its numerical approximation. *European Journal of Mechanics-A/Solids*, 2014.

[35] Simone Rossi, Toni Lassila, Ricardo Ruiz-Baier, Adélia Sequeira, and Alfio Quarteroni. Thermodynamically consistent orthotropic activation model capturing ventricular systolic wall thickening in cardiac electromechanics. *European Journal of Mechanics-A/Solids*, 48:129–142, 2014.

[36] Maxime Sermesant, Philippe Moireau, Oscar Camara, Jacques Sainte-Marie, Rado Andriantsimiavona, Robert Cimrman, Derek LG Hill, Dominique Chapelle, and Reza Razavi. Cardiac function estimation from MRI using a heart model and data assimilation: advances and difficulties. *Medical Image Analysis*, 10(4):642–656, 2006.

[37] Kay Sun, Nielen Stander, Choon-Sik Jhun, Zhihong Zhang, Takamaro Suzuki, Guan-Ying Wang, Maythem Saeed, Arthur W Wallace, Elaine E Tseng, Anthony J Baker, et al. A computationally efficient formal optimization of regional myocardial contractility in a sheep with left ventricular aneurysm. *Journal of biomechanical engineering*, 131(11):111001, 2009.

[38] Hari Sundar, Christos Davatzikos, and George Biros. Biomechanically-constrained 4D estimation of myocardial motion. In *Medical Image Computing and Computer-Assisted Intervention–MICCAI 2009*, pages 257–265. Springer, 2009.

[39] Vicky Y Wang, H I Lam, Daniel B Ennis, Brett R Cowan, Alistair a Young, and Martyn P Nash. Modelling passive diastolic mechanics with quantitative MRI of cardiac structure and function. *Medical image analysis*, 13(5):773–84, October 2009.

[40] Ken CL Wong, Maxime Sermesant, Kawal Rhode, Matthew Ginks, C Aldo Rinaldi, Reza Razavi, Hervé Delingette, and Nicholas Ayache. Velocity-based cardiac contractility personalization from images using derivative-free optimization. *Journal of the mechanical behavior of biomedical materials*, 43:35–52, 2015.

[41] Jiahe Xi, Pablo Lamata, Jack Lee, Philippe Moireau, Dominique Chapelle, and Nic Smith. Myocardial transversely isotropic material parameter estimation from in-silico measurements based on a reduced-order unscented Kalman filter. *Journal of the mechanical behavior of biomedical materials*, 4(7):1090–1102, 2011.

[42] FC Yin, CC Chan, and Robert M Judd. Compressibility of perfused passive myocardium. *American Journal of Physiology-Heart and Circulatory Physiology*, 271(5):H1864–H1870, 1996.

4 Paper III: Data Assimilation of Cardiac Elastic Heterogeneity in an Infarcted Human

Data Assimilation of Cardiac Elastic Heterogeneity in an Infarcted Human

Gabriel Balaban[1,2], Henrik Finsberg[1,2], Einar Hopp[4], Joakim Sundnes[1,2], Samuel Wall[1,5], Marie E. Rognes[1,3]

1. Simula Research Laboratory, P.O. Box 134 1325 Lysaker, Norway
2. Department of Informatics, University of Oslo, P.O. Box 1080 Blindern 0316 Oslo, Norway
3. Department of Mathematics, University of Oslo, P.O. Box 1053 Blindern 0316 Oslo, Norway
4. Faculty of Radiology and Nuclear Medicine, Oslo University Hospital, P.O. Box 1078 Blindern, 0316 Oslo, Norway
5. Department of Mathematical Science and Technology, Norwegian University of Life Sciences, Universitetstunet 3 1430 Ås, Norway

Abstract: In myocardial infarction muscle tissue of the heart is damaged as a result of ceased or severly impaired blood flow. Survivors have an increased risk for further complications, possibly leading to heart failure. Material properties play an important role in determining post-infarction outcome. Due to spatial variation in scarring, material properties can be expected to vary throughout the tissue of a heart after an infarction. In this study we propose a data assimilation technique that can efficiently estimate heterogeneous elastic material properties in a personalized model of cardiac mechanics. As part of the data assimilation an unloaded geometry estimation algorithm is designed and tested on synthetic data. Furthermore, data assimilation is carried out on a clinical dataset consisting of regional left ventricular strains, and in-vivo pressures during atrial systole from a human with a myocardial infarction. Good matches to regional strains are obtained and simulated equibiaxial tests are carried out to demonstrate regional heterogeneities in stress-strain relationships.

4.1 Introduction

Myocardial infarction (MI) is a condition in which muscle tissue in the heart is damaged due to a loss of blood supply. After an infarction, there is an increased risk for further complications, such as rupture, infarct expansion, ventricular remodeling, hypertrophy, and heart failure [18]. Post MI, the elastic properties of the myocardium have been shown to play a large role in determining the outcome [12, 32].

A promising way to study the elastic properties of in-vivo myocardium is by mathematical modelling and computer simulation. Via the use of simulation it is possible to create an in-silico representation of a patient's heart after an infarction. This opens up new possibilities for quantification of elasticity, beyond what is available in medical imaging today. Additionally, an in-silico model that is personalized to a patient can potentially simulate the effects of treatments or therapies on the patient, thereby improving the outcome and reducing risks after MI.

A key step in creating a personalized in-silico model is data assimilation. This involves adjusting mathematical model parameters in order to fit the model to patient data. A properly fitted model can then be said to reflect the state of a patient's heart. Several past studies have presented data assimilation techniques for the creation of in-silico personalized elasticity models of infarcted hearts. The first such study [35] modeled an infarction in a sheep heart. The modeled left ventricular end diastolic volume (EDV) was matched to the measured EDV by tuning a single elastic parameter.

Hand tuning of multiple parameters was carried out in [8] in order to calibrate a computational model of a porcine heart to in-vivo data before and after MI. Good matches to pressure-volume relations were obtained. Hand tuning was also used to identify elastic parameters in a fluid-structure interaction model of a healthy and an infarcted human heart [13].

More recent studies have employed a genetic algorithm in order to identify elastic parameters by minimizing the mismatch between simulated and measured strains and volumes. In the paper which pioneered this technique [31] an infarction was induced in a pig which divided the ventricle into healthy and infarcted areas. Elastic parameters were defined for these two areas and then successfully identified. In a follow up study [30], these same parameters were tracked over the

course of 12 weeks in 7 pigs. The mechanical changes observed in-silico agreed well with previous data collected from excised hearts. A further study employed the methodology of [31] in order to evaluate the effects of a hydrogel therapy on infarct stiffness [9].

Parameter estimation for infarcted humans was considered in [10]. In the study a single elastic parameter was tuned to match model based to measured left ventricular (LV) cavity volumes for 10 patients. The tuned parameter values were shown to be significantly different in healthy and infarcted hearts.

In the general clinical setting the spatial distribution of fibrotic tissue in a heart can be quite complex, which mostly likely leads to heterogeneities in elastic properties after MI. The study of such heterogeneities necessitates a data assimilation procedure which can resolve spatial differences in elastic model parameters. We address this by introducing an adjoint-gradient-based optimization method for the estimation of elastic parameters. This method is able to efficiently optimize high dimensional parameter sets, and thereby estimate spatially resolved elastic parameters throughout the myocardium. As a demonstration we present a personalized in-silico elasticity model based on data collected from a heart failure patient with a heterogeneous distribution of fibrotic tissue. Our data consist of regional strains, which were computed by speckle tracking echocardiography, a pressure transient obtained from a catheter, and a quantification of segmental scar burden based on late enhancement gadolinium magnetic resonance imaging.

Recently it has been shown that the choice of reference geometry has a significant effect on in-vivo elastic parameter estimation [33]. In order to account for this we have designed a combined reference geometry and elastic parameter estimation algorithm and applied it to our clinical data. Additionally, we have carried out synthetic data tests using the combined algorithm in a simplified model with globally constant parameters.

4.2 Methods and Materials

4.2.1 Clinical Data

Clinical data were obtained with the permission of staff of Oslo University Hospital in the context of the Impact study [23]. Specifically, we consider the case of a

64 year old man in systolic heart failure, with left bundle branch block, coronary artery disease, and chronic infarction predominantly in the inferior and posterior sections of the left ventricular wall.

Prior to treatment, the patient had echocardiography, late gadolinium enhancement MRI, and left ventricular (LV) pressure measurements taken, which are the basis for the clinical data used in this study. Pressure recordings were carried out using a standard over the wire technique; that is, a pressure catheter (Millar micro catheter) was placed in the LV through a multipurpose catheter via the right femoral artery. A stable position inside the LV cavity was established by withdrawing the multipurpose catheter into the ascending aorta. Pressure data were obtained automatically within the frequency range of 0 – 1000Hz and digitized (Powerlab system, AD Instruments) before offline analyses were performed with a low pass filter of 200Hz.

A 4D echocardiography examination of the patient's LV was performed using a GE Vingmed E9 machine. Speckle tracking motion analysis was carried out with GE's software package EchoPac. This resulted in regional strain curves defined for a 17 segment delineation of the LV according to the standard AHA representation [7]. The strain curves were measured in the local left ventricular longitudinal, radial and circumferential directions. Data from 6 beats were combined in order to obtain a single sequence of images for a single heartbeat. From this sequence 6 separate measurement points of left ventricular strain during atrial systole were obtained. It was observed that the speckle tracking algorithm was able to accurately follow the motion of the basal and midwall segments, but that the tracking of the apical segments was inaccurate, most likely due to the presence of apical rocking. Finally 6 left ventricular cavity volumes were obtained from the same segmentations that were used to calculate the 6 sets of strain.

Strain and pressure data were synchronized. The start of atrial systole in the pressure measurements was identified from left atrial ECG data which were taken simultaneously. In the echocardiographic images the start of atrial systole was identified by the onset of longitudinal stretching following diastasis, and the end of diastole was identified by the onset of longitudinal contraction. For strain measurements after the first, corresponding pressures were registered using the frequency of image aquisition and timing of pressure measurements.

Pressure data were available only to a precision of 1 mmHg and consequently

strain points 2 and 3 shared the same pressure. In order to give each strain point a unique pressure an additional cubic polynomial smoothing was carried out. Both smoothed and original pressure data are plotted in Figure 4.1.

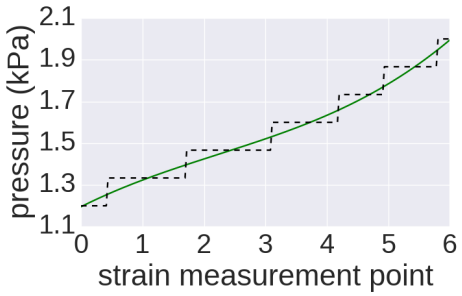

Figure 4.1: Left ventricular pressure trace with original catheter data in dotted black and cubic polynomial smoothed data in solid green.

Cardiac MRI imaging was performed with a 1.5 Tesla scanner (Skyra, Siemens, Erlangen, Germany). The amount of myocardial fibrosis was quantified on a per region basis from short axis late gadolinium enhancement images acquired 10 to 20 minutes after intravenous injection of 0.2 mmol/kg of gadoterat meglumine (Guerbet, Villepinte, France). This resulted in an estimated volume ratio of fibrotic to healthy tissue for each myocardial segment. In this analysis the apex region was merged into the neighbouring apical regions, giving a 16 segment division. This data is summarised in Figure 4.2. Sample ultrasound and MRI images are shown in Figure 4.3.

4.2.2 Mesh Creation

In order to capture the details of the patient ventricular geometry in our in-silico model we created a computational geometry based on a 3-D ultrasound image. This image was taken at the start of atrial systole, when the pressure was at a minimum. Using GE's EchoPac software, we extracted triangulated data points for left ventricular endocardial and epicardial surfaces. These surfaces were cut by a plane fitted to the basal points of the surfaces, and adjusted so that the ventricular volume of the computational geometry was within 1 mL of the volume measured

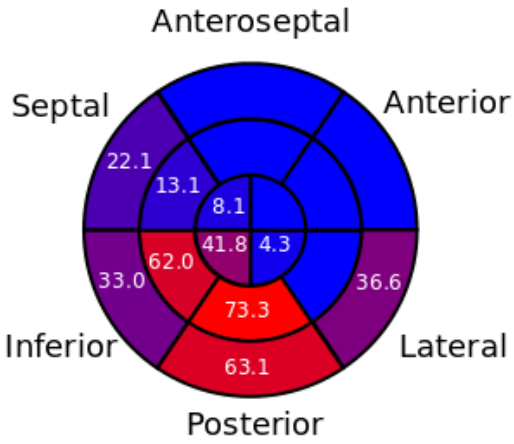

Figure 4.2: Results of regional quantification of myocardial scar burden based on late enhancement gadolinium MRI images. The inner, middle and outer rings represent apical, midwall and basal sections respectively. Scar-free segments are coloured blue, whereas scarred segments are coloured red in proportion to the amount of scar tissue they contain. The proportion of scar is also given as a percentage in scarred segments.

(a) 3-D echocardiography

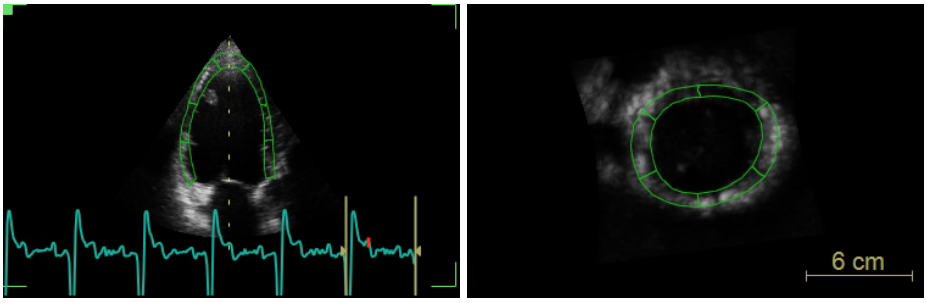

(b) Late enhancement gadolinium MRI

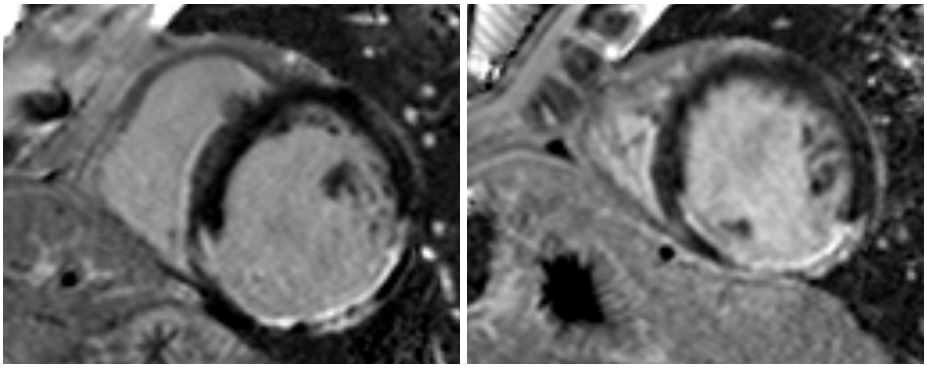

Figure 4.3: Sample ventricular images used in this study. 4.3a: Long and short axis 2D slices of a 3-D echocardiographic image along with tracked segments in green and an ECG signal. 4.3b: short axis late enhancement gadolinium MRI images used for regional scar quantification. Fibrotic sections of the myocardium appear in white.

in the image. Using the epi, endo and basal surfaces as boundaries we created a volumetric mesh using Gmsh [14]. This mesh contained 741 vertices and 2214 tetrahedra. AHA zones were deliniated on this volumetric mesh based on data provided by EchoPac, so that our AHA zones were consistent with those used to calculate image based strains. Finally, local myocardial fiber orientations were assigned with a helix angle of 40 degrees on the endocardium rotated clockwise throughout the ventricular wall to -50 degrees on the epicardium using a rule based method [5]. Snapshots of the image based geometry, along with a sample of fibers and AHA segments, are shown in Figure 4.4.

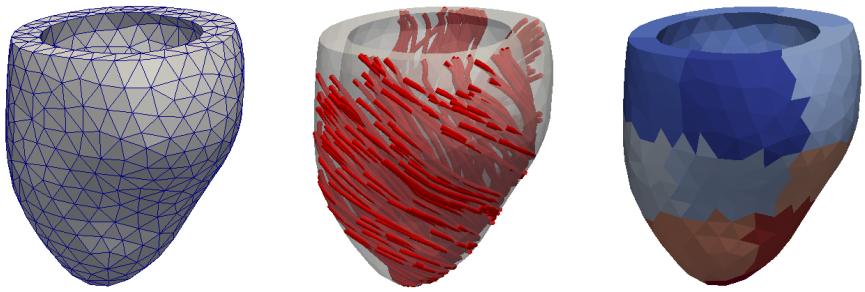

Figure 4.4: Left: image based mesh with 2214 elements. Middle: streamline representation of a sample of fibers. Right: AHA regions marked in separate colours.

4.2.3 Elastic Wall Motion Model

In order to simulate the motion of the left ventricle throughout atrial systole we adopt a quasi-static continuum mechanics description. That is we consider a field $\mathbf{u}$ giving the displacement map between a reference configuration Ω and a deformed configuration undergoing a pressure load. Furthermore, we define the deformation gradient $\mathbf{F} = \text{Grad}\mathbf{u} + \mathbf{I}$, which is the strain measure we use for our clinical and simulated strain data.

In our wall motion model the myocardium is considered to be a hyperelastic material with strain energy given by a transversely isotropic simplification of the

Holzapfel-Ogden law [21],

$$\psi(\mathbf{C}) = \frac{a}{2b}\left(e^{b(I_1(\mathbf{C})-3)} - 1\right) + \frac{a_f}{2b_f}\left(e^{b_f(I_{4f}(\mathbf{C})-1)_+^2} - 1\right). \tag{4.1}$$

This equation defines the amount of energy, ψ, stored per unit volume myocardium undergoing the strain $\mathbf{C} = \mathbf{F}^T\mathbf{F}$. The notation $(\cdot)_+$ refers to $\max\{\cdot, 0\}$, and the mechanical invariants I_1 and I_{4f} are defined as

$$I_1(\mathbf{C}) = \text{tr } \mathbf{C}, \qquad I_{4f} = \mathbf{e_f} \cdot \mathbf{C}\mathbf{e_f}, \tag{4.2}$$

with $\mathbf{e_f}$ indicating the local myocardial fiber direction. The material parameters a, a_f, b, b_f are scalar quantities which influence the shape of the stress-strain relationship, and which we estimate in order to personalize the elastic properties of the computational model to patient data. Furthermore, in order to improve the numerical stability of our finite element solver, as shown in [27], we employ a modified strain energy functional

$$\tilde{\psi}(\mathbf{C}) = \psi\left(J^{-\frac{2}{3}}\mathbf{C}\right). \tag{4.3}$$

The elastic energy (4.3) is embedded into a standard pressure-displacement variational formulation of incompressible hyperelasticity [Chapter 8.5 of [19]]. Displacements are set to 0 in the longitudinal direction at the base of the ventricular geometry by a Dirichlet boundary condition. Movement in the other directions at the base is restricted by a linear spring with constant k.

The total variational equation, including the effects of blood pressure, p_{blood}, and the basal spring, is given by

$$\begin{aligned} 0 = &\int_\Omega \mathbf{P} + pJ\mathbf{F}^{-T} : \text{Grad } \delta\mathbf{u}\, dV + \int_\Omega (J-1)\delta p\, dV \\ &+ p_{\text{blood}} \int_{\partial\Omega_{\text{endo}}} J\mathbf{F}^{-T}\mathbf{N} \cdot \delta\mathbf{u}\, dS + \int_{\partial\Omega_{\text{base}}} k\mathbf{u} \cdot \delta\mathbf{u}\, dS. \end{aligned} \tag{4.4}$$

In this equation $\mathbf{P}$ is the first Piola-Kirchoff tensor $\mathbf{P} = \frac{\partial\tilde{\psi}}{\partial\mathbf{F}}$, $\partial\Omega_{\text{endo}}$ the endocardium, $\partial\Omega_{\text{base}}$ the ventricular base, $\mathbf{N}$ the unit outward facing normal, p the hydrostatic pressure, and $\delta\mathbf{u}, \delta p$ virtual variations in the displacement and pressure respectively. Equation (4.4) is discretized by a mixed finite element method with

Taylor - Hood elements [22], that is a piecewise quadratic representation of the displacement field and a piecewise linear representation of the pressure.

The software implementation of the finite element vector and matrix assembly code is based on the package FEniCS [29]. Nonlinear systems are solved using the PETSc SNES implementation of a Newton line search algorithm [4], while the inner linear solves are handled by a distributed memory parallel LU solver [28].

4.2.4 Elastic Parameter Estimation

In order to personalize the elastic material properties of our computational mechanics model we make use of a least squares minimization of the mismatch between model derived and measured strains. More specifically we define the functional

$$I_{\text{data}} = \sum_{i}^{N_{sm}} \sum_{j}^{N_{reg}} \left| \text{diag}_{crl} \left(\frac{1}{|\Omega_j|} \int_{\Omega_j} \mathbf{F}_i \mathbf{F}_0^{-1} \, dV \right) - \text{diag}_{crl} \left(\tilde{\mathbf{F}}_i \right) \right|^2 . \tag{4.5}$$

Here $N_{sm} = 6$ is the number of strain measurements available in atrial systole and $N_{reg} = 16$ the number of AHA regions, with the apex segment excluded for compatibility with the late enhancement MRI data. Furthermore Ω_j denotes the jth AHA segment, and $|\Omega_j|$ the corresponding segmental volume. Also $\mathbf{F}_i$ is the simulated deformation gradient corresponding to image i, and $\tilde{\mathbf{F}}_i$ the image based deformation gradient. Finally, $\text{diag}_{crl}(\cdot)$ indicates the vector of circumferential, radial and longitudinal diagonal components of the tensor argument. Note that by adjusting the simulated deformation gradient by $\mathbf{F}_0^{-1}$ we are able to measure simulated strains from a reference that is consistent with that used to calculate the image based strains [33].

During data assimilation, each of the four elastic parameters a, b, a_f, b_f is spatially resolved as a piecewise linear function having a separate degree of freedom at each vertex of the computational geometry. This allows for a greater heterogeneity of motion to be modelled than with globally constant parameters, but greatly increases the number of parameters that need to be optimized. This can lead to a potentially under-constrained optimization with many parameter combinations with similar optimal I_{data} values. One way to choose among these parameter sets is to pick the smoothest set. We therefore quantify the solution smoothness

with a 1st order Tikhonov regularization functional

$$I_{\text{smooth}} = \frac{1}{|\Omega|} \sum_{z \in \{a, a_f, b, b_f\}} \int_\Omega |\text{Grad } z|^2 \, dV, \tag{4.6}$$

where $|\Omega|$ is the volume of the simulated myocardium. The total functional for our optimization is then

$$I = I_{\text{data}} + \lambda I_{\text{smooth}} \tag{4.7}$$

with regularization parameter λ. In this study we chose λ empirically by running optimizations with various λ values, plotting the corresponding optimal I_{data} and I_{smooth} values, and choosing a corner point corresponding to the smoothest set of parameters that fits the data well. This procedure is inspired by the so called L-criterion [17].

The total functional (4.7) is minimized by simultaneously optimizing all of the degrees of freedom of the 4 elastic parameters. This optimization is carried out by a sequential quadratic programming (SQP) algorithm [25]. Each iteration of the SQP algorithm requires an evaluation of the functional (4.7), and the gradient of the functional with respect to all of the material parameter variables. This gradient is calculated efficiently by the adjoint gradient method [Equation 13 of [3]] symbolically derived by the software package dolfin-adjoint [11]. In particular, the computational cost of the adjoint gradient does not significantly depend on the number of optimization parameters, of which there are 2964 in our study. This compares favorably with a one sided finite difference approach to functional gradient calculation, which would require 2964 model realizations, one for each optimization parameter.

4.2.5 Unloaded Geometry Estimation

In order to make use of the elastic wall motion model described in Section 4.2.3 we require a reference geometry Ω from which to calculate displacements. Additionally, this geometry should be stress-free in order to be compatible with the requirements of hyperelastic theory. The presence of residual stresses and in-vivo blood pressure means that such a geometry is generally unavailable from medical imaging. In our study we do not estimate residual stresses, but do address the

issue of pressure loading.

The effects of pressure on the image based geometry can be accounted for by deforming the image based geometry in a series of updates according to the backward displacement method [6]. The backward displacement method calculates a reference geometry that matches the in-vivo geometry when inflated to the in-vivo pressure. In order to do this it requires knowledge of the values of the elastic parameters. Consequently the elastic parameter optimization and backward displacement algorithms are interdependent. In order to handle this dependency we have modified the original backward displacement method by optimizing the material parameters after each backward displacement update. Furthermore we recalculate the fibers of our reference geometry at each iteration by deforming the image based fibers by the deformation gradient of the backward displacement. By doing this we ensure that the resulting reference fibers match those of the image based geometry when deformed by the corresponding in-vivo pressure. Our modified backward displacement algorithm is presented as Algorithm 2.

Algorithm 2 Unloaded geometry and material parameter estimation algorithm

for $j \in \{1...\}$ until convergence **do**

Inflate Ω^j to in-vivo pressure with material paramaters $a^j, b^j, a_f^j, b_f^j, {\mathbf{e_f}}^j$ to get displacement $\mathbf{u}_{\Omega^j}$.

Apply backward displacement update at each vertex $\mathbf{X}$ $\mathbf{X}_{\Omega^{j+1}} = \mathbf{X}_{\Omega^0} - \mathbf{u}_{\Omega^j}$.

Update fibers ${\mathbf{e_f}}^{j+1} = \mathbf{F}(-\mathbf{u}_{\Omega^j}){\mathbf{e_f}}^0$.

Obtain $a^{j+1}, b^{j+1}, a_f^{j+1}, b_f^{j+1}$ by minimization of the regularized strain mismatch functional (4.7).

4.3 Results

In the following sections we present the numerical results of this study. We first give the results of a synthetic data test of Algorithm 2, then move onto the re-

sults of applying the algorithm to our clinical data. Finally, we carry out simulated equibiaxial extensions tests using the material parameters calculated from the clinical data.

4.3.1 Synthetic data test

In order to test our implementation of Algorithm 2, we have carried out a set of simple synthetic data tests with spatially constant parameters. As a consequence $I_{\text{smooth}} = 0$ in the tests and only the data functional I_{data} is minimized.

Our procedure was as follows. First we defined a ground truth set of elastic parameters $a = a_f = 1.5$ kPa. This excluded the b parameters which were simply fixed to $b = b_f = 5.0$ during the whole test. The image based ventricular geometry, as shown in Figure 4.4, was chosen as the ground truth 0 pressure geometry for this test. This geometry was inflated to 0.1 kPa using the ground truth parameters, and a 0.1 kPa mesh was then extracted. The original mesh was then further inflated to 0.2 kPa and average regional strain measurements were taken with respect to the 0.1 kPa mesh.

The synthetic data test then consisted of trying to reproduce the 0 pressure ground truth geometry and material parameters by running Algorithm 2 on the 0.1 kPa mesh, using the synthetic strains as a target for the material parameter optimization.

We ran the synthetic test 16 times, each time initializing the material parameters a and a_f for a different combination of values in the set $\{0.5, 1, 5, 10\}$ with units kPa. The algorithm was stopped when the maximum distance between the current and ground truth 0.1 kPa pressure meshes was less than 0.0005 mm. This occurred in all cases, and on average after 14.8 iterations.

Of the 16 trials, 14 reproduced very closely the ground truth 0 pressure mesh and ground truth material parameter values. In two of the cases, corresponding to the initial parameters $a = 10$, $a_f = 0.5$ and $a = 10$, $a_f = 0.5$, the material parameter optimization returned the lower bounds $a = 0.15$, $a_f = 0.15$. Consequently the optimized meshes for these two cases were also inaccurate, with a maximum distance (D_{max}) of 8.80 mm between optimized and target meshes in both cases.

The results for the 14 successful optimizations are presented in Table 4.1. We note that the estimation of the unloaded geometry and material parameters were

	D_{max} (mm)	I_{data}	ϵ_a (kPa)	ϵ_{a_f} (kPa)
Initial				
mean	4.15	336	3.29	4.61
std	0	253	3.32	3.84
Optimized				
mean	9.63×10^{-04}	3.71×10^{-5}	1.27×10^{-04}	8.74×10^{-04}
std	2.75×10^{-5}	2.99×10^{-8}	3.25×10^{-6}	1.30×10^{-5}

Table 4.1: Mean and standard deviation of results for 14 out of 16 successfully fitting synthetic data tests of the combined pressure-free geometry and material parameter estimation procedure, Algorithm 2. The symbol D_{max} denotes the maximum distance of the current unloaded mesh to the target mesh. ϵ_a and ϵ_{a_f} denote the respective absolute errors in estimating the target parameters $a = a_f = 1.5$ kPa.

consistently highly accurate for these cases.

4.3.2 Patient Specific Model

As a first step towards creating a personalized model of the infarcted left ventricle in atrial systole, we identified suitable values for the regularization parameter λ. This was done by carrying out a series of trial material parameter optimizations with the image based geometry used as the reference. These trials were performed for the λ values (1, 10, 50, 100, 500, 1000) and consisted of minimizing the regularized strain mismatch functional (4.5) once without deforming the image based geometry. Material parameters were initialized with globally constant values $a = 1.291, b = 5.0, a_f = 2.582, b_f = 5.0$. These values were selected from a patient-specific study of healthy ventricles [Table 5 case P2 of [2]].

Optimal data and regularization functional values I^*_{data} and I^*_{smooth} were obtained for each of the λ values tested and the corner point $\lambda = 100.0$ was selected. These are shown in Figure 4.5.

With the λ parameter identified, we then ran the full geometry and material parameter estimation, Algorithm 2. The stopping criterion was based on the dif-

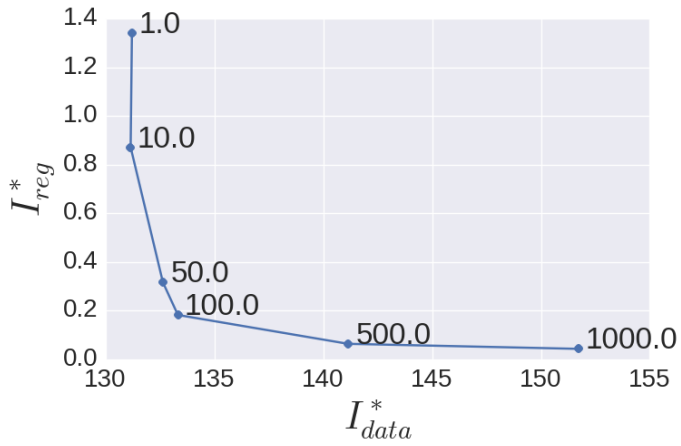

Figure 4.5: Optimal data versus regularization functionals obtained from optimizations with a range of regularization parameter values for the case $k = 0.1$ and in-vivo data. The regularization values are written next to their respective data points in the plot.

ference in volumes of successive unloaded geometries. If this difference was less than 1 mL the algorithm was stopped. We tested basal spring k values in the set $\{0.01, 0.1, 1.0, 10.0\}$ with unit kPa. For the stiff cases $k = 1.0$ and $k = 10.0$ simulated pressure increases caused significant outward bending at the base, leading to large displacements in the midwall. Applying these displacements negatively to the image based geoemtery produced self-intersecting walls. In the very compliant case $k = 0.01$ there were whole ventricle translations. The case $k = 0.1$ avoided both of these problems and was therefore chosen.

The creation of the personalized model required 6 unloading iterations, during which the cavity volume of the reference geometry decreased from 186.0 mL to 33.7 mL. Material parameters were optimized 7 times, requiring between 100-281 SQP iterations for the minimization of the functional. More specific details about the progression of Algorithm 2 are presented in Table 4.2. We note that the spatial averages of the parameters decreased with nearly every unloading iteration, while the optimal function values I^* increased.

Measured vs. optimized strain-pressure curves are plotted in Figure 4.6. We note that the optimized curves match the measured points fairly well, except for

Table 4.2: Performance of the unloaded geometry and material parameter estimation, Algorithm 2, applied to the clinical dataset. The first and second columns contain the unloading iteration number and the cavity volume of the corresponding mesh. The third column I^* contains the values of the optimized total functional at each unloading iteration and the fourth column the number of SQP iterations needed to minimize I. The final four columns contain material parameter values averaged over the entire ventricular geometry.

Iteration	Volume (mL)	I^*	Opt. Iter.	a (kPa)	b	a_f (kPa)	b_f
0	186.0	133.5	100	2.41	3.04	1.29	3.58
1	72.0	168.8	172	2.03	3.01	1.15	3.53
2	63.0	158.1	281	1.67	2.60	0.95	3.36
3	48.3	160.1	104	1.63	2.51	0.95	3.26
4	40.0	194.5	108	1.57	2.43	0.91	3.20
5	33.5	211.8	119	1.60	2.43	0.94	3.22
6	33.7	220.7	103	1.64	2.38	0.91	3.13

Table 4.3: Regionally averaged material parameter values. Data in italics indicates the presence of fibrosis in the corresponding myocardial segment.

	Region	a	b (kPa)	a_f	b_f (kPa)
Basal	Anterior	0.742	0.390	0.508	2.242
	Anteroseptal	0.417	0.838	1.326	2.140
	Septum	*0.277*	*0.789*	*1.305*	*1.597*
	Inferior	*0.176*	*3.904*	*0.839*	*7.108*
	Posterior	*2.374*	*8.699*	*1.206*	*5.723*
	Lateral	*1.358*	*3.931*	*1.261*	*4.504*
Mid	Anterior	2.300	1.903	1.028	2.912
	Anteroseptal	1.339	0.365	0.601	0.817
	Septum	*0.475*	*0.939*	*0.415*	*1.044*
	Inferior	*0.295*	*1.825*	*0.464*	*4.012*
	Posterior	*2.220*	*2.050*	*0.526*	*4.663*
	Lateral	1.353	6.059	0.651	4.305
Apical	Anterior	4.405	3.690	1.650	3.448
	Septum	*1.701*	*0.589*	*0.794*	*0.852*
	Inferior	*1.995*	*0.494*	*0.856*	*1.736*
	Lateral	*2.596*	*1.029*	*0.803*	*2.852*

the circumferential strain in the basal-anteroseptal segment, which is matched poorly. Furthermore, we show the optimal material parameter fields in Figure 4.7 and note that the results are fairly smooth, yet still show significant variation across the ventricle. Segmental averages of the material parameters are given in Table 4.3.

Geometries at 0, begin atrial systole, and end diastolic pressures are shown in Figure 4.8, along with a wireframe of the original image based geometry overlaid over the begin atrial systole geometry for comparison. We note that the wire-frame and the begin atrial systole geometry lie close together, indicating that Algorithm 2

(a) Longitudinal Strains

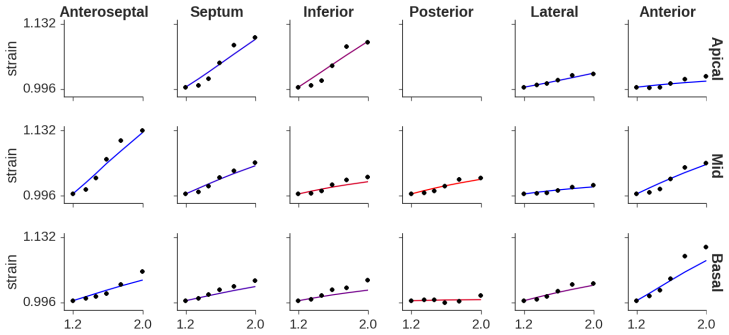

(b) Circumferential Strains

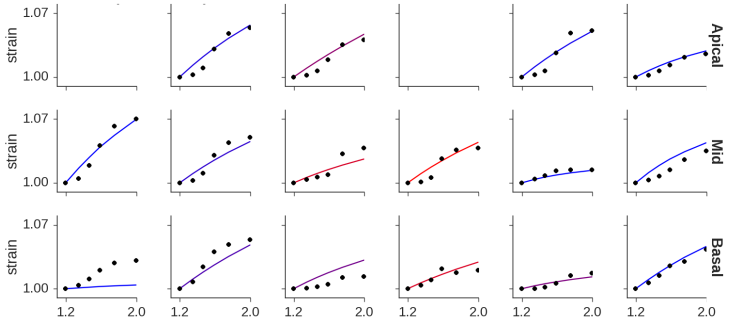

(c) Radial Strains

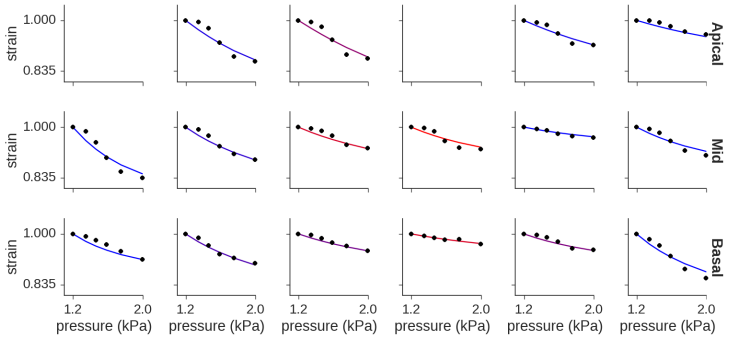

Figure 4.6: Optimized model (solid line) vs. measured (black dot) strains. Model strains are calculated as regional averages of the corresponding diagonal component of the deformation gradient $\mathbf{F}$. The line colouring indicates the relative amount of scar in a segment as in Figure 4.2.

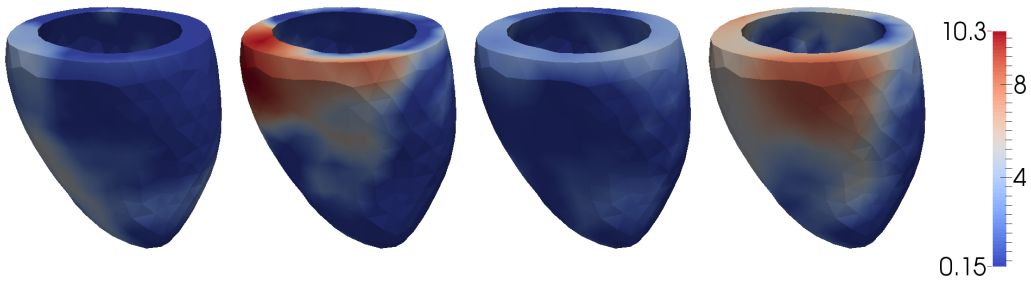

Figure 4.7: Optimal material parameters visualized on the image based ventricular geometry. The orientation of the geometry is such that the anterior, posterior and lateral segments face the viewer. From left to right are parameters a, b, a_f, b_f.

was able to approximate the image based geometry fairly well. Finally we have plotted the pressure volume relationship of the ventricle in Figure 4.9 along with measured volumes. These are compared to the empirically derived relationship predicted by [24]. We note that the optimized model data lie within circa 10 mL of the measured data and that both measured and model data vary significantly from the empirical relationship.

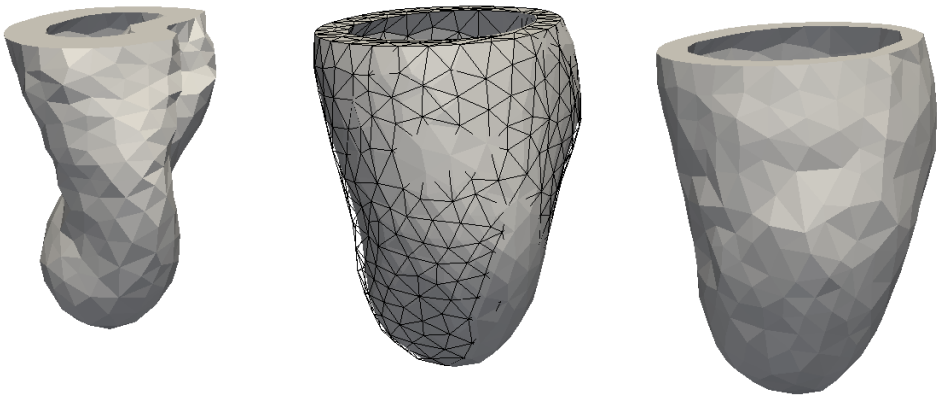

Figure 4.8: Geometries personalized by the unloaded geometry and material parameter estimation algorithm. To the left is the pressure-free unloaded geometry, in the middle the geometry at the start of atrial systole and to the right is the end diastolic geometry. The middle image also includes the original image-based geometry as a black wire-frame for comparison.

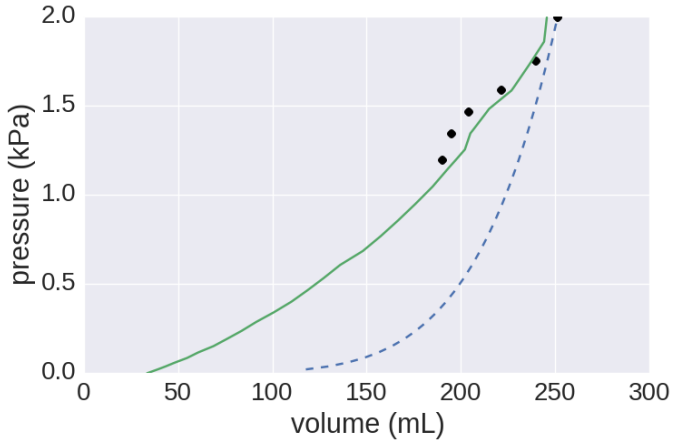

Figure 4.9: Comparison of pressure volume relationships. The black dots represent data from 4-D echocardiography, the green line simulated data from the optimized and unloaded ventricular mechanics model, and the dotted blue line the theoretical relationship predicted by the formula of Klotz et al. [24].

4.3.3 Simulated Equibiaxial Testing

The personalization of the mechanics model to the patient data resulted in 4 material parameters that are resolved in space over the ventricular geometry. These parameters are relevant for mathematical modelling but do not give an intuitive idea of stiffness in the ventricle. Stiffness can be visualized in terms of stress-strain relationships, with stiffer materials giving higher stresses than softer ones at the same levels of strain.

In order to visualize regional differences in stress-strain relationships in the patient ventricle, we have conducted a series of in-silico equibiaxial extension tests, using analytical values for the stresses based on [Equations 17,18 of [20]]. A test was conducted per myocardial region using the corresponding regionally averaged material parameter values from Table 4.3. The results of these tests are presented in Figures 4.10a and 4.10b. We note that the cross fiber stresses were nearly negligible as compared to the fiber stresses, indicating a high degree of anisotropy. Fiber stresses were high in the heavily scarred inferior to posterior, mid to basal segments, and in the scar-free mid lateral and apical anterior segments.

(a) Fiber

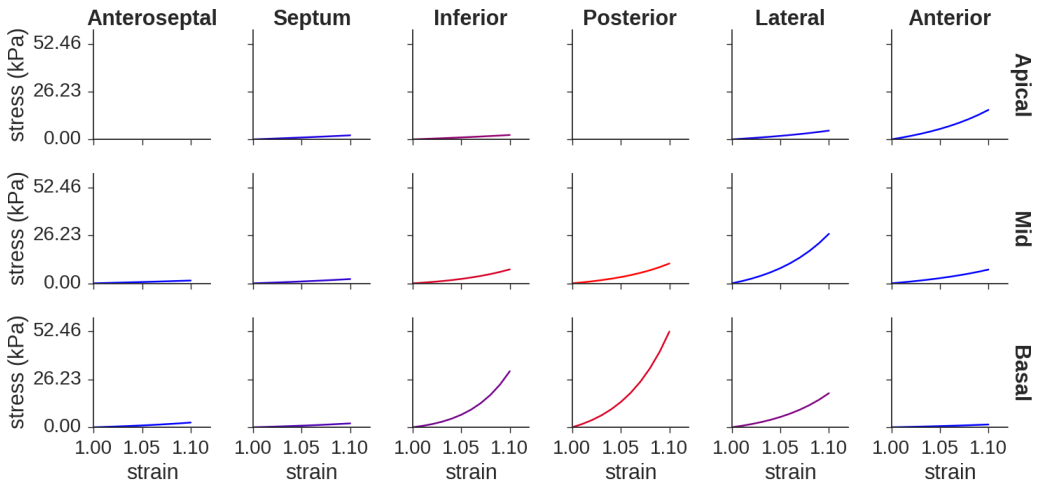

(b) Cross Fiber

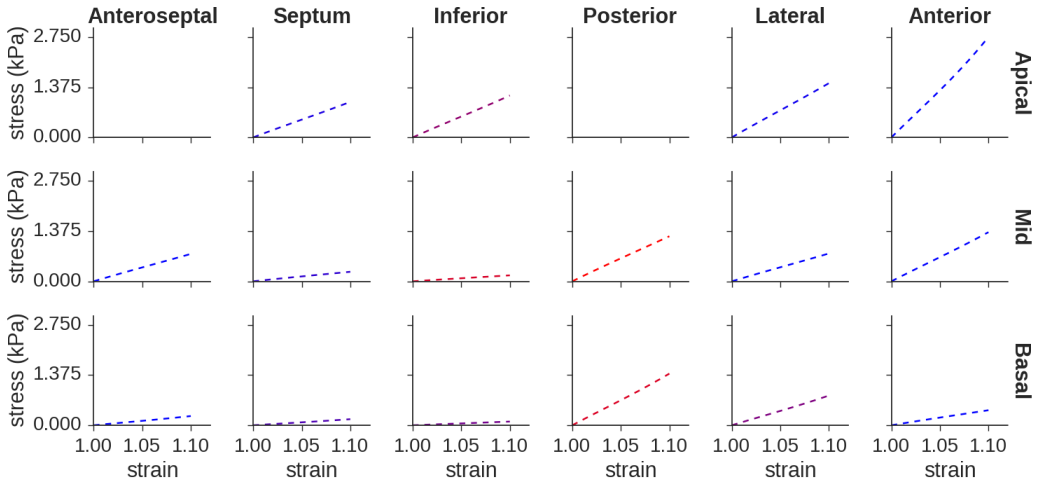

Figure 4.10: Results of simulated equibiaxial extension testing. Solid curves and dotted curves represent stresses in the fiber direction and cross fiber direction respectively. 4.10a and 4.10b: Stress-strain curves generated from simulated equibiaxial extension tests performed with average material parameter values obtained from each myocardial segment. Strains are measured in terms of the in-plane fiber and cross-fiber diagonal components of the deformation gradient $\mathbf{F}$. Blue segments are healthy whereas red contain scar tissue in proportion to their colour as in Figure 4.2.

Finally we have also averaged the stress-strain relationships for the healthy and fibrotic regions, excluding the apical regions due to poor quality in the speckle tracking. These curves are plotted in Figure 4.11 and show that on average, the infarcted segments have just over twice as much fiber stress for a given state of equibiaxial strain as the healthy segments.

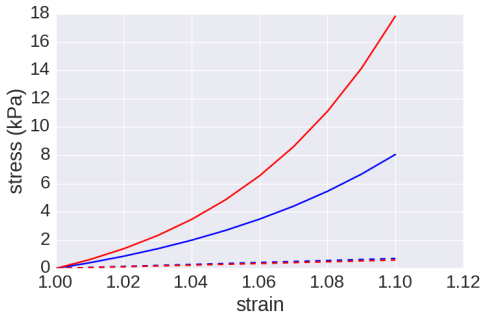

Figure 4.11: Average of stress-strain relationships for scar-free (blue) and scar containing (red) basal and midwall segments. Solid curves and dotted curves represent stresses in the fiber direction and cross fiber direction respectively.

4.4 Discussion

By applying our adjoint gradient-based data assimilation method we were able to estimate spatially heterogeneous material properties in an infarcted left ventricle. Additionally, we have shown the applicability of our combined reference geometry and material parameter estimation algorithm. In particular this algorithm was able to very accurately reproduce synthetic data, and also converged in volume for our infarcted in-vivo case.

Several combined unloaded geometry and material parameter estimation algorithms have been introduced in the past. In the earliest studies [1, 26, 34] material parameters were tuned to fit the pressure-volume relationship predicted by the empirically derived relation of Klotz et al. [24]. In [36] an algorithm was presented that estimated both material parameters and unloaded geometry from in-vivo data, without accounting for the dependency between the material parameter and geometry estimation. Recently in-vivo data was used to estimate both material parame-

ters and unloaded geometry [33] and an iterative algorithm to deal with the mutual dependency of parameter estimation and geometry unloading was introduced.

In our study we faced rather large geometrical changes during the unloading of the image based geometry, which were a consequence of soft material parameters needed to fit the strain measurements. We were unable to compute these geometrical changes with the algorithm presented in [33], as the backward displacements became large and led to mesh self-intersections. By modifying the order of geometrical updates and parameter optimizations in the algorithm, we were able to make smaller changes to the geometry between each material parameter optimization, and thereby more gradually unload the geometry. This modified algorithm successfully converged with our clinical data. During the course of the geometrical unloading, we observed a softening of optimized material properties as the geometry was unloaded. This is in agreement with the results of [33].

We also observed a gradual worsening of the optimal functional values I^* during unloading. Indeed the optimal value was 133.5 before unloading and 220.7 afterwards. In particular we noticed that the circumferential strain in the basal anteroseptal segment was underestimated after unloading and well fitted before. This discrepency can be attributed to a circumferential buckle in the unloaded geometry which was not present in the in-vivo geometry. In the unloaded geometry simulated increases in pressure had the effect of unbuckling the basal anteroseptal segment instead of expanding it circumferentially.

The volume of the unloaded geometry predicted by our model is about 4 times smaller than that predicted by the empirical relationship of Klotz et al. [24], and the measured in-vivo volumes also deviate significantly from the plotted empirical relationship. This is surprising considering that the transversely isotropic Holzapfel law employed in our study was previously found to reproduce the Klotz volume relationship well [16]. As we only consider a single clinical dataset the discrepency in pressure-volume relationships could be a chance occurrence. However, there could also be a significant difference between the true ex-vivo and in-vivo pressure volume relationships of our patient. This would explain the discrepency between the Klotz predicted volumes, which are based on ex-vivo data, and our simulated volume curve which is based on in-vivo data. In the in-vivo situation the contracting atria may pull on the mitral valve plane and thereby contribute to in-vivo ventricular longitudinal lengthening. This mechanism could in-

crease the volume of the ventricle without increasing the pressure, and is absent in the ex-vivo procedures employed in [24]. If the pull of the atria on the mitral valve plane were significant and accounted for in our model, we would expect stiffer material properties and a larger unloaded volume closer to that predicted by the Klotz relation.

Active tension was assumed to be 0 in our model. Typically this tension is absent in atrial systole for a healthy heart, but may extend into atrial systole under pathological conditions. If active tension were present in the diastasis phase of our patient, than its release in atrial systole would contribute to strain. Missing this effect would lead to an underestimation of tissue stiffness in our model. Furthermore the LV pressure and strain measurements were not taken simultaneously and had to be synchronized. Errors in this synchronization can lead to large errors in the determination of end diastolic pressure, especially if the timing of end diastole is falsely placed in the isovolumic contraction phase where pressure changes are large. Such uncertainty in pressure synchronization propagates to our estimates of material stiffness.

The pressure-volume relation and many of the pressure-strain relations measured in the in-vivo dataset have a convex shape for the first 4 pressure measurements. This convexity was reproduced poorly by the model, and may be due to the effects of inertia. As the force of the pressure is first applied, we can expect wall velocities, and therefore strain and volume changes, to be small until the walls build significant momentum from their initial state of rest. As inertia was not included in our quasi-static model, this would explain the discrepancy between simulated and measured data. Another possibility is the pulling effect of the atria on the mitral valve plane. Such a pull might follow a classical Hill curve shape, which we can see in the strain data. However, due to the noisy nature of our echocardiographic data and the lack of precision in our pressure measurements, we do not know whether or not the observed convexity was physiological.

In our simulated and measured data we noticed that the heavily infarcted region encompassing basal to mid, and inferior to posterior segments differed in several ways from healthy segments. In these infarcted segments longitudinal and radial strains were smaller, optimal b and b_f parameters larger, and the simulated equibiaxial stress-strain relationships showed greater fiber stresses. All of these observations indicate increased myocardial stiffness. This is consistent with the

increased stiffness observed in healing infarcts during an ex-vivo tissue experiment [15] and in previous computational modelling with in-vivo data [31].

We also observed that the mid lateral segment was identified as free from scar in the late enhancement MRI analysis, yet showed signs of stiffness similar to the heavily infarcted segments described above. This might be a case of an infarction impairing the mechanics of neighbouring healthy tissue [18]. The apical anterior segment was also identified as free from scar and yet showed signs of stiffness. However, the low measured strain and consequent high simulated stiffness in this region may have simply been a consequence of the speckle tracking algorithm's inability to follow the apical tissue in the 3-D echo images.

Ideally model material parameters should be uniquely identifiable from in-vivo data in order to produce potentially useful biomarkers for clinical practice. Recently it has been shown that the linear parameters a and a_f of a reduced Holzapfel-Ogden law, corresponding to the strain energy (4.1) with $b = b_f = 5.0$, are structurally identifiable [16]. Structural identifiability means that there exist sets of model loaded states such that only one set of parameters produces them, making it theoretically possible to uniquely identify the parameters. In our synthetic data test we made use of the reduced Holzapfel model suggested by the study [16], and were able to uniquely reproduce parameters, which we expected due to the parameters' structural identifiability. As the unloaded geometry estimate depended upon a sequence of material parameter estimates, we expected it to be uniquely identifiable as well, which is what we observed in the experiment.

Our in-vivo data is corrupted by noise, which makes the question of the unique identifiability of parameters more complex. Additionally, we have optimized the exponential b and b_f parameters in our in-vivo experiment, for which structural identifiability is still an open question. Furthermore, in contrast to the synthetic data test, we have spatially resolved all of the parameters in the in-vivo case, thereby greatly increasing their number. Due to the high number of parameters, we have added regularization to the functional in order to constrain the parameter fitting . Indeed, Figure 4.5 confirms the existence of several material parameter sets that fit the model to the data very similarly, but differ in their smoothness. By choosing corner points in the space of optimized data and smoothness functionals our aim was to pick the smoothest data set that still fit the data well. Ultimately though, we do not yet know how uniquely the spatially resolved in-vivo parame-

ters can be estimated, which is a significant limitation in our study.

Further limitations are related to data collection, in particular the speckle tracking algorithm was unable to track the apical rocking phenomenon, pressure measurements were imprecise, and only a single clinical dataset was included.

The computational model lacked several relevant physical effects, notably inertia, viscoelasticity, residual stresses in the unloading geometry, mechanical coupling of the LV to the right ventricle and atria, the effect of sheet microstructure, and tissue compressibility due to blood entering and exiting the ventricle via coronary vessels. The spring constant at the base was tuned due to algorithmic and not physiological considerations. The apex of the computational model was free while longitudinal motion at the base was fixed. The in-vivo situation is the opposite, the base moves longitudinally and the apex is fixed. The fiber orientations were generic and not patient specific. Previous studies have shown that the elastic anisotropy of infarcted areas can be significantly different from healthy tissue [12, 31], an effect not captured by the assumed healthy fiber orientations in the model. The measured ventricular volumes were not included in the parameter estimation in order to simplify the study. Their inclusion might have helped to further constrain the space of optimal parameters.

The spatial discretization of the material parameters was not optimized. The computational mesh used to solve the variational equation of motion (4.4) was also used for the representation of the spatial parameters due to ease of implementation. It is possible that a coarser representation of the material parameters could have also produced good model-data fits. Fewer parameters might improve uniqueness and reduce the number of SQP iterations needed to find a minimum.

4.5 Conclusion

Adjoint based data assimilation has been used to personalize a mechanics model to reflect the heterogeneities in material properties throughout an infarcted left ventricle using in-vivo data. Further trials with more datasets are warranted in order to evaluate the applicability of the technique.

Acknowledgements

Our work is supported by The Research Council of Norway through a Centres of Excellence grant to the Center for Biomedical Computing at Simula Research Laboratory, project number 179578, and also through the Center for Cardiological Innovation at Oslo University Hospital project number 203489. Computations were performed on the Abel supercomputing cluster at the University of Oslo via Notur project nn9316k. Special thanks to Lars Andreas Dejgaard for assistance with speckle tracking strain analysis, to Sjur Gjerald for assistance with fiber orientations, and Sareh Behdadfar for early discussions regarding unloading of ventricular geometries.

Bibliography

[1] Jazmin Aguado-Sierra, Adarsh Krishnamurthy, Christopher Villongco, Joyce Chuang, Elliot Howard, Matthew J Gonzales, Jeff Omens, David E Krummen, Sanjiv Narayan, Roy CP Kerckhoffs, et al. Patient-specific modeling of dyssynchronous heart failure: a case study. *Progress in biophysics and molecular biology*, 107(1):147–155, 2011.

[2] Liya Asner, Myrianthi Hadjicharalambous, Radomir Chabiniok, Devis Peresutti, Eva Sammut, James Wong, Gerald Carr-White, Philip Chowienczyk, Jack Lee, Andrew King, et al. Estimation of passive and active properties in the human heart using 3D tagged MRI. *Biomechanics and modeling in mechanobiology*, 15:1121–1139, 2015.

[3] Gabriel Balaban, Martin S Alnæs, Joakim Sundnes, and Marie E Rognes. Adjoint multi-start-based estimation of cardiac hyperelastic material parameters using shear data. *Biomechanics and Modeling in Mechanobiology*, pages 1509–1521.

[4] S Balay, J Brown, K Buschelman, WD Gropp, D Kaushik, MG Knepley, L Curfman McInnes, BF Smith, and H Zhang. PETSc web page. `http://www.mcs.anl.gov/petsc`, 2015.

[5] JD Bayer, RC Blake, G Plank, and NA Trayanova. A novel rule-based algorithm for assigning myocardial fiber orientation to computational heart models. *Annals of biomedical engineering*, 40(10):2243–2254, 2012.

[6] Joris Bols, Joris Degroote, Bram Trachet, Benedict Verhegghe, Patrick Segers, and Jan Vierendeels. A computational method to assess the in vivo

stresses and unloaded configuration of patient-specific blood vessels. *Journal of computational and Applied mathematics*, 246:10–17, 2013.

[7] Manuel D Cerqueira, Neil J Weissman, Vasken Dilsizian, Alice K Jacobs, Sanjiv Kaul, Warren K Laskey, Dudley J Pennell, John A Rumberger, Thomas Ryan, Mario S Verani, et al. Standardized myocardial segmentation and nomenclature for tomographic imaging of the heart a statement for healthcare professionals from the cardiac imaging committee of the Council on Clinical Cardiology of the American Heart Association. *Circulation*, 105(4):539–542, 2002.

[8] Radomir Chabiniok, Dominique Chapelle, Pierre-François Lesault, Alain Rahmouni, and Jean-François Deux. Validation of a biomechanical heart model using animal data with acute myocardial infarction. In *CI2BM09 - MICCAI Workshop on Cardiovascular Interventional Imaging and Biophysical Modelling*, page 9 pages, London, United Kingdom, September 2009.

[9] Shauna M Dorsey, Jeremy R McGarvey, Hua Wang, Amir Nikou, Leron Arama, Kevin J Koomalsingh, Norihiro Kondo, Joseph H Gorman, James J Pilla, Robert C Gorman, et al. MRI evaluation of injectable hyaluronic acid-based hydrogel therapy to limit ventricular remodeling after myocardial infarction. *Biomaterials*, 69:65–75, 2015.

[10] Longling Fan, Jing Yao, Chun Yang, Zheyang Wu, Di Xu, and Dalin Tang. Material stiffness parameters as potential predictors of presence of left ventricle myocardial infarction: 3D echo-based computational modeling study. *Biomedical engineering online*, 15(1):1, 2016.

[11] Patrick E Farrell, David A Ham, Simon W Funke, and Marie E Rognes. Automated derivation of the adjoint of high-level transient finite element programs. *SIAM Journal on Scientific Computing*, 35(4):C369–C393, 2013.

[12] Gregory M Fomovsky, Andrew D Rouillard, and Jeffrey W Holmes. Regional mechanics determine collagen fiber structure in healing myocardial infarcts. *Journal of molecular and cellular cardiology*, 52(5):1083–1090, 2012.

[13] Hao Gao, David Carrick, Colin Berry, Boyce E. Griffith, and Xiaoyu Luo. Dynamic finite-strain modelling of the human left ventricle in health and disease using an immersed boundary-finite element method. *IMA Journal of Applied Mathematics*, 2014.

[14] Christophe Geuzaine and Jean-François Remacle. Gmsh: A 3-D finite element mesh generator with built-in pre-and post-processing facilities. *International Journal for Numerical Methods in Engineering*, 79(11):1309–1331, 2009.

[15] Krishanu B Gupta, Mark B Ratcliffe, Michael A Fallert, LH Edmunds, and Daniel K Bogen. Changes in passive mechanical stiffness of myocardial tissue with aneurysm formation. *Circulation*, 89(5):2315–2326, 1994.

[16] Myrianthi Hadjicharalambous, Radomir Chabiniok, Liya Asner, Eva Sammut, James Wong, Gerald Carr-White, Jack Lee, Reza Razavi, Nicolas Smith, and David Nordsletten. Analysis of passive cardiac constitutive laws for parameter estimation using 3D tagged MRI. *Biomechanics and modeling in mechanobiology*, 14(4):807–828, 2015.

[17] Per Christian Hansen and Dianne Prost O'Leary. The use of the l-curve in the regularization of discrete ill-posed problems. *SIAM Journal on Scientific Computing*, 14(6):1487–1503, 1993.

[18] Jeffrey W Holmes, Thomas K Borg, and James W Covell. Structure and mechanics of healing myocardial infarcts. *Annu. Rev. Biomed. Eng.*, 7:223–253, 2005.

[19] Gerhard A Holzapfel. *Nonlinear solid mechanics:A Continuum Approach for Engineering*. Wiley Chichester, 2000.

[20] Gerhard A Holzapfel and Ray W Ogden. On planar biaxial tests for anisotropic nonlinearly elastic solids. a continuum mechanical framework. *Mathematics and mechanics of solids*, 14:474–489, 2008.

[21] Gerhard A Holzapfel and Ray W Ogden. Constitutive modelling of passive myocardium: a structurally based framework for material characterization.

Philosophical transactions. Series A, Mathematical, physical, and engineering sciences, 367(1902):3445–75, sep 2009.

[22] P Hood and C Taylor. Navier-stokes equations using mixed interpolation. *Finite element methods in flow problems*, pages 121–132, 1974.

[23] Oslo University Hospital. Acute feedback on left ventricular lead implantation location for cardiac resynchronization therapy (CCI impact). `https://clinicaltrials.gov`, 2016.

[24] Stefan Klotz, Ilan Hay, Marc L Dickstein, Geng-Hua Yi, Jie Wang, Mathew S Maurer, David A Kass, and Daniel Burkhoff. Single-beat estimation of end-diastolic pressure-volume relationship: a novel method with potential for noninvasive application. *American Journal of Physiology-Heart and Circulatory Physiology*, 291(1):403–412, 2006.

[25] Dieter Kraft et al. A software package for sequential quadratic programming. Deutsche Forschungs- und Versuchsanstalt fuer Luft- und Raumfahrt e.V. (DFVLR), Germany. `http://hdl.handle.net/10068/147127`, 1988.

[26] Adarsh Krishnamurthy, Christopher T Villongco, Joyce Chuang, Lawrence R Frank, Vishal Nigam, Ernest Belezzuoli, Paul Stark, David E Krummen, Sanjiv Narayan, Jeffrey H Omens, et al. Patient-specific models of cardiac biomechanics. *Journal of computational physics*, 244:4–21, 2013.

[27] Sander Land, Steven Niederer, Pablo Lamata, Nicolas P Smith, et al. Improving the stability of cardiac mechanical simulations. *Biomedical Engineering, IEEE Transactions on*, 62(3):939–947, 2015.

[28] Xiaoye S. Li and James W. Demmel. SuperLUDIST: A scalable distributed-memory sparse direct solver for unsymmetric linear systems. *ACM Trans. Mathematical Software*, 29(2):110–140, June 2003.

[29] Anders Logg, Kent-Andre Mardal, Garth N. Wells, et al. *Automated Solution of Differential Equations By the Finite Element Method*. Springer, 2011.

[30] Jeremy R McGarvey, Dimitri Mojsejenko, Shauna M Dorsey, Amir Nikou, Jason A Burdick, Joseph H Gorman, Benjamin M Jackson, James J Pilla, Robert C Gorman, and Jonathan F Wenk. Temporal changes in infarct material properties: an in vivo assessment using magnetic resonance imaging and finite element simulations. *The Annals of thoracic surgery*, 100(2):582–589, 2015.

[31] Dimitri Mojsejenko, Jeremy R McGarvey, Shauna M Dorsey, Joseph H Gorman III, Jason A Burdick, James J Pilla, Robert C Gorman, and Jonathan F Wenk. Estimating passive mechanical properties in a myocardial infarction using MRI and finite element simulations. *Biomechanics and modeling in mechanobiology*, 14(3):633–647, 2015.

[32] Masato Morita, Chad E Eckert, Kanji Matsuzaki, Mio Noma, Liam P Ryan, Jason A Burdick, Benjamin M Jackson, Joseph H Gorman, Michael S Sacks, and Robert C Gorman. Modification of infarct material properties limits adverse ventricular remodeling. *The Annals of thoracic surgery*, 92(2):617–624, 2011.

[33] Amir Nikou, Shauna M Dorsey, Jeremy R McGarvey, Joseph H Gorman III, Jason A Burdick, James J Pilla, Robert C Gorman, and Jonathan F Wenk. Effects of using the unloaded configuration in predicting the in vivo diastolic properties of the heart. *Computer methods in biomechanics and biomedical engineering*, 19(16):1714–1720, 2016.

[34] D Nordsletten, M McCormick, PJ Kilner, P Hunter, D Kay, and NP Smith. Fluid–solid coupling for the investigation of diastolic and systolic human left ventricular function. *International Journal for Numerical Methods in Biomedical Engineering*, 27(7):1017–1039, 2011.

[35] Joseph C Walker, Mark B Ratcliffe, Peng Zhang, Arthur W Wallace, Bahar Fata, Edward W Hsu, David Saloner, and Julius M Guccione. MRI-based finite-element analysis of left ventricular aneurysm. *American Journal of Physiology-Heart and Circulatory Physiology*, 289(2):H692–H700, 2005.

[36] Jiahe Xi, Pablo Lamata, Steven Niederer, Sander Land, Wenzhe Shi, Xiahai Zhuang, Sebastien Ourselin, Simon G Duckett, Anoop K Shetty, C Aldo

Rinaldi, et al. The estimation of patient-specific cardiac diastolic functions from clinical measurements. *Medical image analysis*, 17(2):133–146, 2013.